Time-Dependant Behaviour of Engineered Cement-Based Composites

by

William Peter Boshoff

Dissertation presented for the degree of

Doctor of Philosophy in Engineering

at the University of Stellenbosch

Promotor:

Prof G.P.A.G. van Zijl

March 2007

Declaration

I, the undersigned, hereby declare that the work contained in this dissertation is my own original work and that I have not previously in its entirety or in part submitted it at any university for a degree.

Signature: …….

Date: …….

SUMMARY

ECC (Engineered Cement-based Composites) is a type of HPC (High Performance Concrete) that was engineered to overcome the weaknesses of ordinary concrete. It shows high ductility as it can resist the full tensile load at a strain of more than 3 %. This superior response is achieved with multiple cracking under tensile loading which has a pseudo strain hardening phenomenon as result.

The purpose of the research project reported in this dissertation is to investigate and characterise the time-dependant behaviour of ECC and create a constitutive model to numerically simulate the static and time-dependant behaviour of ECC.

To investigate the time-dependant behaviour experimentally, rate and creep tests were done on the meso- and macro-level while rate tests were done on the structural-level. The meso-level was represented by the pull-out testing of fibres embedded in the cement-based matrix and direct tensile tests were done for the macro-level. Flexural tests on thin beams were done to simulate the structural-level.

Strong time-dependant behaviour was found on all three these levels. On the meso-level, the most prominent finding is that the failure mechanism can change with a change of strain rate, i.e. fibre pull-out at a low pull-out rate, while with a high pull-out rate, fibre rupture can occur. Even though the strength of a tensile specimen on the macro-level showed a dependence on the strain rate, the ductility remained constant over four orders of magnitude of the strain rate. On the structural-level, however, a reduction of the flexural ductility was found with an increase of the deflection rate.

The tensile creep on the macro-level was found to consist of three parts, namely matrix creep, time-dependant crack initiation and the time-dependant fibre pull-out which causes cracks to widening when under a tensile load. The effect of the last mentioned phenomenon was found to increase exponentially when the load is increased. No tensile creep fracture was found on the macro-level at a load of 80 % of the ultimate static load after 8 months, but considerable creep occurred during this period.

A constitutive model based on a damage mechanics approach was created and implemented. This model was found to predict the static behaviour well, except for the ductility. The under estimation of the ductility can be ascribed to fibre orientation caused by an edge effect in the thin ECC members that were investigated. The static model also predicted the rate-dependant behaviour of a beam tested in flexure with reasonable accuracy.

A preliminary implementation was done of a constitutive model created to simulate the creep behaviour of ECC. This model is based on a damage mechanics approach combined with elasto-plasticity to incorporate matrix creep and the non-linear tertiary creep found at high loads. This model needs to be expanded to include the time-dependant crack propagation and the time-dependant fibre pull-out to accurately simulate and predict the total time-dependant behaviour of ECC.

OPSOMMING

ECC (“Engineered Cement-based Composites”) is ‘n tipe HPC (“High Performance Concrete”) wat ontwerp is om die swakhede van gewone beton te verbeter. Hierdie materiaal het ‘n hoe duktiliteit en kan die volle trekkrag weerstaan met ‘n vervorming van meer as 3 %. Hierdie uitstaande gedrag word verkry deur meerdere krake wat vorm gedurende ‘n trek belasting wat vervormingsverharding tot gevolg het.

Die doel van hierdie navorsingsprojek wat weergegee word in hierdie proefskrif is om die tydsafhanklike gedrag van ECC te ondersoek en ‘n konstituwe numeriese model op te stel wat die statiese asook die tydsafhanklike gedrag simuleer.

Om die tydsafhanklike gedrag eksperimenteel te ondersoek is belastingstempo- en kruiptoetse gedoen op die meso- en makrovlakke, terwyl belastingstempo-toetse gedoen is op die struktuurvlak. Die mesovlak was verteenwoordig deur enkel vesels wat uitgetrek word uit die matriks en direkte trektoetse was gedoen op die makrovlak. Buigtoetse op dun balke is gedoen om die struktuurvlak te simuleer.

Beduidende tydsafhanklike gedrag was op al drie hierdie vlakke gevind. Die belangrikste bevinding op die mesovlak was dat die falings meganisme verander het met ‘n verander in die uittrek tempo. Op die makrovlak het die treksterkte beduidend afgehang van die belastingstempo terwyl die duktiliteit konstant gebly het oor al die belastingstempo’s. Op die struktuurvlak was daar egter ‘n afname in duktiliteit met ‘n verhoging van die belastingstempo.

Daar was gevind dat die kruip in trek op die makrovlak uit drie dele bestaan, naamlik die matriks kruip, die tydsafhanklike kraak vermeerdering en die tydsafhanklike uittrek van vesels wat veroorsaak dat die kraakwydte vergroot na ‘n tyd. Die effek van die laasgenoemde gedrag is gevind om ekponensiëel toe te neem met ‘n toename in belasting. Geen kruip faling was egter gevind oor 8 maande met ‘n belasting van 80 % van die statiese sterkte nie, maar noemenswaardige kruip vervorming is gevind gedurende hierdie tyd.

‘n Konstituwe model wat gebaseer is op skade meganika was geskep en geïmplementeer. Hierdie model het die statiese gedrag goed gesimuleer, behalwe vir die duktiliteit. Die onderskatting van die duktiliteit is heelmoontlik te wyte aan die

oriëntering van die vesels naby die kante van die proefstukke. Hierdie statiese model het ook die belastingtempo gedrag van balke in buig redelik goed gesimuleer.

‘n Voorlopige implementering van ‘n tydsafhanklike konstituwe model was gedoen om die tydsafhanklike gedrag van ECC te simuleer. Hierdie model is gebasseer op skade meganika gekombineerd met ‘n elastiese-plastisiteits teorie om die liniêre en nie-liniêre kruip te modelleer. Hierdie model moet nog uitgebrei word om die tydsafhanklike vesel uittrek te inkorporeer om die volledige tydsafhanklike gedrag te simuleer.

ACKNOWLEDGMENTS

I would like to thank the following people for their assistance:

- The staff of the laboratory and workshop of the Civil Engineering Department, University of Stellenbosch, for their time and effort in assisting with the experimental work.
- Viktor Mechtcherine for his hospitality and guidance during my stay in Kaiserslautern.
- Gideon van Zijl, my promoter, for his guidance and support.
- Most importantly, Huba, my wife, who's loving support and patience made this dissertation possible.

TABLE OF CONTENTS

LIST OF SYMBOLS

A	Material model parameter used to calculate the non-linear creep factor.
AS	Autogenious shrinkage.
BC	Basic creep.
B	Material model parameter used to calculate the non-linear creep factor.
b	Depth of beam
β	Slip-hardening coefficient.
C_c	Creep compliance.
C_1	Material model parameter that represents the total creep for one stress unit.
C_2	Material model parameter that represents the rate of creep.
Δ	Pull-out displacement.
Δ_c	Crack width.
ΔL	Length change.
Δ_n	Normalised pull-out displacement.
Δ_p	Pressure difference over liquid film.
d	Fibre diameter.
$\overline{\overline{D}}^{e}$	Elastic stiffness matrix.
DC	Drying creep.
DS	Drying shrinkage.
E_f	E-modulus of the fibre.
E_{long}	Long term E-modulus.
E_m	E-modulus of the matrix.
ε	Strain.
ε_c	Creep strain.

ε_e	Elastic strain.
ε_{sh}	Material model parameter for the tensile ductility.
$\tilde{\varepsilon}$	Equivalent strain.
$\tilde{\varepsilon}_H$	Equivalent strain history variable.
ε_{tu}	Material model parameter for the ultimate strain.
G_d	Chemical bond of a fibre to the matrix.
γ	Surface tension.
g	Snubbing coefficient.
h	Height of section.
H_1	History variable.
H_2	History variable.
J_c	Crack tip energy.
MOR	Modulus of rupture.
κ	Plastic strain.
L	The fibre length; Length between the supports.
$L_{critical}$	Critical embedment length of fibre.
L_e	Original embedment length; Element length.
L_s	Material model parameter for the softening length.
P	Applied force load.
P_Δ	Load drop during fibre debonding
Φ	Creep factor.
φ	Non-linear creep factor.
r	Radius of meniscus.
S	Material model parameter for the crack spacing.
σ	Stress.
σ_{max}	Maximum stress resistance over a crack plane bridged by fibres.
σ_{fc}	Material model parameter for the first crack.
σ_u	Material model parameter for the ultimate stress.
t	Thickness of the notch area; Time.
τ	Interfacial shear stress.
τ_0	Initial interfacial shear stress.
ν	Poisson’s ratio; Deflection.
V_f	Volume ratio consisting of fibre.

V_f^{crit}	Critical volume ratio of fibre.
w_c	Crack width.
ω	Damage variable.

CHAPTER 1

Introduction

Concrete has been used over many centuries as a reliant, fairly durable building material. Two of the main advantages of concrete are that it has a high compressive strength and can be cast on the construction site into almost any shape and size. The short comings of concrete is becoming more and more prominent in this day and age due to the emphases of design moving towards economical design rather than a durable design. The most prominent disadvantages of concrete are the brittleness during failure and the low tensile strength, which is about one tenth of the compression strength. The low tensile strength is compensated with steel reinforcing, but cracking still occurs during the normal use of concrete. These cracks lead to durability problems as water penetrates the concrete through the cracks and aggravates the corrosion of the steel reinforcing which in turn results in structural degradation.

ECC (Engineered Cement-based Composites) is a type of HPC (High Performance Concrete) that was engineered to overcome these weaknesses of ordinary concrete. It shows high ductility as it can resist the full tensile load at a strain of more than 3 % compared to concrete which fails on average at a strain of 0.01 % in tension. When using ECC instead of ordinary concrete the strain capacity increases more than 300 times. This leads to a high energy absorption capacity of ECC.

During the increase of strain under tensile loading of ECC, a constant strain hardening effect is found and many, closely spaced, micro cracks are formed in the material. These fine, multiple cracks reduce the problem of water penetration and thus improve the durability of structures.

ECC however cost more than ordinary concrete, but if the material is used to exploit its advantages, it becomes a competitive material in the building industry. In several applications the advantages of ECC may be exploited:

- Earthquake loading application: Due to the high ductility and flexibility of ECC it can be used in designated areas in a multi-storey structure to withstand earthquake loadings. ECC can be used as the material for the hinge areas as well as shear walls and panels.
- Thin membrane members: Due to the high ductility, thin membrane members, i.e. less than 15 mm thick, can be made e.g. pipes and tiles.
- Repair material: Due to the high strain capacity and energy absorption, ECC is ideal to be used as repair material, especially for bonded overlays.
- Durability application: Due to the fine, multiple cracking phenomenon of ECC it can be used as a permanent formwork for concrete members. This will also add to the shear resistance of the member as ECC has a higher shear resistance than ordinary concrete.

The mechanical behaviour of ECC has been well researched over the past 10 years, but little work has been done on the time-dependent behaviour and no research has been published on the tensile creep characteristics of ECC. There is no indication whether this high ductility and energy absorption capability is sustainable if the material is exposed to a long term load. Premature and unexpected failure could occur over a period of time at a load lower that the ultimate load determined with short time tests in laboratories.

Also, a robust finite element material model is not available to simulate the static behaviour of ECC, not to mention the long term creep behaviour. The finite element models available (Han et al 2003, Simone et al 2003, Kabele 2000) either have shortcomings, especially simulating the localisation, or are too complex, intended for fundamental academic research (Kabele 2005). Without an accurate and robust finite element model, it is also difficult to predict the long term creep deflection of any structure incorporating ECC.

These shortcomings in the research and development of ECC form the basis of the research project reported in this dissertation. The time-dependant behaviour of ECC is thoroughly investigated from a single fibre level to a structural level. A finite element model is also created to simulate the structural behaviour of ECC.

In Chapter 2 a theoretical background is given on ECC and the typical time-dependant behaviour found for cement-based materials.

In Chapter 3 the rate dependence of ECC is investigated on the single fibre level, material level and structural level. This was done by performing tests at different loadings rates.

In Chapter 4 the creep behaviour is characterised. This was done using tensile creep tests of ECC specimens. The creep behaviour of the fibres and the fibre pull-out were investigated and are reported.

A constitutive finite element material model is elaborated in Chapter 5. Problems that occur in the modelling of the localisation behaviour are reported and addressed. The verification of this model is done in Chapter 6.

In Chapter 7 the constitutive model is used to predict the time-dependant behaviour and a time-dependant material model is proposed that can simulate the time-dependant response directly.

CHAPTER 2

Background of ECC and Time-Dependant Behaviour

The phenomenological mechanical behaviour of ECC and the micro-mechanical models that can be used to engineer the material are presented in this chapter together with a background study on the typical time-dependant behaviour found in cement-based materials.

2.1 Engineered Cement-based Composites

ECC (Engineered Cement-based Composites) are a special type of FRC (Fibre Reinforced Concrete) consisting of the ingredients of ordinary concrete, i.e. water, cement and cement extenders, aggregates and additives for the workability modifications. Short, randomly distributed polymer fibres at low volume percentages (up to 2 %) are added to the carefully engineered mixture of ingredients and a superior response is achieved (Li 1998, Li et. al. 2001). The tensile behaviour of ECC is what sets it apart from ordinary concrete and even ordinary FRC. The tensile behaviour shows high ductility, high toughness and multiple cracking.

Even though FRC has been researched for many decades (Hannant 1978), ECC development only began recently in the early 1990's (Li and Wang 1990, Li 1992, Li 1993) with numerous ground breaking developments, e.g. the tailoring of the surface properties of PVA (Polyvinyl Alcohol) fibres to create an economical substitute for expensive polyethyleen fibres (Li and Wu 2002).

In this section, the macroscopic behaviour of ECC will be reviewed together with micro-mechanical models used to engineer the material.

2.1.1 Macroscopic behaviour of ECC

A typical tensile response of ECC is shown schematically in Figure 2.1 and compared to a typical response of ordinary concrete and FRC. Even though FRC shows some ductility, no multiple cracking is found as in the case of ECC.

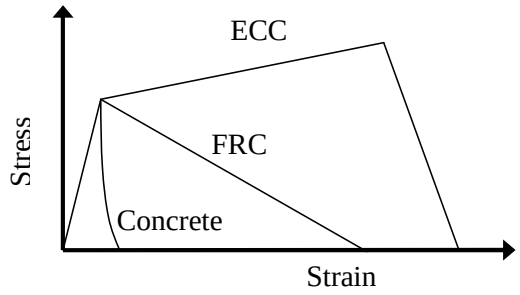

Figure 2.1 The tensile stress-strain response of ECC compared to FRC and ordinary concrete schematically.

The strain hardening is achieved by multiple cracking of the matrix. As for any material under a tensile load, the matrix cracks at the weakest point. If no fibres are present in the matrix, the material would fail completely. If fibres are used to reinforce the matrix, the load will be carried by the fibres that bridge the crack. In the case of FRC, the fibre crack bridging capacity is less than the cracking strength of the concrete, thus the crack widens and the load is reduced if the strain is increased. In the case of ECC, however, the fibres bridging a crack in the matrix have the capacity to sustain the load. If the strain is then increased, the load will increase and the matrix will crack at the next weakest point which is stronger that the first cracking point, thus an increase of the stress is found. This is a pseudo-strain hardening phenomenon similar to post yielding strain hardening in steel with the difference that it is accompanied by cracking. This process will continue until the load becomes more than the crack bridging capacity of the fibres. At this point a localising crack will form at one of the multiple cracks and strain softening will start. Strain hardening can be achieved over a large tensile strain range, up to and in excess of 4 % (Li et al 2001). An example of the multiple cracking and high ductility is shown in Figure 2.2.

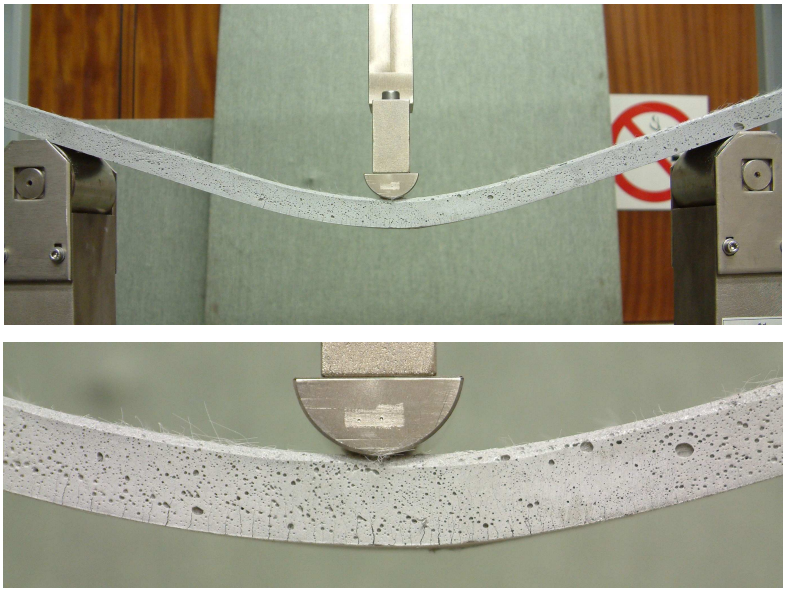

Figure 2.2 Example of the ductility of ECC and the multiple cracking.

There are two requirements for multiple cracking to occur (Li 1997). The first is already explained in detail: the crack bridging capacity of the fibres must be more than the matrix cracking strength. The second is that steady-state cracking must occur in stead of an unstable Griffith crack which occurs in qausi brittle material like concrete. This will be explained further in Section 2.1.3.

The unloading and reloading behaviour is an important characteristic of ECC as it will assist in the structural design using ECC, especially for repetitive loading, e.g. an earthquake loading. A typical result of unloading and reloading tests that were done at the University of Stellenbosch is shown in Figure 2.3. It is clear that the unloading and reloading stiffness decreases with a higher tensile strain. For further details on the reverse cyclic response of ECC the reader is referred to Kesner et al (2003).

2.1.2 Single fibre level

In ECC, or any FRC for that matter, three structural components exist i.e. the matrix, the fibres and the matrix-fibre interface. To be able to design the material for the desired ECC mechanical behaviour the single fibre pull-out behaviour needs to be understood and mathematically modelled. Some of the micro-mechanical models in use are explained in this section.

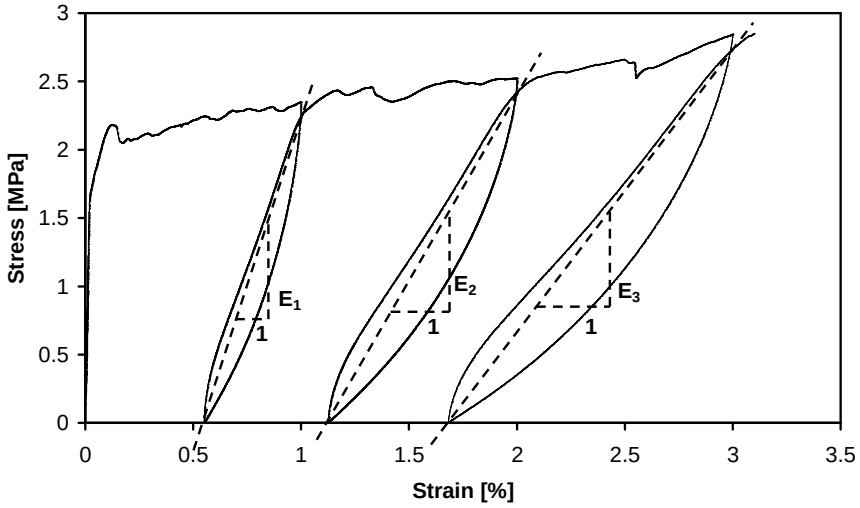

Figure 2.3 The unloading and reloading tensile behaviour of ECC.

The fibres used in this research project were made of PVA (Polyvinyl Alcohol). The fibres have a diameter of 40 μm and a length of 12 mm. The tensile strength is 1560 MPa and the stiffness 40 GPa.

The most basic model of the fibre pull-out behaviour was first introduced by Li (1992). The model is based on the assumption that a constant, uniform frictional force is present on the surface between the fibre and the matrix. The magnitude of the frictional shear stress is given as τ_0. This is shown in Figure 2.4 a). This model also assumes that the value of τ_0 is the same regardless of the embedment length of the fibre. This model would result in a fibre pull-out response as shown schematically in Figure 2.4 b).

An adjustment was made to this model by Lin and Li (1997) by introducing a slip-hardening coefficient, β. A model that included slip hardening was needed to

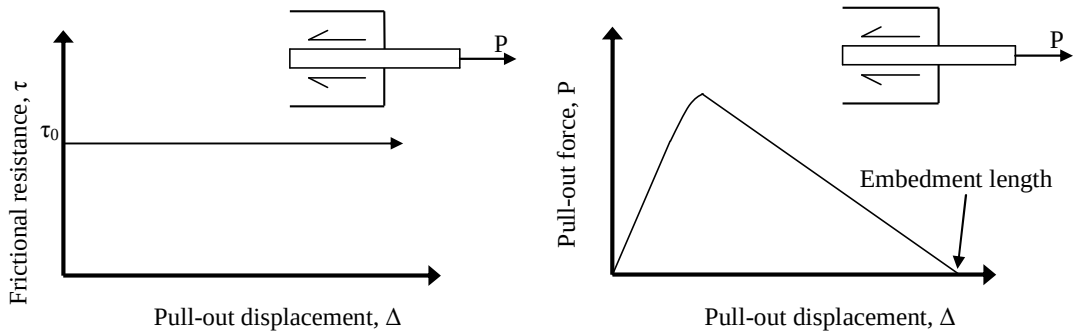

Figure 2.4 a) The uniform shear resistance model for fibre pull-out. b) The fibre pull-out response using this model shown schematically.

consider the phenomenon that the interfacial bond, τ_0, increases as the pull-out displacement increases. The effect of the pull-out displacement on the interfacial shear resistance if slip-hardening is present is shown schematically in Figure 2.5 and the expression for τ is:

$$\tau = \tau_0\left(1+\beta\frac{\Delta}{d}\right) \qquad (2.1)$$

with Δ the pull-out displacement and d the fibre diameter.

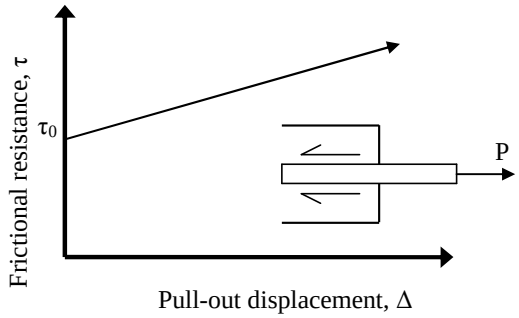

Figure 2.5 The effect of the slip hardening coefficient on the interfacial shear resistance between the fibre and the matrix, shown schematically.

When PVA fibres were introduced to ECC, a third parameter became necessary to model the fibre pull-out behaviour, termed chemical bond by Kanda and Li (1998) and Lin et al (1999). During the pull-out of fibres which have a high chemical bond to the matrix, the bond has to be broken before pull-out can start. A phenomenon found with these fibres in some cases is that a sudden load drop occurs during the pull-out process that coincides with the full debonding of the fibre, as shown schematically in Figure 2.6.

Three approaches are available to consider the chemical bond in the micro-mechanical models, namely a strength based model (Kanda and Li, 1998), fracture based model (Kanda and Li, 1998) and an energy based model (Lin et al 1999). The most widely used model currently for ECC is the energy based model. The expression to calculate the energy based chemical bond is:

$$G_d = \frac{2P_\Delta{}^2}{\pi^2 E_f d^3} \qquad (2.2)$$

with P_Δ as the load drop and E_f the stiffness of the fibre.

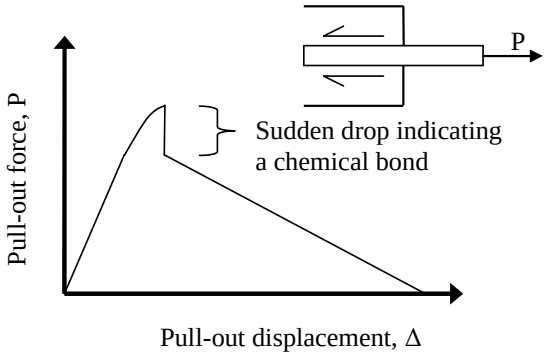

Figure 2.6 The sudden drop of pull-out force that indicates that a chemical bond exists between the matrix and the fibre shown schematically.

With the introduction of PVA fibres in the late 1990's, the dominant mechanism during fracture was found to be fibre rupture. This gave the impression that hydrophilic fibres, of which PVA fibres are an example, were not suitable for strain hardening materials. The hydrophilic nature leads to high interfacial bond, around 3.8 to 5.9 MPa (Redon et al 2001), which may cause fibre rupture. PVA fibres were also found to have a high chemical bond which needed to be broken before fibre slippage could occur (Lin et al 1999). Together with these properties, PVA fibres also showed a strong slip-hardening coefficient, in the region of $\beta = 2.2$. The slip-hardening was found to be so profound for these hydrophilic fibres that pull-out of an embedment length longer than 1 mm would result in fibre rupture (Kanda and Li, 1998). An oil coating was introduced to the PVA fibres and this reduced the interfacial bond, the chemical bond and the slip-hardening coefficient considerably. This gave the possibility for PVA fibres to produce strain hardening in cement-based materials.

2.1.3 Micro-mechanical modelling of ECC

The early micro-mechanical models introduced for the design of ECC materials were based on the simple assumption of the fibre pull-out behaviour shown in Figure 2.4 a)

(Li 1993). As mentioned before, there are two requirements for the tensile strain hardening behaviour of ECC. Firstly, crack bridging capacity of the fibres must be more than the matrix cracking strength and secondly, steady-state cracks must develop in the matrix.

The first requirement was addressed by the early micro-mechanical models (Aveston et al 1971) by applying volume averaging over a crack plane with fibre bridging the plane. The following equation was derived for the crack bridging capacity of a crack plane:

$$\sigma_{\max} = 0.5 V_f \, g \, \tau_0 \frac{L}{d} \qquad (2.3)$$

with V_f the volume of fibres, L the fibre length and g, the snubbing coefficient. The snubbing coefficient was introduced by Li (1992) to incorporate the increase of the fibre resistance when the fibre is pulled out at an angle.

This expression gives the ultimate crack bridging resistance of the fibres. From this, if the cracking strength of the matrix is known, the critical fibre volume can be calculated to fulfil the first requirement for strain hardening. It is however important to note that the fibre strength is not a variable in Equation 2.3. This equation is thus based on the assumption that no fibre rupture occurs, only fibre pull-out. This is however the case for fibres with low interfacial shear resistance, e.g. polyethylene fibres, but is not the case for PVA fibres. For PVA fibres, slip hardening and the fibre strength need to be included. This model was advanced further by Lin et al (1999) and the modified model not only included the slip hardening and chemical bond, but also the effect of fibre rupture and the reduction of fibre strength when embedded at an angle with relation to the crack plane. This model is a useful link from the mechanical behaviour on the micro-level to the mechanical behaviour on the macro-level. This link will however not be made quantitatively in this dissertation. The experimental work that will be done on the micro-level will be a mechanistic investigation into the source of the time-dependant behaviour and not a quantitative investigation. For this reason this model will not be further elaborated in this dissertation.

For the second requirement, a steady state crack must be formed instead of an unstable Griffith type crack. The two types of cracks are shown schematically in Figure 2.7. This requirement is normally the more important of the two requirements,

i.e. if the volume of fibres is adequate for the second requirement, the first requirement is normally automatically satisfied.

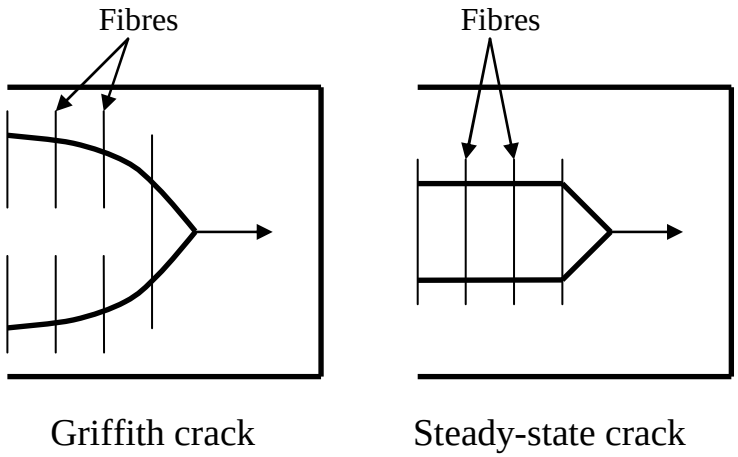

Figure 2.7 The growth of a Griffith type crack and a steady-state crack.

Using once again the fibre pull-out model of uniform shear resistance, shown schematically in Figure 2.4, the critical volume of fibres required, V_f^{crit}, to satisfy the second requirement can be calculated by balancing the matrix fracture energy, J_c, with the energy absorbing capacity of the fibres using fracture mechanics (Li 1993). This results in an equation for the V_f^{crit} as follows:

$$V_f{}^{crit} = \frac{12 J_c}{g \tau_0 \left(\frac{L}{d}\right) w_c} \qquad (2.4)$$

with J_c, the matrix fracture energy, also referred to as the crack tip energy and w_c, the crack width at which the highest fibre crack bridging resistance is found. The equation of w_c is:

$$w_c = \frac{\tau_0 L^2}{E_f d \left(1 + \frac{V_f E_f}{(1 - V_f) E_m}\right)} \qquad (2.5)$$

with E_m the stiffness of the matrix.

Lin and Li (1997) advanced this model to include slip-hardening, β, during fibre pull-out. The model was later modified further to include the effect of the chemical bond and the probability of fibre rupture (Lin et al 1999).

Using these models ECC materials can be engineered for specific applications by tailoring the fibre properties, interface characteristics and the matrix to acquire the desired behaviour.

2.2 Time Dependence of Cement-Based Materials

The time dependence of a cement-based composite is a complex phenomenon of which creep and shrinkage are the best known. Numerous articles have been published on the phenomena and sources of the time-dependant behaviour of cement-based materials. Some authors use a phenomenological approach to describe the mechanisms, an approach where the time-dependant deformations are measured on a macro-level and the results are related to different apparent mechanisms. A different approach to the time-dependant mechanisms is to look at the material at the micro-level. This is where the true mechanisms behind the time-dependant phenomena are to be found. This is a complex task due to the complexity and variability of the micro-structure of a cement-based composite and the sensitivity to different types of cement, cement extenders, aggregates as well as additives. The mechanisms on the micro-level are intertwined and can not be related directly to the phenomenological strain variation over time found on the macro-level.

In this section, the different mechanisms causing the time-dependant behaviour are discussed and a phenomenological approach to model the mechanisms is explored.

2.2.1 Shrinkage mechanisms

Shrinkage is a phenomenon which can be attributed to several mechanisms on the micro-level. Four phenomena are observed on the macro-level, namely drying shrinkage, hardening shrinkage also known as chemical shrinkage, autogenious shrinkage and carbonation shrinkage.

Drying shrinkage is traditionally defined as the volume or length change of a cement-based material when allowed to dry, i.e. the ambient relative humidity is

lower that the internal relative humidity and the migration of moisture is initiated. The mass reduction due to the loss of water from the material is not always directly related to the volume change found. The first stage of drying shrinkage, which is the loss of free water in the capillary pores, has little or no effect on the measured shrinkage. This causes a non-linear relation of the weight loss to the shrinkage. The higher the volume of the cement paste in the matrix, the more linear the relation between weight loss and shrinkage (Neville 1970). As the drying continues, the absorbed water in the capillary pores and gel is removed and causes shrinkage of the unrestrained hydrated cement paste. Part of drying shrinkage can also be caused by the removal of intercrystalline and intracrystalline water (Neville 1970).

Hardening shrinkage is defined as the volume change of the material, mostly in the plastic state, due to chemical reactions taking place during the hydration of cement. One of the most common reactions that take place in the normal hydration of cement paste is:

$$2C_2S + 6H_20 \quad \rightarrow \quad C_3S_2H_3 + 3Ca(OH)_2 \qquad (2.6)$$

To illustrate the possible volume change due to hydration, the volume reduction due to solidification of the free water in Equation 2.6 can be calculated theoretically to be up to 10.87 % (Tazawa et al 1995a). This volume reduction due to stochiometric calculations has been experimentally verified (Tazawa et al 1995a), but does not play a large role in the macroscopic volume or length change of the material in the hardened state as most of the chemical shrinkage is accommodated by internal porosities.

Autogenious shrinkage is defined as the macroscopic volume or length change when water transport is not allowed to or from the concrete or cement paste. In this way it differs from chemical shrinkage, as chemical shrinkage requires an abundance of water transfer to the material for full hydration to take place. Due to the hydration of the unhydrated cement, water is extracted from the capillary pores and the gel. This extraction of water causes the autogenious shrinkage. This is also known as self-desiccation. In the past, autogenious shrinkage has been often neglected and all volume change during drying has been attributed to drying shrinkage. It has been shown that lower water cement ratios cause higher autogenious shrinkage and less

true drying shrinkage (Tazawa et al 1995b). At a water cement ratio as low as 0.17 it has been shown that all the length change during drying can be attributed to the autogenious shrinkage and true drying shrinkage did not play a role (Tazawa et al 1995b).

Carbonation shrinkage occurs in the surface region of concrete and is due to CO_2 from the ambient environment reacting with the hydrated cement paste (Neville 1970). Due to the fixation of CO_2, the mass of the concrete increases while the carbonation shrinkage occurs. The first step of the reaction is the dissolving of CO_2 in the pore water, thus if the there is insufficient water in the pores, no carbonation shrinkage would occur.

2.2.2 Creep mechanisms

Creep can be defined as the increase of strain of a structure or material under a constant load or stress over a period of time. Many theories have seen the light in the previous century to describe the mechanisms of creep. The theories have been narrowed down by scholars to be a combination of three mechanisms (Neville 1970).

Firstly, creep is caused by the migration of the ever present water in the capillary pores in the matrix. This movement is provoked if stress is applied to the material. This is closely linked to a viscous flow theory for which the hydrated cement paste is believed to be a highly viscous liquid. This theory was first postulated by Thomas (1937). This model captures the creep behaviour with reasonable accuracy, especially below 50 % of the ultimate load in which range the creep strain is proportional to the applied stress.

The second mechanism is breaking and re-establishing of bonds on the micro-level. This is closely linked to the first mechanism of the movement of moisture in the pore structure. Due to the stress applied to the material, the gel structure is believed to collapse when internal stress peaks are formed. The micro-structure is then redefined due to the continuation of the hydration. This is an explanation for the permanent deformation associated with creep.

Lastly, the formation of micro cracks in the matrix in relative high stress conditions is believed to cause the non-linearity of creep. The stress peaks form internally which exceed the fracture strength, thus causing micro cracks. With a sustained load, these cracks grow and connect and may eventually cause a global

material failure on the macro-level, called creep fracture. The non-linearity of creep will be discussed later in this section.

2.2.3 Rate dependence and creep fracture

The decrease of the strength of a cement-based material with a decrease of loading rate is a well-known phenomenon. Much research has been done to quantify and model this reduction of resistance, e.g. Reinhard (1990) , Brühwiler and Wittmann (1990), Wittmann et al (1987), Körmeling (1986), Bazant and Gettu (1989), Fu et al (1991).

Together with this decrease of resistance the material also becomes less brittle with a lower loading rate. This is shown schematically in Figure 2.8. Typical responses for a flexural beam test using a normal testing rate are shown with a creep limit. The creep limit is defined as a test, flexural in this case, done over a long period of time, e.g. 15 years. The responses for rates between the shown rates will lie within the two responses shown in Figure 2.8. Another method of obtaining the creep limit is by applying a sustained load at different load levels. The deflection would increase until it reaches the creep limit as shown in Figure 2.8.

If a sustained load higher than the peak of the creep limit is applied, the beam would fail after time and this type of failure under sustained loading is called creep fracture. The peak strength of the creep limit is thus called the creep fracture limit and is shown in Figure 2.8. Zhou (1992) found the force-displacement point of creep fracture is close to the softening branch of the normal testing rate response for a specific set of notched concrete beams tested in flexure.

To date, no research has been done on the strain extension mechanisms causing creep and creep fracture of ECC. ECC could have a low creep fracture limit which would have an unexpected failure as a result. The point of creep fracture could also be much sooner than the softening branch of the normal testing rate as in the case of Zhou (1992) which would result in an unexpected loss of ductility.

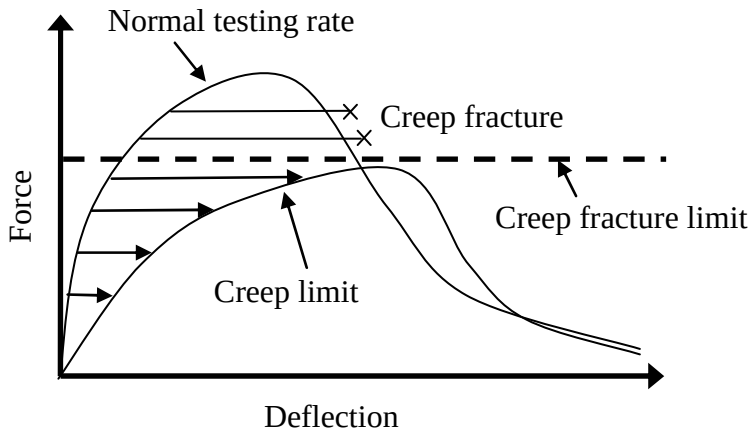

Figure 2.8 Schematic representation of creep fracture and a creep limit.

2.3 Phenomenological Approach to Creep Modelling

Most scholars in the past used phenomenological models to describe and define creep behaviour of concrete, e.g. Boltzmann (1876), Picket (1942). More recently, scholars have created more fundamental models which are based on the mechanisms rather than the phenomena, e.g. Bazant (1988). The phenomenological models are however useful as the creep and shrinkage strains are expressed in terms of phenomena on the macro-level, rather than relating the strains to the complex mechanisms on the micro-level. There are many discrepancies using this approach, as not all the possible mechanisms that occur can be captured with this limited approach.

The four most commonly used phenomena for the quantifying of the time-dependant behaviour is autogenious shrinkage, drying shrinkage, basic creep and drying creep. The term total creep will be used in this dissertation as the sum of the basic creep and the drying creep. These mechanisms will be independently defined.

Autogenious shrinkage, as described earlier, is the length change of a cement-based material if no moisture transport is allowed to and from a specimen. This is normally measured by sealing a concrete sample in a saturated state and monitoring the length change over time.

Drying shrinkage by definition is the length change of the material when it is allowed to dry. As discussed earlier, some autogenious shrinkage also occurs during drying, but due to the difficulty separating the two phenomena, drying shrinkage is defined as the only mechanism acting on the specimen in this unsealed condition. An

unsealed, fully saturated specimen is placed in an environment with a constant relative humidity and temperature to measure the drying shrinkage at this constant climate conditions.

Basic creep is defined as the length change over time in the direction of loading when the material, which is sealed to prevent any moisture interchange with the environment, is subjected to a sustained load. Autogenious shrinkage also occurs in this condition, but is by definition, stress independent. The basic creep is measured by applying a constant load to a sealed specimen and the length change of a separately measured autogenious shrinkage test is deducted from the reading to give the basic creep.

Ideally, when the measured basic creep is added to the measured drying shrinkage found in the same environmental conditions, the sum should be the same as the length change of a specimen that was allowed to dry and was subjected to a sustained load. This is however not the case as the measured creep is more than what is expected (Pickett 1942). This is shown schematically for compressive creep in Figure 2.9.

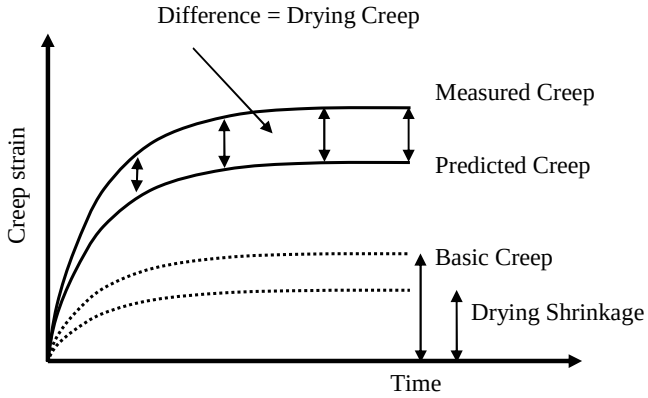

Figure 2.9 The Picket-effect for creep in compression shown schematically.

This discrepancy is attributed to an apparent mechanism, named drying creep. This apparent mechanism was first pointed out by Picket (1942), hence the reference to the Pickett-effect. He showed that when concrete is allowed to dry out before the commencing of a load, it shows almost no creep after the load application. However, when the concrete specimen is sealed to prevent any moisture migration from or to the specimen, the creep magnitude is proportional to the moisture content. And lastly, if the specimen is allowed to dry during loading, the creep is increased even further.

As the definition of drying creep suggests, it is the increase of creep when the material is loaded and allowed to dry at the same time. This is however a phenomenological approach and to understand the mechanisms behind this phenomenon, one needs to look at the physical processes occurring on the micro-level during these conditions.

The first possible mechanism that is believed to be the cause of this phenomenon is the surface micro-cracking of a specimen that undergoes unrestrained drying shrinkage (Pickett 1942, Wittman and Roelfstra 1980). They argued that when concrete is unrestrained and allowed to dry, the moisture content is not uniform throughout the specimen. This is shown schematically in Figure 2.10 a).

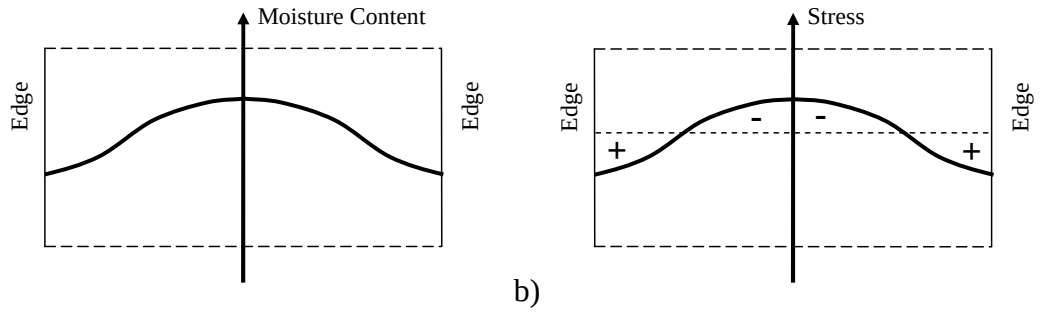

Figure 2.10 a) The moisture content distribution in a drying sample. b) The stress distribution caused the non-uniform moisture content in an unrestrained, unsealed specimen. Tensile stresses are defined as positive and compressive stresses as negative.

The varying moisture content in the drying specimen will cause a non-uniform shrinkage, as the decrease (or increase) of moisture causes shrinkage (or swelling). This non-uniform distribution will in turn cause internal stresses. Tensile stresses will form at the surface while compression forces will occur in the middle area. This is shown in Figure 2.10 b). Wittmann and Roelfstra (1980) showed that the tensile stresses as seen in Figure 2.10, can easily overcome the tensile strength of the concrete. This will cause micro-cracking close to the drying surface. Due to the inelastic behaviour of the micro-cracking, the micro-cracks will not close completely when a uniform moisture content condition is achieved over time. The length change due to shrinkage will then always be less due to these permanent micro-cracks than the true shrinkage length change.

When a uniform compressive force is applied to a specimen subjected to the same environmental conditions as in Figure 2.10, the stress distribution would look as in Figure 2.11. Note that for this example the effect of creep is neglected at first. It

can be clearly seen that no part of the specimen is subjected to tensile stress, thus no cracking will occur. The shrinkage that will be measured in this specimen will be more than the shrinkage measured in the unloaded drying specimen. This effect can successfully explain why the total deformation of an unsealed specimen loaded in compression is more than the superposition of the elastic deformation, basic creep and the drying shrinkage measured on an unrestrained, unloaded specimen.

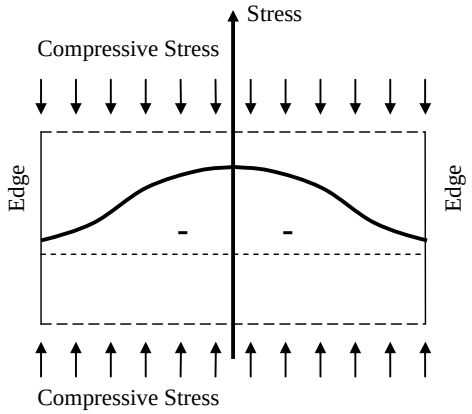

Figure 2.11 Stress distribution of a drying specimen which is under a constant compressive load and the effect of creep is neglected.

Wittmann (1993) showed that the opposite effect is also true for tensile loading. If the material is subjected to a tensile stress, the shrinkage measured on a loaded specimen is less than the shrinkage measured for the unrestrained specimen.

This explanation for the increase of shrinkage during compressive loading, defined earlier as drying creep, is a valid rationalization but only explains up to one half of the difference attributed to drying creep (Acker 1993). Glucklich (1968) was the first to suggest that a second mechanism exists which causes the Pickett-effect. Bazant and Chern (1985a, b) investigated this further and defined it as stress-induced shrinkage. This process is believed to be caused by the moisture migration in between the capillary pores and the gel pores. This is also known as micro diffusion as macro diffusion is the water migration between the larger pores which has been shown to have little or no effect on the shrinkage. This micro diffusion transports water between these micro pores and between micro pores and macro pores and has a direct influence in deformation rate of the cement gel. This transportation of water is accelerated when drying occurs, as well as when a stress is applied, thus causing a stress-dependant shrinkage.

Bazant and Xi (1994) were the first to publish results of an experiment that succeeded in distinguishing the mechanisms that cause drying creep. Different concrete beams were subjected to the same bending moment, but with different axial forces. The curvatures of the beams were monitored over time. They found that the drying creep is caused by two mechanisms, namely micro-cracking and stress induced shrinkage. Micro-cracking was found to increase at the start and then tends to decrease over a period of time while the stress-induced shrinkage was found to increase continuously.

In a phenomenological approach, stress-induced shrinkage, surface micro-cracking and drying creep can be accumulated in one phenomenon on the macro-level for the purpose of most time-dependant studies of concrete. This will also be done here and will be combined as drying creep.

Four macroscopic phenomena have now been defined, namely drying shrinkage (DS), autogenious shrinkage (AS), basic creep (BC) and drying creep (DC). To quantify these phenomena four different types of time-dependant tests have to be done. They are a sealed and unloaded (SU) test, an unsealed and unloaded (UU) test, a sealed and loaded (SL) test and an unsealed and loaded (UL) test.

The different phenomena applicable in the different tests are shown in Table 2.1. The basic creep and drying creep are defined as stress dependant and the others are considered to be stress-independent.

Table 2.1 The time-dependant phenomena applicable to the different tests.

	Time-dependant phenomena			
	Drying Shrinkage (DS)	Autogenious Shrinkage (AS)	Basic Creep (BC)	Drying Creep (DC)
Unsealed unloaded (UU)	x			
Sealed unloaded (SU)		x		
Unsealed loaded (UL)	x		x	x
Sealed loaded (SL)		x	x	

Using the definitions in Table 2.1, the values for the different time-dependant phenomena can be calculated using the measured time-dependant strains from the different tests as follows:

$$\varepsilon_{DS} = \varepsilon_{UU} \qquad (2.7)$$

$$\varepsilon_{AS} = \varepsilon_{SU} \qquad (2.8)$$

$$\varepsilon_{BC} = \frac{(\varepsilon_{SL} - \varepsilon_{SU})}{\sigma} \qquad (2.9)$$

$$\varepsilon_{DC} = \frac{(\varepsilon_{UL} - \varepsilon_{UU} - \varepsilon_{SL} + \varepsilon_{SU})}{\sigma} \qquad (2.10)$$

This method of identifying the different phenomena has been used with success in the past. For compression creep tests, the creep strain and the shrinkage strain are in the same direction. Therefore, the drying shrinkage and the basic creep strains are easily deducted from the bulk creep to find the drying creep. As shown in this section, drying creep is caused by two phenomena, i.e. surface micro cracking and stress-induced shrinkage. The effect of these phenomena would be in different strain directions if the loading is tensile, i.e. the micro-cracking phenomena would cause drying creep in the positive, tensile strain direction and the stress-induced shrinkage in the opposite direction. To distinguish these phenomena directly, experiments similar to Bazant and Xi (1994) would have to be performed.

Drying creep is defined as these two phenomena together, so the sum could be a positive or a negative strain, or as Kovler (1995) found, the sign changed from negative (compression) to positive (tensile) over a period of time. However in a later publication, Kovler (1996) found that after a correction was made for the swelling of sealed concrete the drying creep was found to be positive throughout the test. Bazant and Chern (1985a) concluded that the effect of micro-cracking in drying creep is short lived for compression, but for tensile and bending creep tests it plays a dominant role in the Pickett-effect.

2.4 Approaches to Creep Modelling

To include creep in any analytical or numerical analysis, a mathematical description is required. In Chapter 7 a time-dependant constitutive model for ECC is proposed and a mathematical model is derived to simulate the creep behaviour. As a basis for this model, the phenomenological characteristics of the total creep behaviour of cement-based materials on a macro-scopic level are presented here.

A typical strain-time graph of observed total creep is shown schematically in Figure 2.12. In the figure the load is kept constant for a period of time and then removed. As seen on the graph, the creep strain increases rapidly in the early stages after loading and then flattens to an asymptote called the creep limit of the material. Although the total creep deformation continuously increases in time, it is usually considered to stabilize after several years. When unloading the material, a certain part of the creep strain is recoverable. The rest of the creep deformation is thus a permanent deformation.

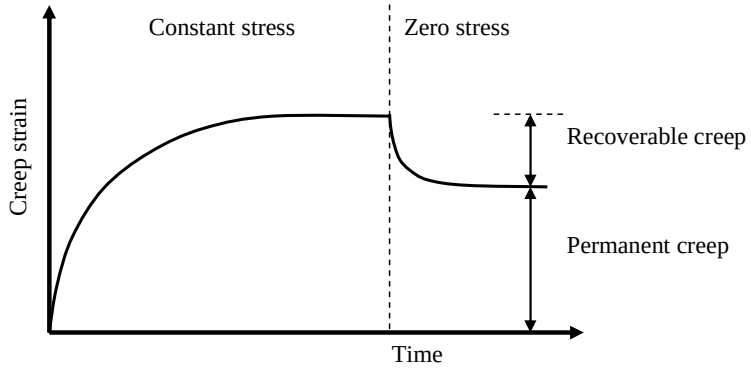

Figure 2.12 Basic creep behaviour over time.

To distinguish between recoverable creep and permanent creep, (Illston 1965a) unloaded creep specimens at different stages and then subtracted the recoverable creep from the total creep. This is shown schematically in Figure 2.13. In the context of this dissertation, the recoverable creep is called primary creep, while the permanent creep will be known as secondary creep.

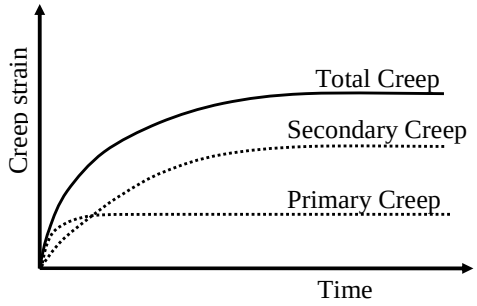

Figure 2.13 Components of creep strain.

It is important to note that the primary creep is dominant in the early stage of loading while the secondary creep becomes dominant in the medium to long term. Typical values of primary creep are found to be between 10 % and 25 % of the total creep in the long term (Neville 1970).

The magnitude of stress applied to a structure plays the primary role in the amount of creep strain that occurs. Figure 2.14 shows the effect of the load, expressed as a ratio of the ultimate strength, on creep strain as well as on the creep compliance, which is the creep strain per unit stress.

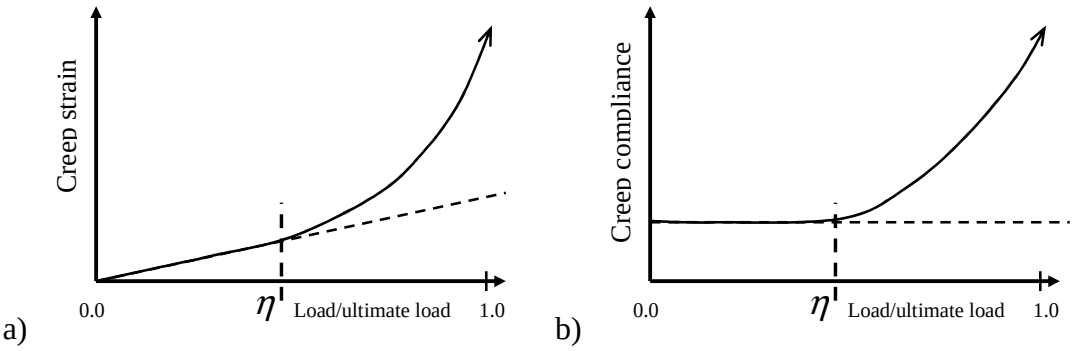

Figure 2.14 a) Creep strain in relation to the applied load. b) Creep compliance in relation to the applied load.

Up to a certain load ratio, referred to as the non-linear creep load ratio, η in this dissertation, the creep strain is proportional to the load. Past this point the creep strain increases exponentially with an increase in load. This non-linearity is believed to be due to micro cracks forming in the matrix and is not reversible (Neville 1970). This is eventually the mechanism that causes creep fracture. Creep fracture is the failure of the material under a constant load lower than the short term ultimate load. Another

part of creep is now identified, i.e. the added creep strain that causes the non-linear relation, and is referred to in this dissertation as tertiary creep.

Boltzmann (1876) was the first to show that superposition can be applied to creep strains. Superposition implies that the total creep strain at any point of time is the sum of all the creep strains caused by each stress and time increment that has occurred up to the specific point in time. This theory is based on the assumptions that creep is proportional to the stress and the creep strain caused by each stress increment acts independently on the material.

2.5 Concluding Summary

The understanding and characterisation of the time-dependant behaviour of any building material is important as it is required not for only further fundamental research on the material, but also for design guidelines for the structural use of the material. The investigation and understanding of the fundamental mechanisms that cause the time-dependant behaviour of any new building material such as ECC are required before any characterising of the time-dependant phenomena can begin. A few works have been published to date of the time-dependant behaviour of ECC (Douglas and Billington 2005, Yang and Li 2005 and Maalej et al 2005), but an in depth investigation into the mechanisms is still lacking, especially as no tensile creep tests have been done. The addressing of this issue forms the basis of the experimental research work that is presented in this dissertation. This is done with rate and creep tests on the macro-level and the structural-level. Tests on the single-fibre level are also done to investigate the mechanisms causing the time-dependant behaviour.

To understand and further explore the implications of the time-dependant behaviour, or even the static behaviour, numerical models that accurately predict the mechanical behaviour on a structural-level are required. No framework for the numerical modelling of the time-dependant behaviour of ECC exists and will be addressed in the second part of this dissertation.

CHAPTER 3

Experimental Rate Dependence of ECC

Any cement-based composite is prone to time-dependant behaviour and the mechanical properties of the material will change due to the change of the loading rate. The phenomena of creep and shrinkage are well known, even though not always understood. However, the phenomenon of the reduction of the peak resistance at a lower loading rate is not so well known. As an example of this, the peak resistance of notched plain concrete beams tested in flexure by Zhou (1992) at different deflection rates is shown in Figure 3.1. An approximate 45 % increase in peak resistance was the result of an increase in the deflection rate from 0.05 μm/s (peak load after about 80 minutes) to 50 μm/s (peak load after about 5 s).

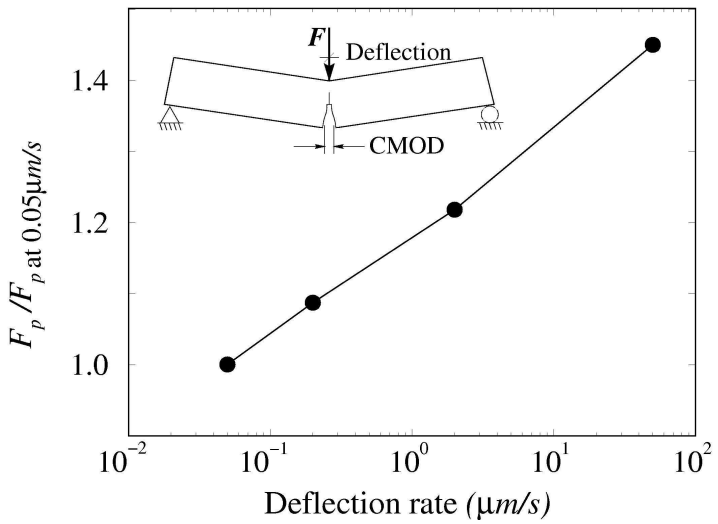

Figure 3.1 Concrete rate-dependent strength increase in quasi-static loading range (Zhou 1992).

The reduction of strength, or perhaps strain capacity in the case of ECC, is also an important issue that requires a thorough investigation. The reduction of strength or strain capacity could cause unexpected failure over time if a constant load is applied. The effect of the loading rate on the behaviour of ECC has only recently become a concern (Douglas and Billington 2005, Yang and Li 2005 and Maalej et al 2005) and the research of this subject is still lacking depth and understanding of the mechanisms causing the time-dependant behaviour.

In this chapter more light will be shed on the problem of the time dependence of ECC. Three different types of tests were done to show the influence of the loading rate on the macroscopic as well as the microscopic behaviour. The tests are tensile rate tests, flexural rate tests, as well as rate-dependant pull-out tests of single fibres.

3.1 Tensile Rate Tests

An uni-axial tensile test is the only type of test that can be used to obtain the tensile material parameters of ECC directly. Inverse calculation methods that deduce the tensile parameters from flexural test results, e.g. Østergaard et al (2005), have had limited success. The uni-axial tensile test setup is still a point of controversy as many research based opinions exists on how such a setup should look, e.g. fixed or rotational boundary conditions. To test pure tensile response, a gradient must be avoided. The standardising for tensile testing of ECC is currently under investigation (Mechtcherine and Schulze 2005).

However, a simple test setup was chosen for this research project, designed and built to not only produce reasonably accurate results, but also simplicity of testing which would allow a large number of tests on one day.

Even though tensile testing of ECC has been performed since the early 1990's, the effect of the loading or strain rate on ECC has only been published recently. Rate-dependant tensile tests have been by Douglas and Billington (2005), Yang and Li (2005) and Maalej et al (2005), but these results are not directly comparable to each other or to the results reported here due to the large difference in fibre types, matrix compositions as well as the shape of the test specimens. A summary of the test parameters used in these tests are shown in Table 3.1.

Table 3.1 Summary of rate-dependant tests on ECC.

Reference	Fibres used	Strain rates	Specimen
Maalej et al (2005)	PE and steel combined	$2x10^{-6}$ to $2x10^{-1}$	Coupon: 300x75x15 mm
Yang and Li (2005)	2 % PVA by volume	$1x10^{-5}$ to $1x10^{-1}$	Coupon: 220x75x12.7 mm
Douglas and Billington (2005)	2 % PVA by volume	$2x10^{-5}$ to $2x10^{-1}$	Cylinder: 51 mm diameter 102 mm height

The results of the aforementioned tests will be discussed together with the results of the rate tests in the following sections.

3.1.1 Test setup

A specimen shape and test setup were designed that objectively produce material properties, but at the same time are simple and practical. Flat dog bone shaped specimens were chosen for this research project as the intended use of ECC is thin structural members. They are cast horizontally in a steel mould with two removable studs in the middle of the enlarged end parts, as shown schematically in Figure 3.2. The specimens were cast with these studs in place. They create holes of 16 mm diameter that assist with the gripping of the specimens in the test setup. The dimensions of the specimens are shown in Figure 3.2 and the steel mould in Figure 3.3.

The mould has a lid which is applied during the vibration of the freshly cast ECC. Due to the high viscosity, the material has a so-called “stickiness” which makes it difficult to ensure a flat surface. With careful application of the lid a flat surfaced specimen is ensured every time.

The tensile tests were performed in a Zwick Z250 Universal Materials Testing Machine which has a capacity of 250 kN. Two clamps are fixed to the grips of the machine as shown in Figure 3.4. This method does not produce fully rigid boundary conditions, but has some rotational stiffness at the top and bottom. A 5 kN load cell is connected in line and is used to take the force readings during the test. The strain is

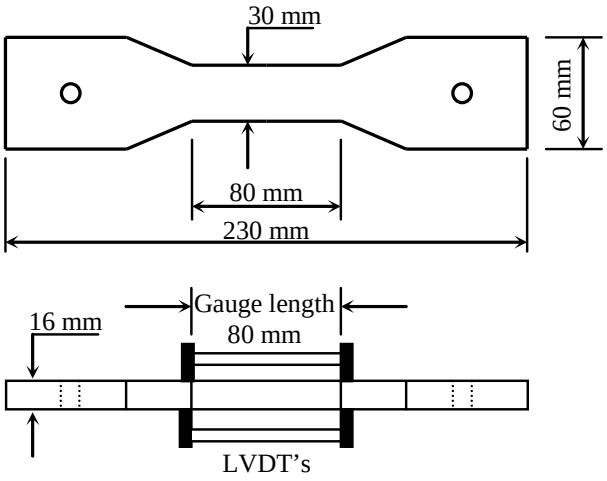

Figure 3.2 The dimensions of the flat dog bone specimen.

Figure 3.3 The steel mould for the flat dog bone specimens with the two removable studs.

measured by means of two LVDT's fixed on a removable aluminium frame, shown in Figure 3.4, which is attached over the gauge length during the test. The machine is controlled by the speed of the crossheads.

3.1.2 Experimental test program

Only one mix of ECC was used for all the experiments. The mix proportions are shown in Table 3.2. These proportions are calculated using the following ratios: water/binder ratio of 0.4, aggregate/binder ratio of 0.5. The binder consisted of CEM I 42.5 cement, a fly ash extender marketed as PozzFill by Ash Resources and Corex Slag of origin the Saldanha Steel Refinery in the Western Cape Province, South Africa used in the ratio of 45:50:5 by mass respectively. Note that even though not all

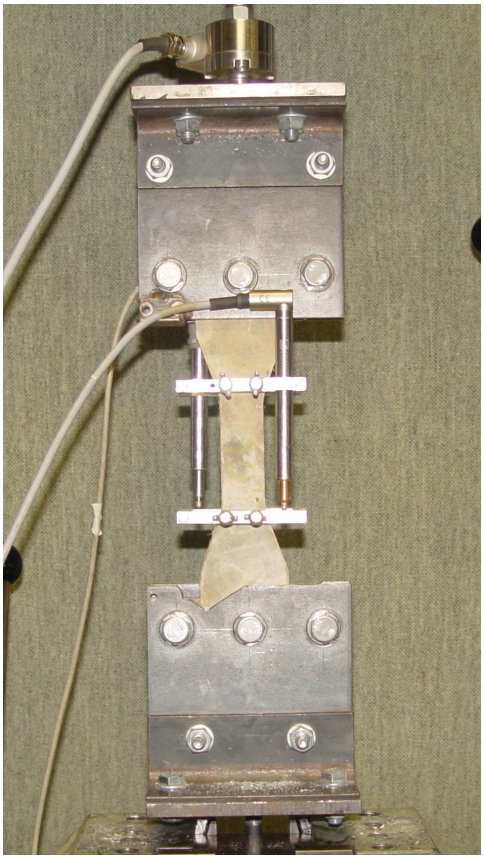

Figure 3.4 The tensile test setup in the Zwick Z250 and the aluminium frame with the LVDT's that were used to measure the strain over the gauge length.

Table 3.2 Mix proportions for the chosen ECC mix.

	Mass [kg/m^3]
Water	423
Cement	423
Fly ash	528
Corex slag	106
Fine sand	528
PVARecs 13	26.0

the fly ash reacts as binder due to its high content with relation to the cement, all the fly ash is included in the above ratios. PVA fibres with a length of 12 mm and a diameter of 40 μm were used. The fibres were supplied by Kuraray, Japan. Rheology modifying chemicals were added to ensure the correct workability.

Fine sand was used as the aggregate and its grading is shown in Figure 3.5. Please note for particle sizes above 105 μm, locally available dune sand, marketed as

Philippe sand was used and for the smaller particles, finely crushed Malmesbury Shale both easily available in the Cape Peninsula, Western Cape Province, South Africa. The different particle sizes were separated from each sand before the correct amounts of each specific particle size were mixed to ensure the correct grading.

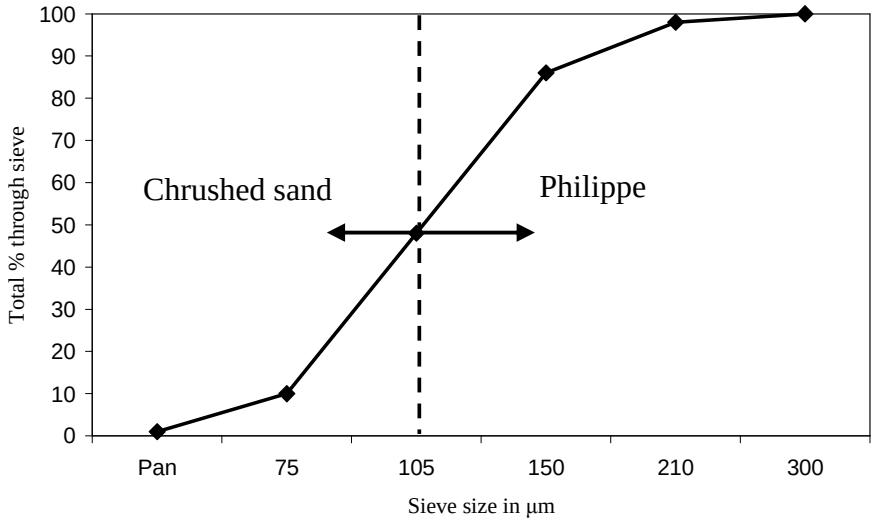

Figure 3.5 The grading of the sand used in the ECC mix.

Care was taken to ensure that the mixer was saturated with water, but dry to the touch before the execution of all the mixes. This ensured a minimum loss of water during the mixing process due to the absorption of the mixer. A Hobart type mixer with a capacity of 10 litres was used. The mixing procedure and mixing times are shown schematically in Figure 3.6.

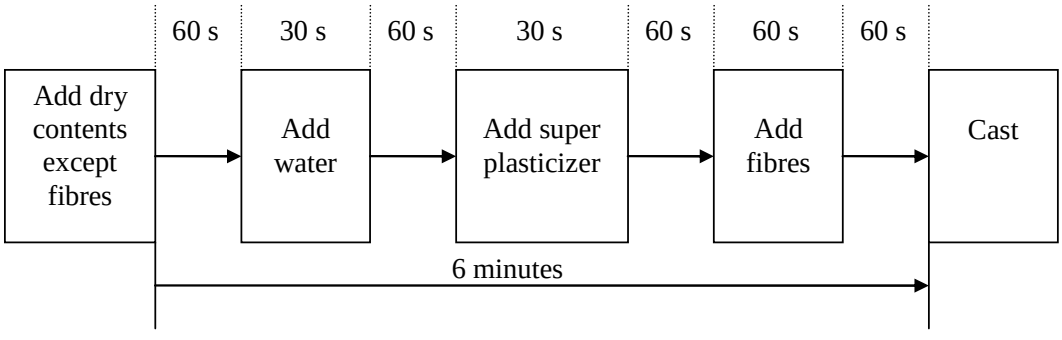

Figure 3.6 The mixing procedure with the time shown in seconds for each step.

The specimens were cast horizontally in steel moulds on a standard vibrating table. The correct amount of material was placed in the moulds while vibrating and a

steel lid was used to close the mould. The mould was then left to vibrate for another minute.

The moulds were taken to a temperature controlled room at 23˚C after casting. The specimens were left to cure in the closed moulds for 72 hours before they were stripped. The specimens were then submerged in clean potable water at 23˚C until an age of 13 days. Sikagard 63N, a brush applied sealant supplied by Sika SA, was used to seal the specimens directly after they were taken out of the water. All specimens were then tested at an age of 14 days. They were all sealed to minimise the effect of drying shrinkage during the testing. The effectiveness of this sealant is discussed in Chapter 4.

The strain rate was varied over four orders of magnitude ranging from $1.04x10^{-5}$ /s to $1.04x10^{-1}$ /s. At least five specimens were tested for every strain rate. The rates and the number of specimens tested are shown in Table 3.3.

Table 3.3 Test program for the tensile rate tests.

	Tensile rate tests				
Number of specimens	6	6	7	5	5
Loading rate [/s]	10.4µ	104µ	1040µ	0.0104	0.104

Another important characteristic is the spacing of the fine, multiple cracks. The importance of this characteristic will become clear in Chapter 5. To obtain the crack spacing, unsealed tensile test samples were tested at different strain rates to investigate the influence of the strain rate on the crack spacing. The specimens were tested unsealed as the cracks are not clearly visible if the specimen is sealed. Drying shrinkage would have an effect on the results, but is neglected as the test results are only used to determine the crack spacing.

The crack spacing is found by counting the cracks over the gauge length after the specimen has been tested. After unloading, the cracks can only be seen using a microscope. The number of specimens used for each strain rate is shown in Table 3.4.

Table 3.4 Test program for the determination of the crack spacing.

	Crack spacing tests				
Number of specimens	5	5	4	2	4
Loading rate [/s]	10.4µ	104µ	1040µ	0.0104	0.104

3.1.3 Results

The results of the rate tests are shown in Figure 3.7. The strain is expressed as a percentage and is measured over a gauge length of 80 mm. The stress is calculated as the force reading divided by the actual dimensions of the section in the gauge area.

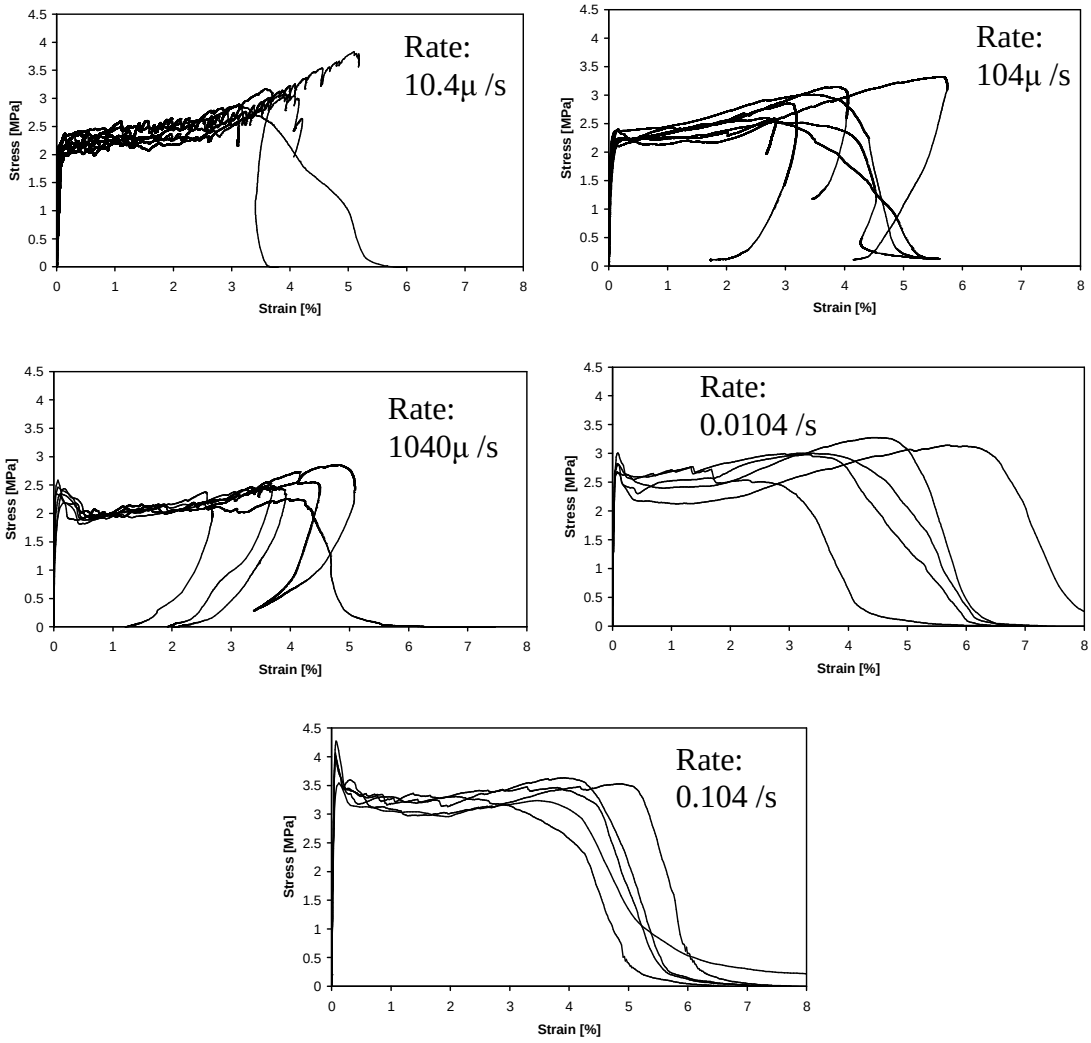

Figure 3.7 Direct tensile responses at different strain rates.

A phenomenon that was observed and which is more profound at the high rates, is a reduction of the stress after the first cracking point while the material still shows constant strain hardening after the initial loss of load. This phenomenon is not found at the lower rates. This type of behaviour is to be expected for ordinary FRC, but is not common for ECC. For ordinary FRC this drop can be ascribed to the load being shed unto the fibres after the crack initiation. This drop seen for the ECC tests is not this load shedding phenomenon, as the multiple cracking still continues after this

drop. The drop in stress capacity at high rates can however be explained when looking at the localised strain rates over the gauge length.

It is known that concrete strength increases at a higher strain rate (Zhou 1992, Fu et al 1991). Fu et al (1991) showed that the increase of strength is more profound in tension than in compression or flexure of concrete. The same trend is to be expected for the first cracking strength of the cement-based matrix of ECC. The average strain rate over the specimen will stay the same during the entire duration of the test, but differences can be seen in the local strain rates at specific points due to the crack formation.

This can be explained mathematically using the following assumptions:

- The average strain rate over the gauge length remains constant.
- A crack forms during a finite length of time to a constant crack width, Δ_c.
- The effect of a negative strain rate at a localised point which causes unloading is ignored. This would in fact even further reduce the local strain rate, as the unloading would result in the strain decrease to become larger.

Take the original gauge length as L, the average strain rate of the uncracked material as $\dot{\varepsilon}$, and the increase of gauge length during a finite time period as $\dot{\Delta}L$. Phase 1 of the test is defined as the time until the first crack occurs as shown in Figure 3.8 and $\dot{\varepsilon}$ can then be expressed as:

$$\dot{\varepsilon}_{Phase1} = \frac{\dot{\Delta}L}{L} \qquad (3.1)$$

During the second phase which is the period when the crack initiates and grows, $\dot{\varepsilon}$ has to be adjusted as $\dot{\varepsilon}$ is the average strain rate of only the uncracked area. $\dot{\varepsilon}$ will then be reduced during the formation of the crack, as follows:

$$\dot{\varepsilon}_{Phase2} = \frac{\dot{\Delta}L - \dot{\Delta}_c}{L} \qquad (3.2)$$

This results in a sudden decrease in the average strain rate over the uncracked material, thus causing a reduction in cracking strength. The average strain rate will not

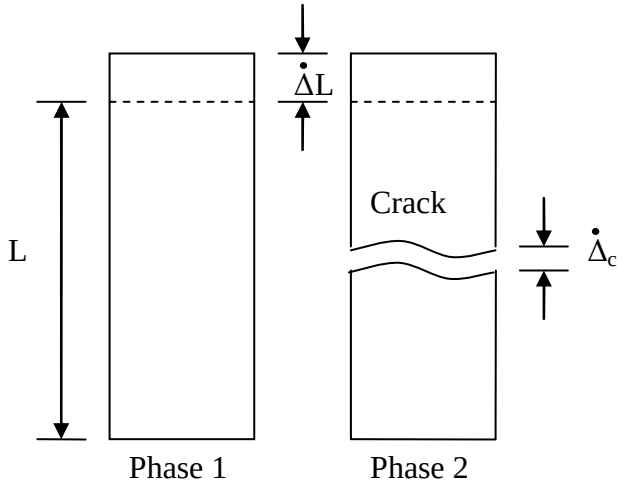

Figure 3.8 The schematic description of the decrease of strain rate after cracking.

be increased again as long as new cracks are forming, which occurs during the strain hardening phase

As a numerical example, a $\dot{\Delta}L$ of 8 mm/s and a Δ_c of 50 μm, which corresponds to the strain rate of the fastest test as well as an estimated crack width for ECC during strain hardening respectively. The time required to form a crack is unknown, but for this example a time of 10 μs is chosen. The gauge length, L, is taken as 80 mm. Using these values, the strain rate during the first phase can be calculated as 0.1 /s using Equation 3.1 while during cracking, the second phase, the strain rate decreases to 0.035 /s. This shows a reduction of more than 60 % of the average strain rate. A graph is shown in Figure 3.9 that shows what effect the crack formation time has on the reduction of the strain rate as in the aforementioned example. It shows clearly that there is a reduction in strain rate and shows the strain rate could even become negative at a crack formation time of less than 0.005 s.

Due to the simplifying assumptions, this method does not give accurate results but clearly indicates that a drop in strain rate does occur when a crack forms in the matrix. This drop of strain rate will result in a lower cracking strength.

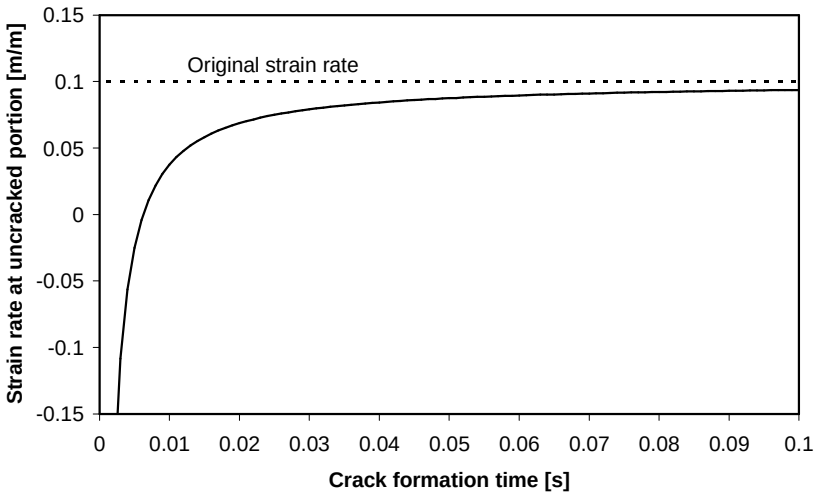

Figure 3.9 A parameter study on the crack formation time to show its influence on the reduction of strain rate.

When determining the first cracking strength of the material from the test results, the definition of the first cracking point is used as shown schematically in Figure 3.10 for the high and low strain rates to take into account the aforementioned phenomenon. It is acknowledged that micro-cracking does occur before the determined first cracking point, but this method is chosen to objectively determine the onset of the strain hardening phase. The more classical definition is to find the point where the response deviates substantially from the virgin elastic behaviour. This method is not appropriate for the lower strain rate tests due to the strong non-linear behaviour caused by creep and micro-cracking. For the higher strain rates, the first cracking stress is taken as the peak value before the stress reduction after the first crack.

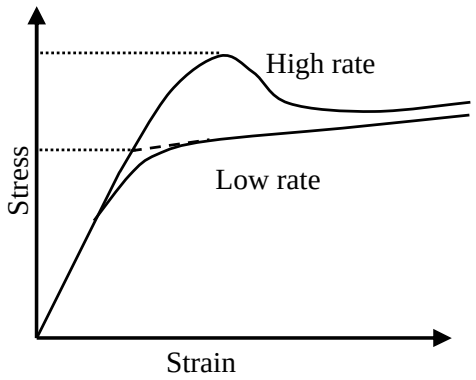

Figure 3.10 The definition for the first cracking stress for the high and low strain rate tests shown schematically.

Due to this phenomenon of stress reduction after the first crack for the high rates, the stress resistance value seldom reaches the first cracking stress after this initial drop for the high strain rates. For this reason the ultimate strength of the material is defined as the highest stress reached after the stress drop coinciding with the first cracking point and not the overall highest stress resistance, as this would result in the same value as the first cracking strength.

The E-modulus is difficult to define, as micro-cracking occurs in tension that causes non-linear behaviour as shown in Figure 3.11. The effect of the micro-cracking is more profound at lower strain rates. A pragmatic approach was used to objectively determine the E-modulus, namely to take the initial slope of the test results as shown schematically in Figure 3.11.

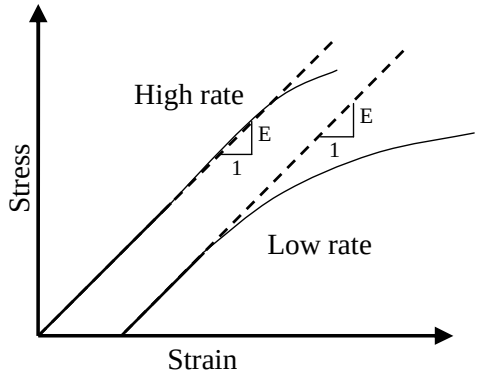

Figure 3.11 The definition of the E-modulus for high and low strain rates shown schematically.

Graphs summarizing the first cracking stresses, ultimate stresses, ductility (which is defined as the strain at the point of the ultimate stress) as well as the E-moduli are shown in Figure 3.12 a) to d). The average values are plotted with min-max values to indicate the spread of the values.

The crack spacing was determined by dividing the number of cracks visible with a small, handheld microscope in the gauge area by the gauge length. The results are shown in Figure 3.13 as a function of the strain rate.

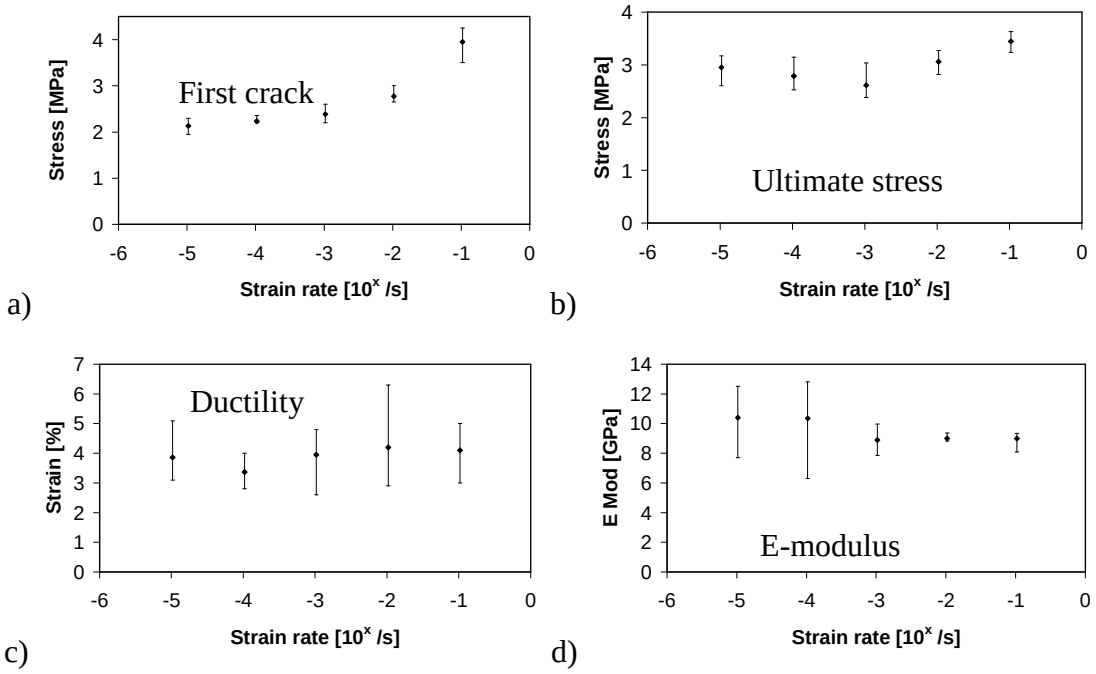

Figure 3.12 a) The first cracking strength. b) The ultimate stresses. c) The ductility. d) The E-moduli.

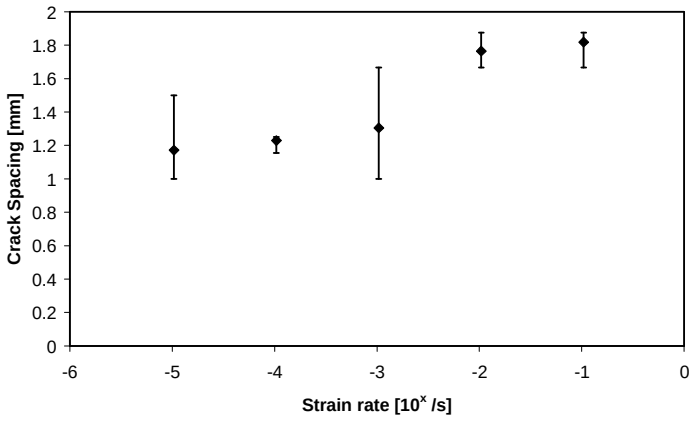

Figure 3.13 The average crack spacing for the different strain rates.

3.1.4 Discussion

It is apparent from Figure 3.7 that a typical ECC strain hardening response was obtained for all specimens in direct tension. A clear distinction could be made between the elastic, strain hardening and the strain softening phase. Moreover, reasonable repeatability was found, indicated by for instance a coefficient of variation of less than 10 % in ultimate tensile strength at all rates.

A rate-dependant trend was found for the first cracking strength. The cracking stress increases with an increase of the strain rate, especially when nearing dynamic

strain rates. This type of trend is to be expected for a cement based material (Fu et al 1991). The strength increased by up to 70 % from the lowest strain rate to the highest. Yang and Li (2005) also found an increase in the first cracking strength of ECC, but did not quantify the increase. Douglas and Billington (2005) quantified the increase to be only 12 % over the same strain rate increase as in this research project.

For the ultimate strength, a steady result was found averaging at 3.0 MPa. There is however an increase towards the higher strain rate. The increase is 17 % if the highest strain rate is compared to the lowest strain rate. This is significantly different to the results of Yang and Li (2005), Douglas and Billington (2005) and Maleej et al (2005) who found an increase of 70 %, 76 % and 90 % respectively.

A significant difference is found in the two trends of the first cracking stress and the ultimate stress, an increase of 70 % and 17 % respectively. The difference is ascribed to two different mechanisms controlling these values. The first cracking strength is dependant on the cement-based matrix strength which is rate-dependent as shown by Zhou (1992) and Fu et al (1991). The ultimate strength is dependant on the fibre strength rate dependence and the fibre-matrix interface. These mechanisms will be investigated later in this chapter when single fibre pull-out tests are reported.

The ductility of the material, which is also referred to as the strain capacity is shown here not to be influenced significantly by the strain rate. An average of 3.9 % is found over all the strain rates. No reduction of the ductility was found as in the case of Yang and Li (2005) and Douglas and Billington (2005) who found a decrease of 83 % and 53 % respectively. Maleej et al (2005), however, also found no change in the ductility if the strain rate is changed.

A steady E-modulus of about 9.2 GPa was found for the material throughout the loading rates. The method used for determining the E-modulus does not include the effect of the non-linear behaviour which is more profound in lower loading rates as shown schematically in Figure 3.11. No rate effect is thus found in the E-modulus values.

The crack spacing was shown to be dependant on the strain rate. With an increase of strain rate, the crack spacing increased. At the lowest strain rate the average crack spacing was found to be 1.2 mm and at the highest strain rate it was 1.8 mm. The ductility remained constant with an increase of strain rate and a logical conclusion can be made that due to the reduction of the number of cracks over the gauge length, the crack width increased with an increase of loading rate.

3.2 Flexural Rate Tests

3.2.1 Test setup

Three point flexural tests were performed to investigate the effect of the strain rate on the flexural response of ECC. These tests were done in the Zwick Z250 machine as in the case of the tensile tests. The Zwick 3 point bending setup was used which has a capacity of 250 kN. A photo of this setup is shown in Figure 3.14.

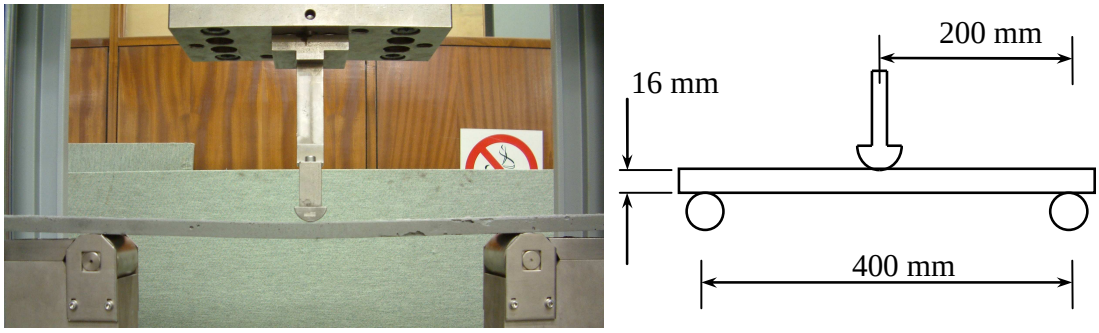

Figure 3.14 Three flexural test setup and the bending specimen.

The beam specimens were 16 mm thick and cast in steel moulds on a vibrating table. During the vibration a steel lid was placed on the mould to ensure a flat surface of the specimens. The steel mould as well as the dimension of the beams are shown in Figure 3.15. The beams were tested in the same vertical orientation as during casting, i.e. the top surface during casting was the top surface during testing.

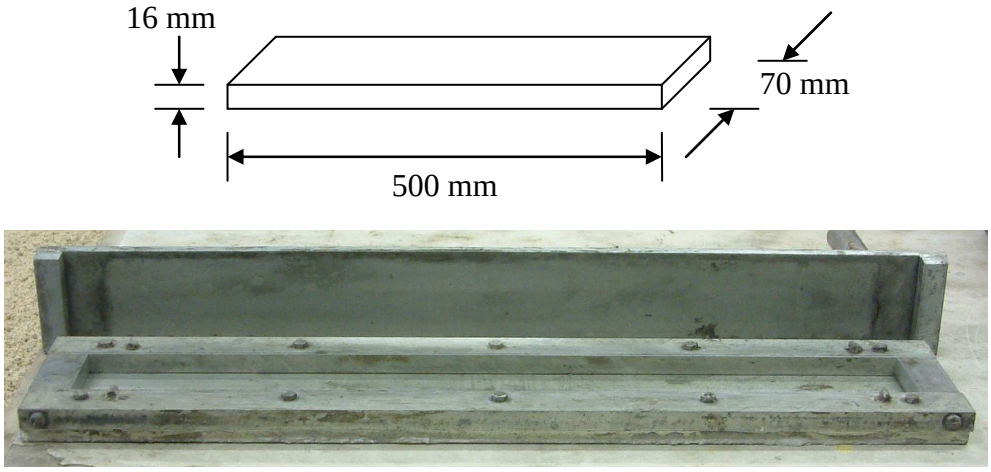

Figure 3.15 The beam dimensions as well as the steel mould.

The tests were controlled by means of the displacement rate of the crossheads and the load and deflection were measured using the internal load cell and the displacement of the crossheads of the Zwick.

3.2.2 Experimental test program

Exactly the same mix proportions and mixing procedure were used as in the case of the tensile tests in Section 3.1. The specimens were also sealed before testing to minimize the effect of shrinkage, even though it should have insignificant effects on the results as there is no restriction on any axial length change.

Flexural tests were done over a range of almost four orders of magnitude of the deflection rate. The deflection rate varied from 3.3 μm/s to 8.3 mm/s. The test program is shown in Table 3.5 together with the number of test specimens tested.

Table 3.5 Test program for the flexural rate tests.

	Flexural rate tests				
Number of specimens	5	4	6	5	5
Loading rate [/s]	3.3 μm	8.3 μm	83.3 μm	0.83 mm	8.3 mm

3.2.3 Results

The results of the flexural rate tests are shown for all the deflection rates in Figure 3.16.

The important characteristics determinable from a flexural test result are the ultimate flexural strength commonly expressed as the modulus of rupture (MOR), the first cracking strength as well as the deflection at the ultimate load. Even though these parameters could not directly be used as ECC material parameters as they strongly depend on the geometry and the boundary conditions, they are useful in this case for investigating the rate effect of ECC in a structural sense as a strain gradient represents a more general structural condition.

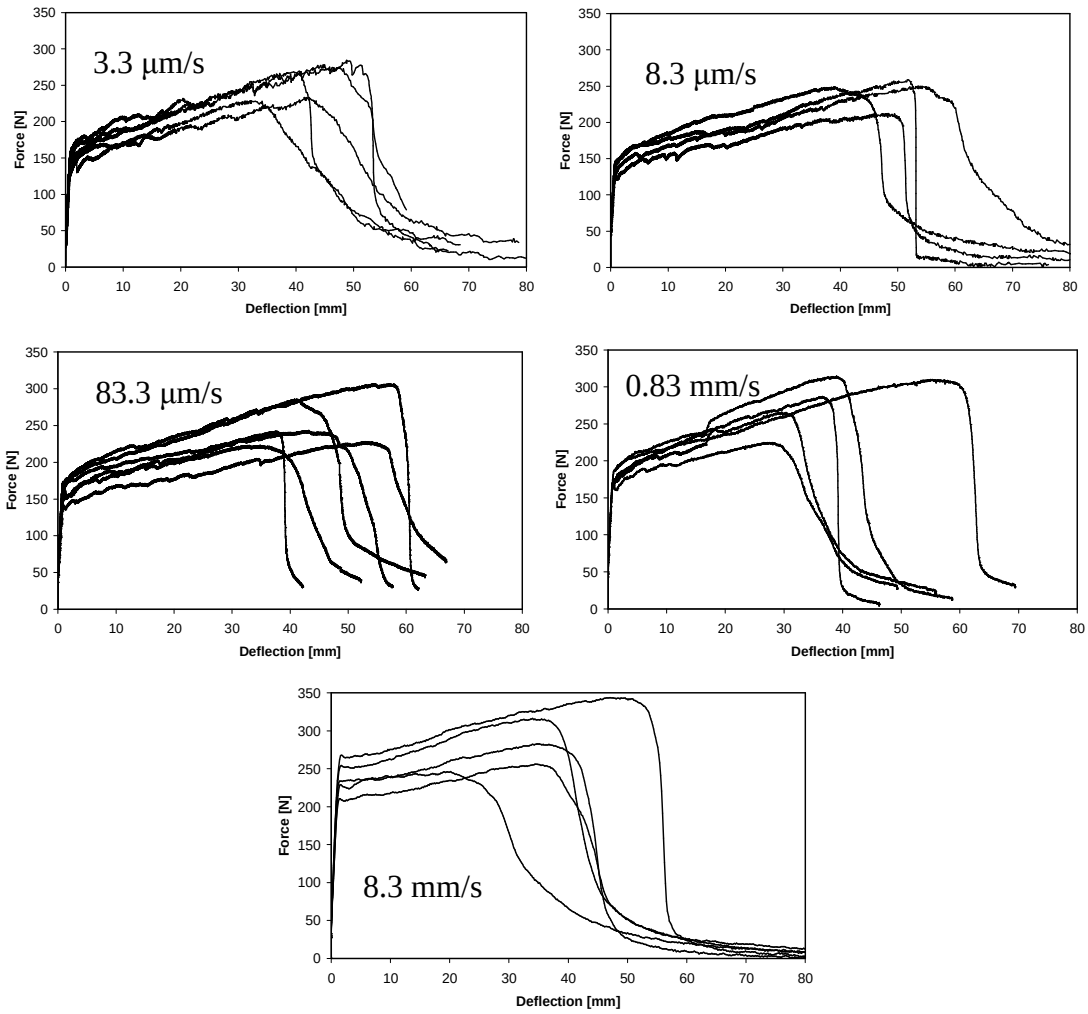

Figure 3.16 Results of the flexural deflection rate tests.

The three aforementioned characteristics were found for the tests and are shown in Figure 3.17. The averages together with the maximum and minimum values for each deflection rate are shown. The first cracking strength is found with the same method as for the direct tensile tests. The ultimate strength is determined from the highest force resisted by a specimen and the ultimate deflection is the coinciding deflection of the ultimate strength. The ultimate strength in Figure 3.17 b) is expressed as a force in Newton on the left axis and the MOR on the right axis. The definition of the modulus of rupture as used for Figure 3.17 b) is the tensile stress resistance that the material would require to resist the applied load if the material behaviour was purely elastic. This can be calculated from:

$$MOR = \frac{3}{2}\frac{PL}{bh^2} \qquad (3.3)$$

with P the applied force, L the distance between the supports, b the depth of the beam section and h the height of the section.

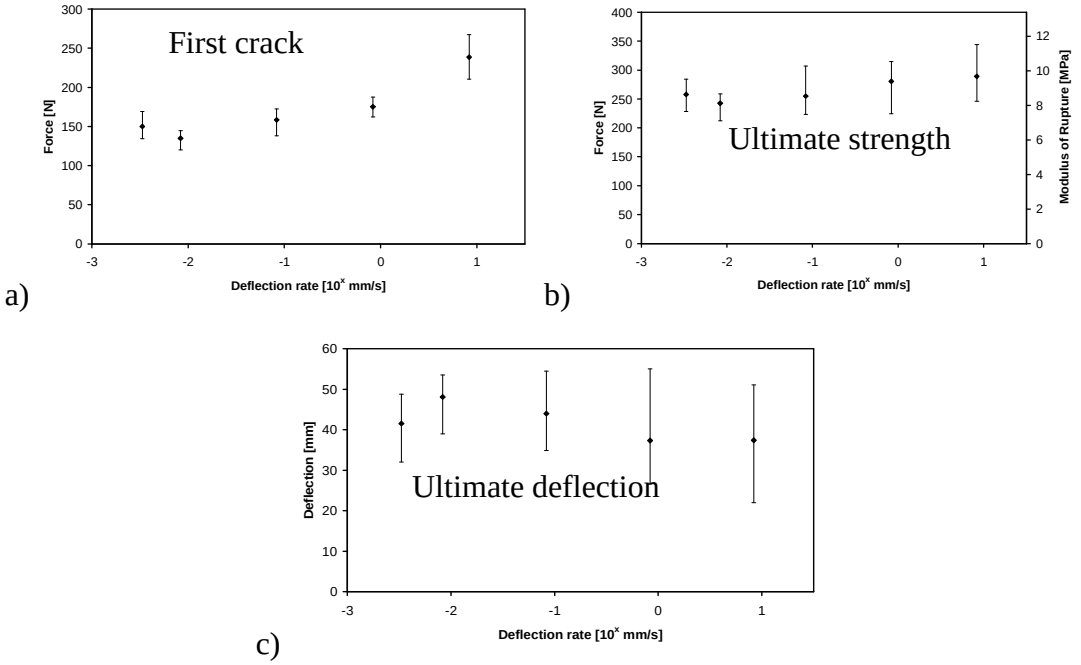

Figure 3.17 a) The first cracking force. b) The ultimate strength. c) The deflection corresponding to the ultimate force.

3.2.4 Discussion

To the author's knowledge, no results of flexural rate tests on ECC have been published so the results could not be compared to other work. Significant trends have however been found.

A similar trend of the first cracking strength rate dependence has been found as for the tensile results. The first cracking resistance of the beams increased by 77 % over three orders of magnitude. This is comparable to the first cracking strength of the tensile tests which increased 70 %. These values are however not directly comparable to the tensile results. For a better comparison of the first cracking trends of the tensile and flexural results, the beam results may to be transformed to stresses and strains using elastic bending theory.

In the elastic range, the strain rate of the bottom edge of the beam can be related to the deflection rate by:

$$\dot{\varepsilon} = \frac{6h}{L^2}\dot{v} \qquad (3.4)$$

with ν the deflection of the beam. The dot indicates the derivative with regard to time. Equation 3.4 can be found using the Euler-Bernoulli law for elastic bending. The applied force can be related to the stress at the bottom edge of the beam using Equation 3.3. The results of the first cracking strength of flexural rate tests can now be compared directly to the tensile rate tests if linear elasticity is assumed up to this point. The result is shown in Figure 3.18.

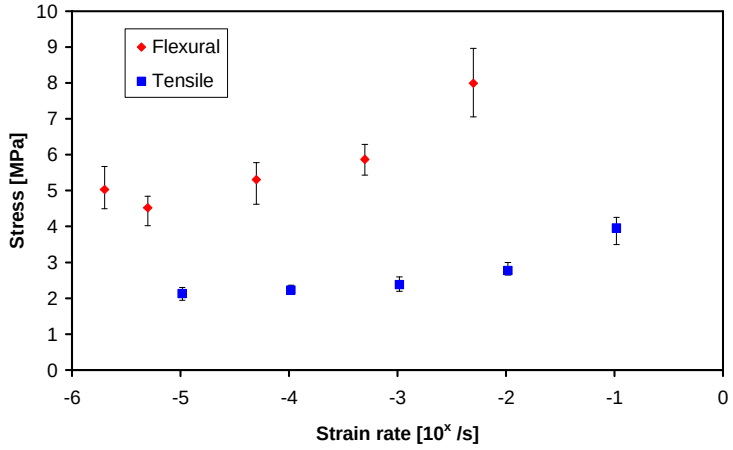

Figure 3.18 The comparison of the first cracking strengths of the tensile rate tests and the flexural rate tests.

A similar trend was found for the increase of the first cracking strength with an increase of the strain rate. Note however that the flexural cracking stress is more than double the tensile cracking stress. The rate of increase of stress at high rates is also more profound for the flexural tests. The calculation of the flexural cracking stress using the MOR equation assumes perfect elastic behaviour. At the time of the first crack of the flexural test, the stress gradient is not linear due to the fracture energy dissipation and a higher than actual tensile stress value is calculated. This explains the higher tensile strength calculated for the flexural tests compared to the tensile tests. The higher rate of increase of the flexural stress can be ascribed to the combination of the tensile stress and fracture energy that both increase with a higher strain rate.

An increase of 19 % of the ultimate strength was observed with an increase of the deflection rate. This is comparable to the 17 % increase found for the ultimate strength in the direct tensile tests. These results combined with the first cracking

strength shows that a steady rate effect can be seen for the strength in flexure as well as in tension.

The ultimate displacement, i.e. the displacement corresponding to the ultimate load also referred to as the flexural ductility, shows a decline with the increase of the deflection rate. This is significantly different to the direct tensile case as the ductility stayed constant throughout the different strain rates of the direct tensile tests. The flexural ductility decreased by 26 % over the range of deflection rates tested. This decrease in ductility which was not found in the tensile behaviour can be explained by looking at the spread of multiple cracking in the beam.

The centre area of the beam undergoing flexural testing is shown schematically in Figure 3.19. Note that the figure is not intended to be to scale. L_m is defined, as shown in Figure 3.19, as the length at the bottom of the beam that undergoes multiple cracking. It can also be defined as the area of which the tensile stress exceeded the first cracking tensile strength of the material. It follows that the larger L_m, the higher the ductility of the flexural test as the multiple cracking is the reason for the ductile behaviour in bending. For the higher deflection rate tests, higher strain rate occurs at the bottom of the beam. Due to the increase of cracking strength of the matrix with an increase of strain rate as shown in section 3.1, the area of multiple cracking will be less and thus have less flexural ductility as a result. It can thus be concluded that the higher the deflection rate, the less ductility can be expected even if the tensile ductility does not change with the increase of strain rate. This postulation is elucidated numerically in Chapter 6.

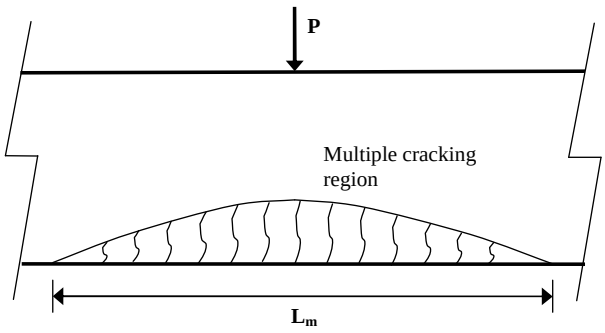

Figure 3.19 Graphical representation of the area of multiple cracking in a flexural test.

3.3 Rate Tests of Single Embedded Fibres

Pull-out testing of PVA fibres embedded in a cement-based matrix is not an easy task. The maximum tensile force is below 2 N, thus a precise and accurate test setup is required to do these tests. Accurate force measurements are required if the interfacial parameters, i.e. τ_0 and β are to be distinguished. These interfacial parameters were defined in Chapter 2.

A method was developed by Wang et al (1988) to determine the critical length of embedment of fibres in a matrix. Small polymeric or steel fibres embedded in a matrix have a critical embedment length, as in the case of steel reinforcing in concrete. The critical length is defined as an embedment length beyond which fibre rupture will occur and a shorter embedment length would lead to fibre pull-out. To find the critical embedment length for a specific fibre type, the fibres are cast in a matrix at different embedment lengths and then pulled out simultaneously as shown in Figure 3.20 a). A typical result is shown in Figure 3.20 b) with L_c the experimentally determined critical embedment length. The results do not shed light on the debonding process, as some of the fibres that ruptured could have debonded fully, but due to the slip hardening phenomenon described in Chapter 2 caused them to rupture during pull-out.

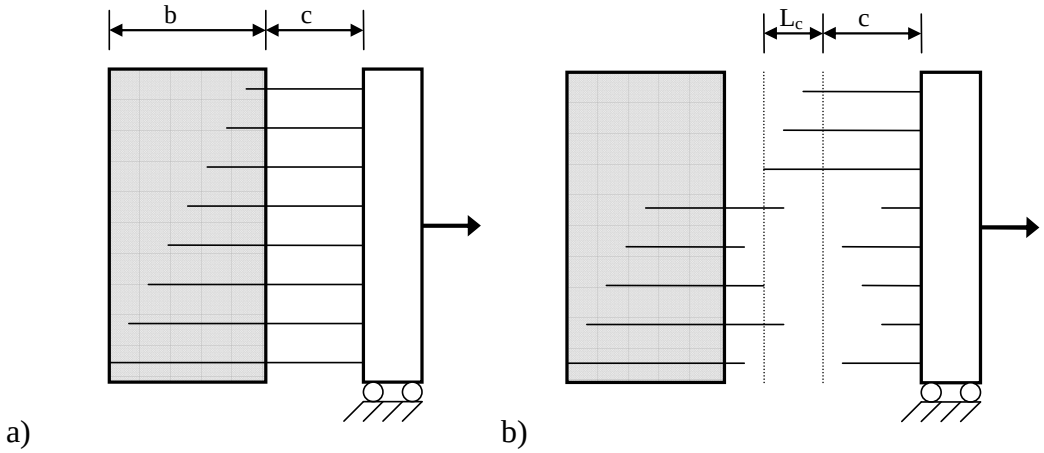

Figure 3.20 Experimental determination of the critical fibre length (Wang et al 1988).

This method can also be used to determine the original interfacial bond strength, τ_0, in an indirect way as was done by Li et al (1990). This is done by balancing the fibre strength (which is known, usually specified by the supplier) with the interfacial bond for the critical embedment length and assumes that the interfacial shear

resistance, τ_0, is uniformly distributed along the embedded length of the fibre. This method does not take into account the chemical bond, slip-hardening effect or the apparent strength of the fibres, which causes this method to be inaccurate for hydrophilic fibres. Kanda and Li (1998) have found that the strength of high strength hydrophilic fibres is reduced if they are embedded in a cement-based composite and called it the apparent strength of the fibres. Typical reduction ratios are 75 % for 14 μm diameter PVA fibres (Kanda and Li 1998) and 60 % for 44 μm diameter PVA fibres (Redon et al 2001). This phenomenon of apparent strength is found to increase if the embedment angle is increased and is believed to be caused by surface damage during the debonding and pull-out process. The rupture always occurs at a portion of the fibre that was originally embedded in the matrix. The indirect method is thus not an accurate method for calculating τ_0 for PVA fibres.

The two direct methods found in the literature for single fibre pull-out tests from cement-based matrixes are shown in Figure 3.21. The method shown in Figure 3.21 a) has been found to be effective for hydrophobic fibres as the critical embedment lengths are normally more than 6 mm (Li et al 1996) due to a low τ_0. The specimens are cast with the fibre carefully held to the correct embedment length. This will only work for stiff fibres as it is very difficult to ensure an embedment length with flexible fibres.

For PVA fibres an embedment length less than 1.2 mm is required (Redon et al 2001; Lin and Li 1999; Kanda and Li 1998; Yang and Li 2005; Li et al 2002) to ensure fibre pull-out without fibre rupture, therefore another method was developed to ensure an accurate embedment length of this magnitude. This alternative test setup is shown in Figure 3.21 b) and the casting setup is shown in Figure 3.22. After curing, the specimen is cut to ensure a short embedment length as shown in Figure 3.22 with dimensions of about 10 x 5 mm by the required embedment length.

The last mentioned test setup was adopted in this research program and will be described in more detail in the next section.

3.3.1 Test setup

To perform pull-out tests of a single PVA fibre with a diameter of 40 μm a precise and accurate test setup is required. The test setup used in this research project

.

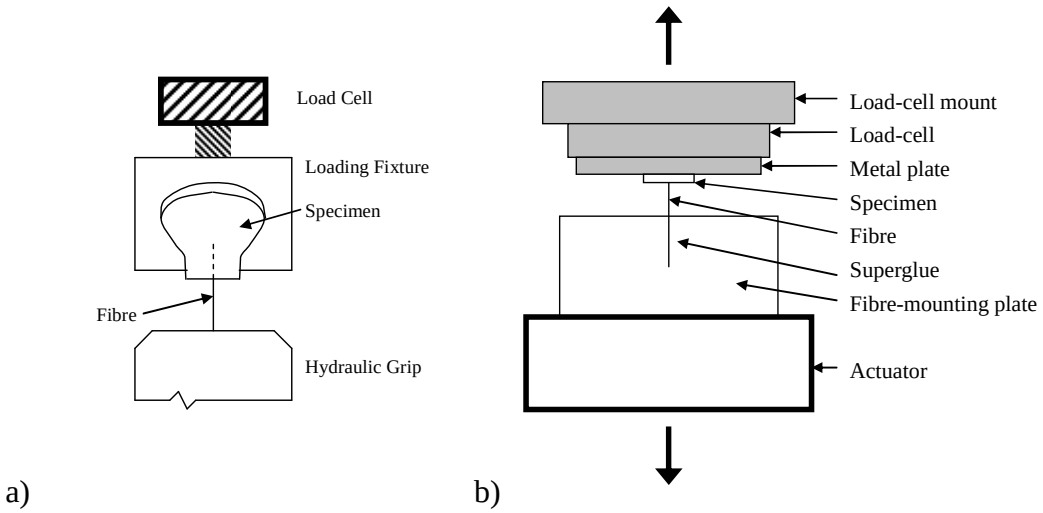

Figure 3.21 Two types of direct single fibre pull-out tests with a) from Li et al (1996) and b) from Kanda and Li (1998).

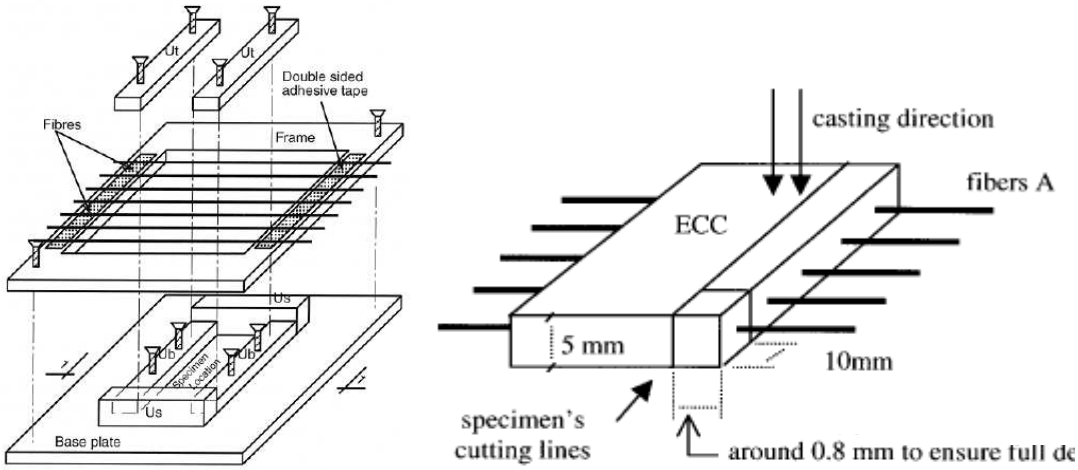

Figure 3.22 Casting setup for small (smaller than 3 mm) embedment length of fibres (Katz et al 1996).

is based on the test setup of Kanda and Li (1998). The mould design is based on the work of Katz and Li (1996). The setup was briefly introduced in the previous section

The casting mould used for test samples is shown in Figure 3.23. The fibres are drawn in for illustration purposes as they are too fine to be seen on the photo. The distance between the fibres is 15 mm and the thickness of the specimen is 15 mm.

The test samples are cut from the specimen shown being cast in Figure 3.23. The dimensions of the specimen are shown in Figure 3.24

The tests were done on a Schenk 250 kN Universal Testing Machine with a total stroke of 250 mm. A 10 N HBM load cell was mounted on the top crosshead with a

fibre gluing plate fixed on the load cell. On the bottom platen a base plate was fixed on which the test sample was glued. A photo of the test setup is shown in Figure 3.25 with a graphic illustration in Figure 3.26. The testing sample was glued to the bottom

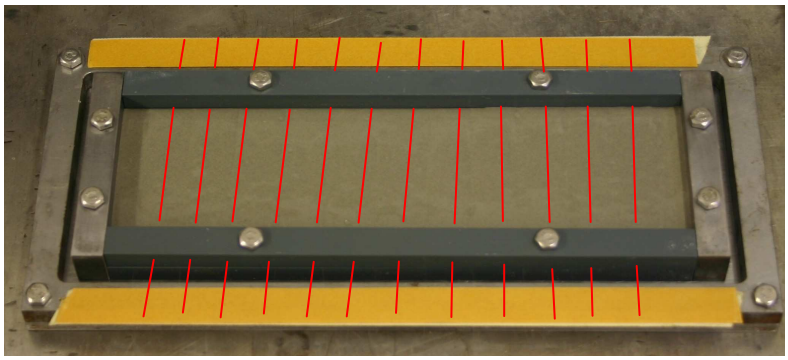

Figure 3.23 The mould used for the casting of the single fibre pull-out specimens. The fibres are drawn in with red lines as they are too small to be seen in the photo.

.

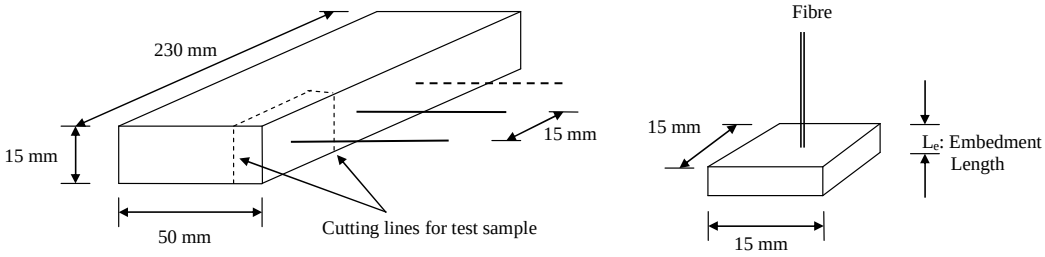

Figure 3.24 a) The cast specimen. b) The dimensions of the cut specimen that becomes the test sample.

base plate using a two component glue, X60 supplied by HBM. Special care was taken to ensure that no glue came in contact with the end of the embedded fibre as it could influence the pull-out force. The loose end of the fibre was carefully glued to the fibre mounting plate with a “superglue” type glue called Z70 also supplied by HBM. This was all done while ensuring that no force was applied to the fibre that could cause debonding or pull-out. The force was monitored during the gluing process and if a force was applied that could have damaged the test sample, the results of that test were disregarded. A gap of about 1 mm was ensured between the bottom of the fibre mounting plate and the test sample during the gluing process.

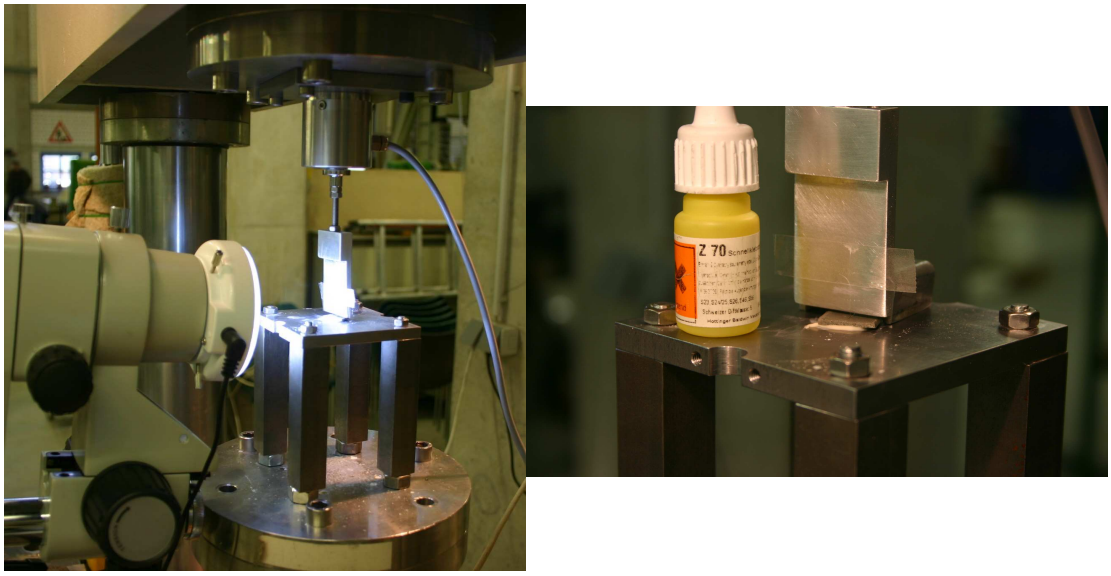

Figure 3.25 The single fibre pull-out test setup.

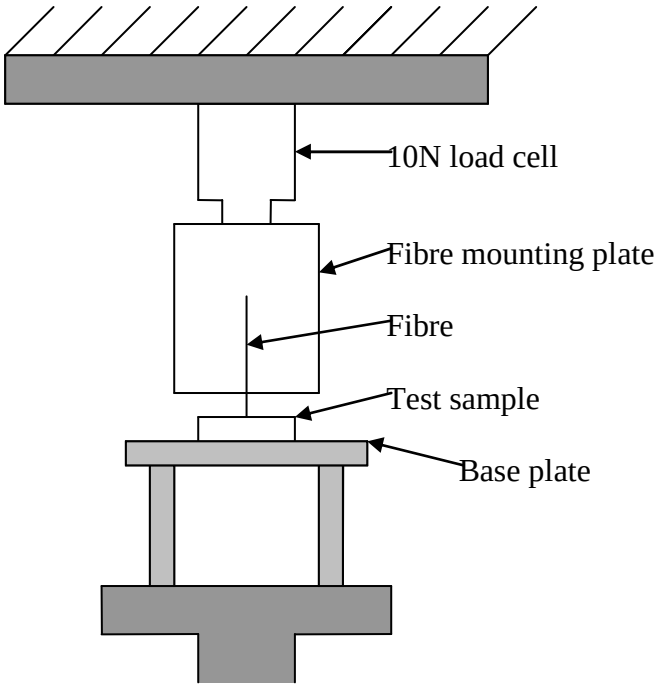

Figure 3.26 Graphical representation of the single fibre pull-out test setup.

3.3.2 Experimental test program

For the preparation of the test sample for the single fibre pull-out tests the same mix proportions and mixing procedure were followed as described in Section 3.1 except that no fibres were used in the mix. Instead, long strands of PVA fibres were used as shown in Figure 3.23.

The casting procedure was as follows:

1. The long strands of fibres were fixed to the fibre frame of the mould.
2. The mould was filled half way and then vibrated for about 1 minute.
3. The fibre frame with the fibres already in position was placed on the mould and the sides of the mould were closed to the top edge of the mould.
4. The mould was carefully filled to the top with the mortar and vibrated for another minute.

Directly after casing, the mould was sealed with a plastic wrapping and stored at room temperature for 2 days. The specimens were then stripped and water cured until testing.

At an age of 14 days the test samples were cut from the specimens. This was done using a small cutting blade normally used to prepare specimens to be analysed with SEM (Scanning Electron Microscope). The specimens were tested shortly after the cutting.

The test program for single fibre pull-out consisted of three parts. Firstly, embedment length tests were done to assist in choosing an embedment length for the single fibre pull-out rate tests. These tests were also used to investigate the effect of the embedment length on the interface parameters. A standard pull-out rate of 1 mm/min was used. The test program is summarised in Table 3.6.

Table 3.6 Single fibre embedment length pull-out tests.

	Embedment length tests			
Number of specimens	5	5	5	5
Embedment length [mm]	1.0 to 1.5	1.5 to 2	4	6
Loading rate [mm/s]	1	1	1	1

Secondly, rate tests were done to investigate the rate dependence of fibre pull-out. The pull-out rate was varied over four orders of magnitude from 0.01 mm/min to 100 mm/min. The test program is shown in Table 3.7. The desired embedment length was chosen from the results of the embedment length tests. This will be discussed in the following section.

Table 3.7 Single fibre pull-out rate tests.

	Pull-out rate tests				
Number of specimens	5	4	6	7	4
Embedment length [mm]	Average = 1.39; COV = 16 %				
Loading rate [mm/s]	0.01	0.1	1	10	100

Creep tests on embedded fibres, i.e. a constant pull-out force applied over time, were the third part of the single fibre tests and will be reported and discussed in Chapter 4.

SEM pictures were also taken of the test samples and the tested fibres to gain insight on the type of damage of the fibres and if the loading rate had an effect on the damage distribution. The following were examined with the SEM:

- The end of some of the pulled out fibres to confirm whether the fibres were completely pulled out or if fibre rupture occurred.
- The fibres at different pull-out rates as well as an unused fibre as a reference to investigate the effect of the pull-out rate on the damage on the fibre surface.
- The inside of the test sample to find out if fibres do debond and slip before they rupture.
- The inside of the test sample to examine the matrix interface after the fibre has pulled out.

To view the inside of the test samples, the samples were carefully broken open to expose the fibre-matrix interface. This is a difficult process and numerous samples were broken before one was broken that successfully exposed the interface.

3.3.3 Results

Different embedment lengths cause large variations of the pull-out displacements and forces and the results had to be normalised for comparison. For this, the force was expressed as a shear stress and the displacement of the pull-out tests were normalised.

The model of a uniformly distributed shear resistance along the embedment length of the fibre is assumed as described in Chapter 2. All the force readings are

expressed as an interfacial shear resistance by dividing it by the surface area of the embedded fibre that is in contact with the matrix using:

$$\tau = \frac{P}{L_e \pi d} \qquad (3.5)$$

with P the applied force, d the fibre diameter and L_e the original embedment length.

The displacement is normalised by the L_e to give a displacement of 1.0 when complete pull-out is achieved. The calculation of the normalised displacement, Δ_n, was done using:

$$\Delta_n = \frac{\Delta}{L_e} \qquad (3.6)$$

with Δ the measured displacement during the pull-out test.

The slip-hardening/slip-softening coefficient, β, is calculated as in Chapter 2 with a positive β representing slip-hardening and a negative β slip-softening. β is found by doing an individual curve fitting exercise with every result using Equation 2.1, to find the most appropriate β.

A typical result is shown in Figure 3.27 with the method of approximation of τ_0 and β represented graphically. The axes are the normalised force expressed as a stress, τ and the normalised pull-out displacement, Δ_n.

The results of the embedment fibre length tests are shown in Figure 3.28. The force and the displacements are normalised as described above. The range of the axes is the same for all the graphs to ease the comparison.

As can be seen from the results, not all fibres were pulled out completely as many of them fractured during pull-out. The difference can easily be distinguished from the results, as a fibre that ruptured shows a sudden drop of force while the response of a fibre that pulled out completely would show a steady load reduction until a zero load resistance at or just before the normalised pull-out displacement, Δ_n, reaches 1. To confirm this, SEM pictures were taken of the fibre ends that were

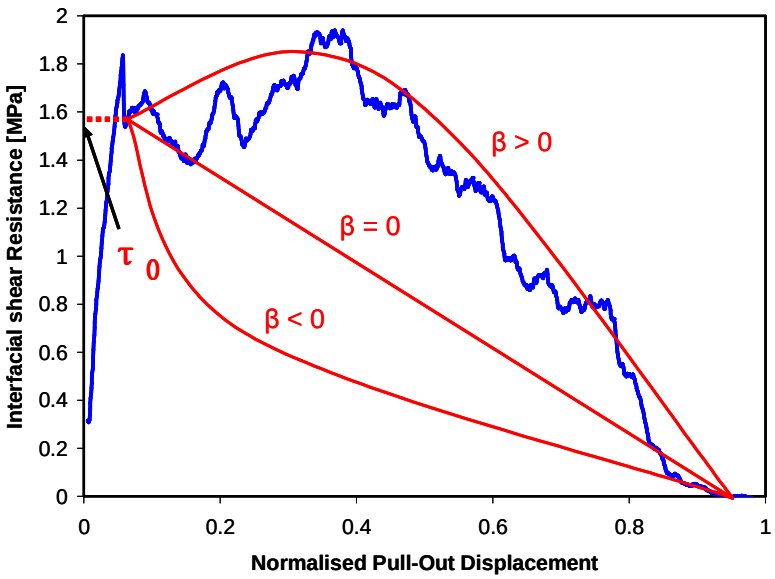

Figure 3.27 A typical fibre pull-out results showing the definition of τ_0 and β.

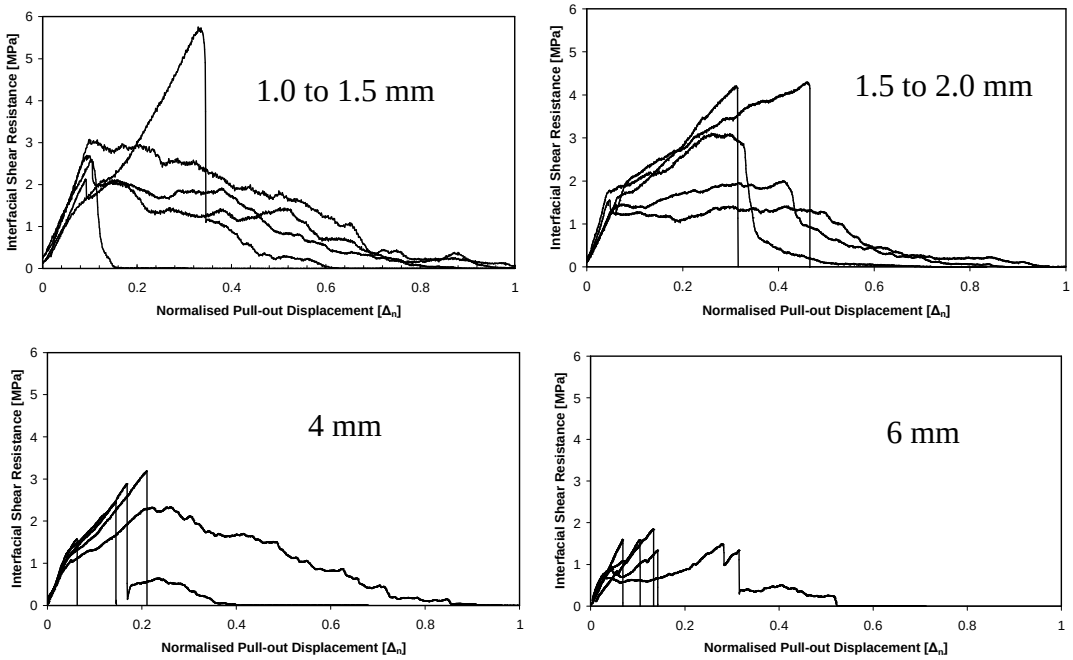

Figure 3.28 The results of the embedment length fibre pull-out tests.

embedded in the matrix. In Figure 3.29 a) an example is shown of a ruptured fibre end, and in Figure 3.29 b) an example of a fibre that pulled out completely. From the SEM pictures it is clear to distinguish which fibre ruptured and which fibre pulled out completely. The end of the latter fibre shows signs of a mechanical cut edge, which occurred during the preparation of the testing sample as described in the previous section.

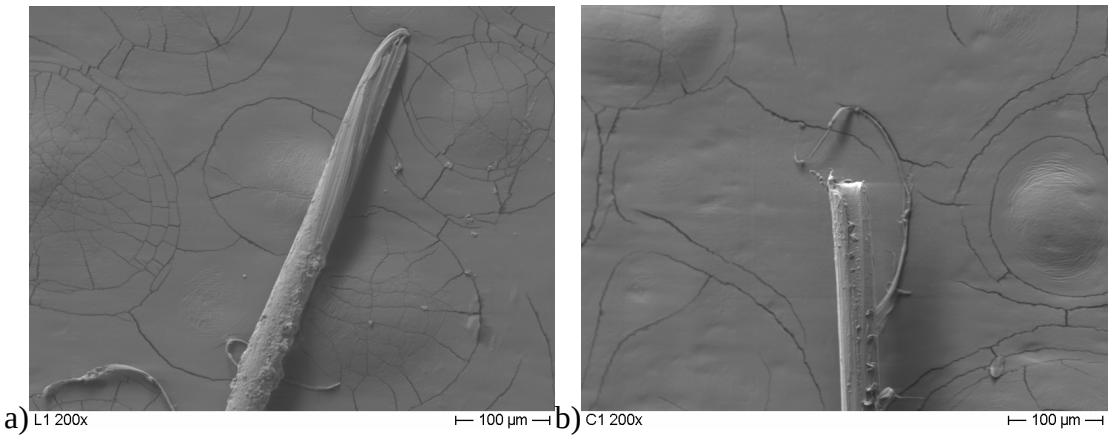

Figure 3.29 a) A SEM picture of a ruptured fibre. b) A SEM picture of a completely pulled out fibre.

To show that the probability of fibre rupture is dependant on the embedment length, the amount of fibres that ruptured during testing is expressed as a percentage of the number of fibres tested in the set of a specific embedment length. The results are shown in Figure 3.30 a) where the percentages are expressed against the embedment length. A clear dependency of the probability of fibre rupture on the embedment length can be seen, with a higher probability with an increasing embedment length.

The initial interfacial shear resistance, $\tau_{0,}$ was found and is shown in Figure 3.30 b) versus the embedment length.

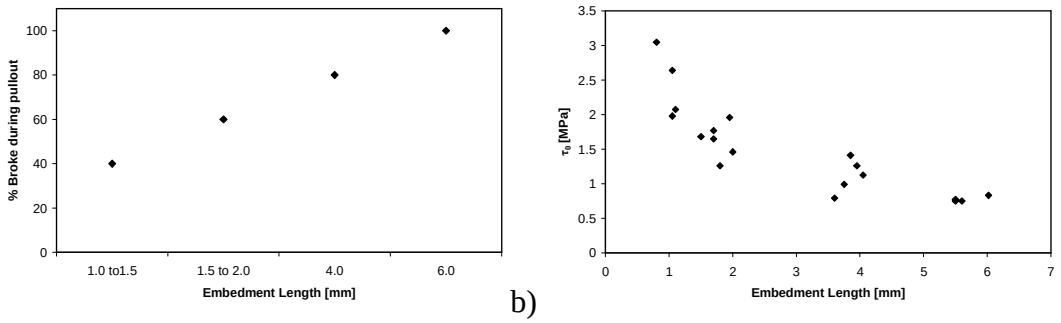

Figure 3.30 a) The percentage of fibres that ruptured during testing versus the embedment length. b) τ_0 versus the embedment length.

The chemical bond, G_d, was defined in Equation 2.2 as a function of the unstable load drop that occurs during debonding. As shown in Figure 3.28, an unstable load drop after debonding was not a regular phenomenon. The G_d will thus be calculated as zero for almost all the tests. This shows that the chemical bond did not play a prominent role in these specific fibre and matrix combination and will for that reason not be derived and discussed.

The primary purpose of these embedment length tests was to establish a suitable embedment length for the single fibre pull-out rate test. For the pull-out tests, the best scenario is when a fibre is pulled out completely as the τ_0 and the β parameters can then be easily identified. As seen in Figure 3.30 a), the shorter the embedment length, the less the chance of fibre rupture, thus the shorter the embedment length, the more suitable the results. An embedment length of less than 1 mm is impractical due to the small size of the test sample for preparation and gluing in the test setup. For these reasons an embedment length in the region of 1.4 mm was chosen for the rate tests.

The results of the rate tests are shown in Figure 3.31 ranging from a pull-out displacement rate of 0.01 mm/min to 100 mm/min. All the axes of the graphs are the same to assist with the comparison. The probability of fibres rupturing during the

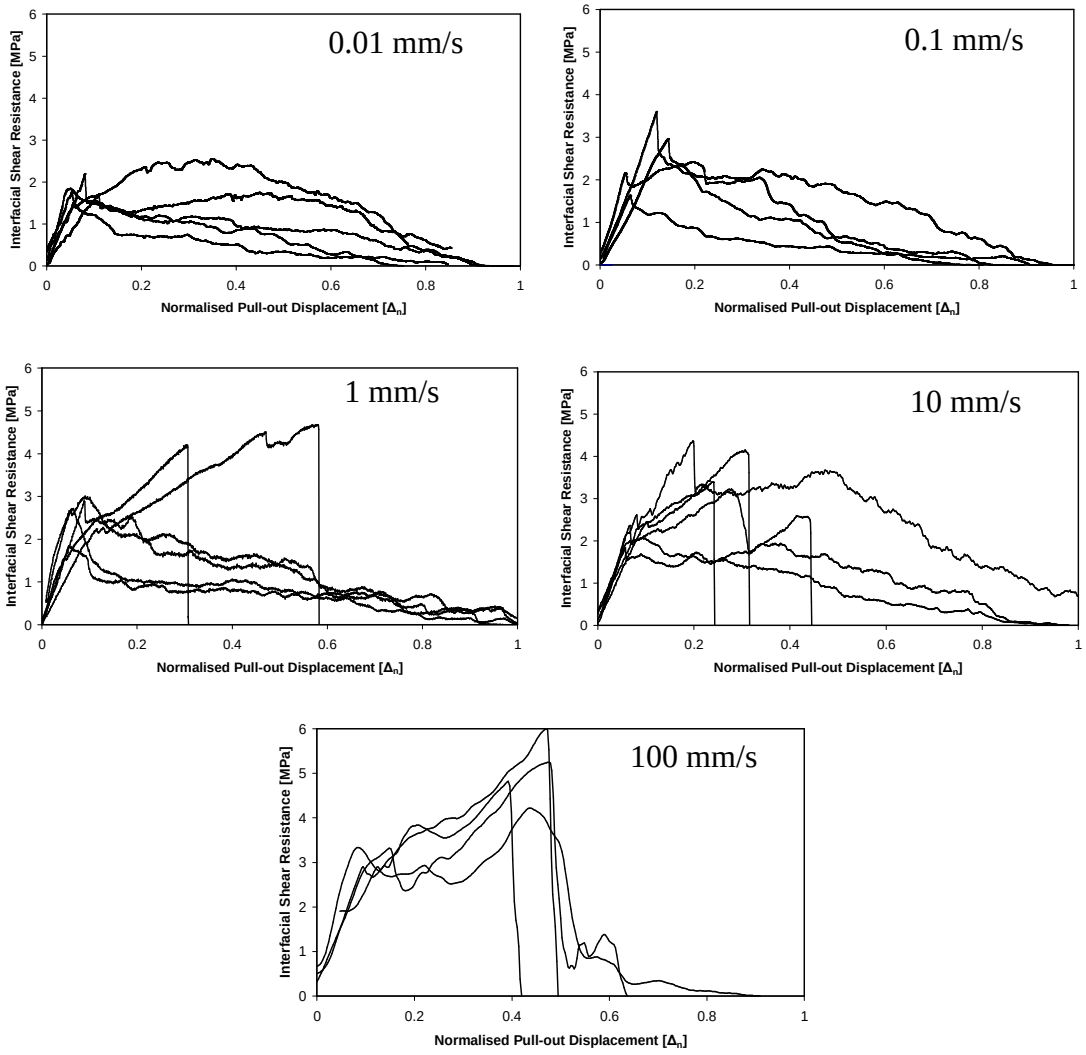

Figure 3.31 Results of the single fibre pull-out rate tests.

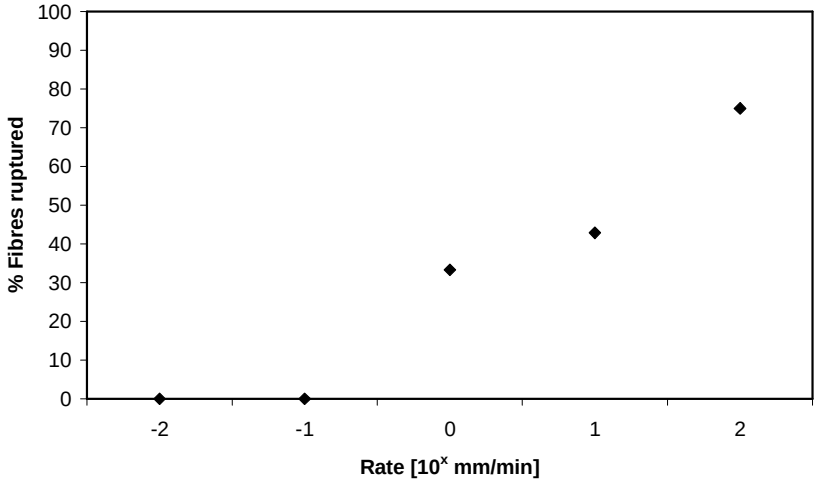

Figure 3.32 Percentage of fibres that ruptured during the rate tests expressed against the testing pull-out rate.

different rate tests is expressed in Figure 3.32 as a percentage of the number of fibres tested for each rate.

The results of the rate tests were analyzed and the trends of the τ_0, β and τ_{max} were found. The definition of τ_{max} is the highest normalised force resisted by the fibre during the test. This value is expressed as an interfacial shear stress over the original embedment interfacial area. The values of τ_{max} include results of tests where the fibres ruptured and pulled out completely. The trends for these parameters are shown in Figure 3.33.

To investigate the damage of the fibres after testing and the effect of loading rate on the damage, a number of SEM pictures were taken of the fibres and fibre matrix interface.

Firstly, test samples were broken open at the interface to expose the fibre embedded in the matrix. Figure 3.34 a) shows a photo of a fibre that was partially pulled out, but due to the fibre rupturing, a part of the fibre stayed behind in the matrix. The damage lines can be seen clearly on the fibre. Figure 3.34 b) shows a test sample that was not tested and the fibre was still embedded in its original position. There are no visible damage lines on the fibre as on the fibre of Figure 3.34 a).

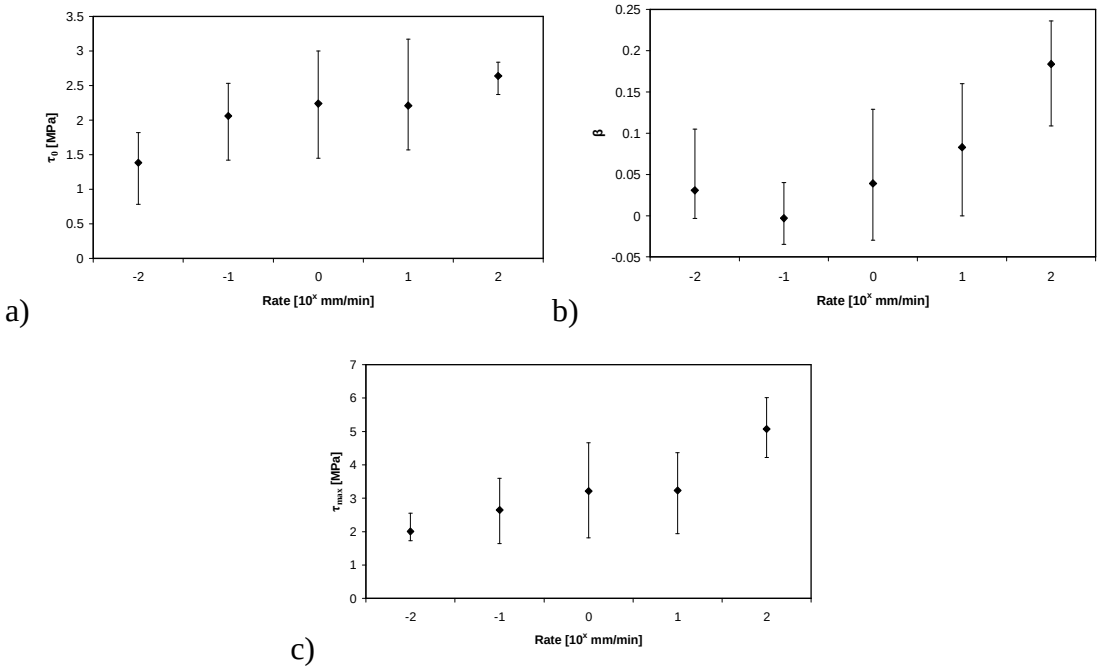

Figure 3.33 The range and average values for different pull-out rates with regard to a) initial interfacial shear resistance, τ_0, b) the slip-hardening/softening relation β and c) the maximum interfacial shear resistance, τ_{max}, expressed as a shear resistance over the original embedment interfacial area.

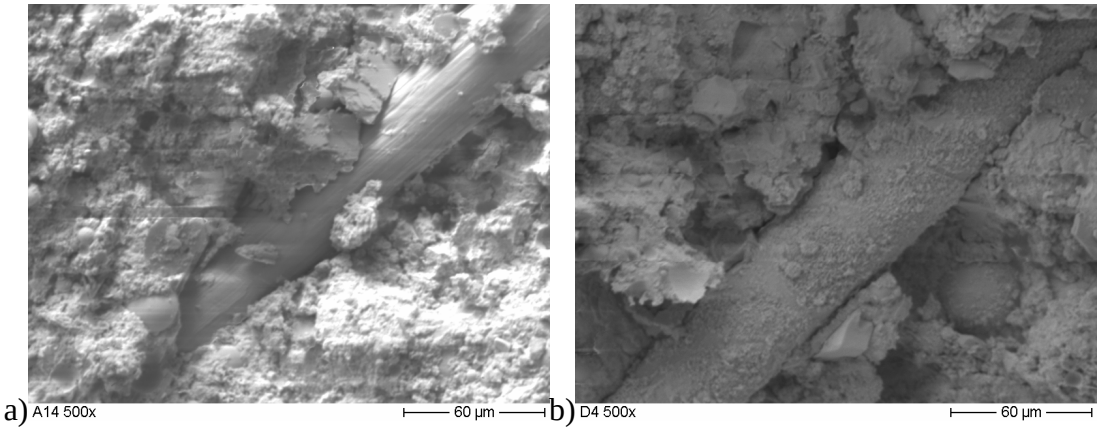

Figure 3.34 a) A test sample of which part of the ruptured fibre remained in the matrix after testing. b) A sample that was not tested.

To see if the pull-out rate has an influence on the surface damage of the fibres, SEM pictures were taken of the pulled out fibres after testing. One SEM picture was selected for each pull-out rate. The photos are shown in Figure 3.35 together with a reference fibre that was still unused.

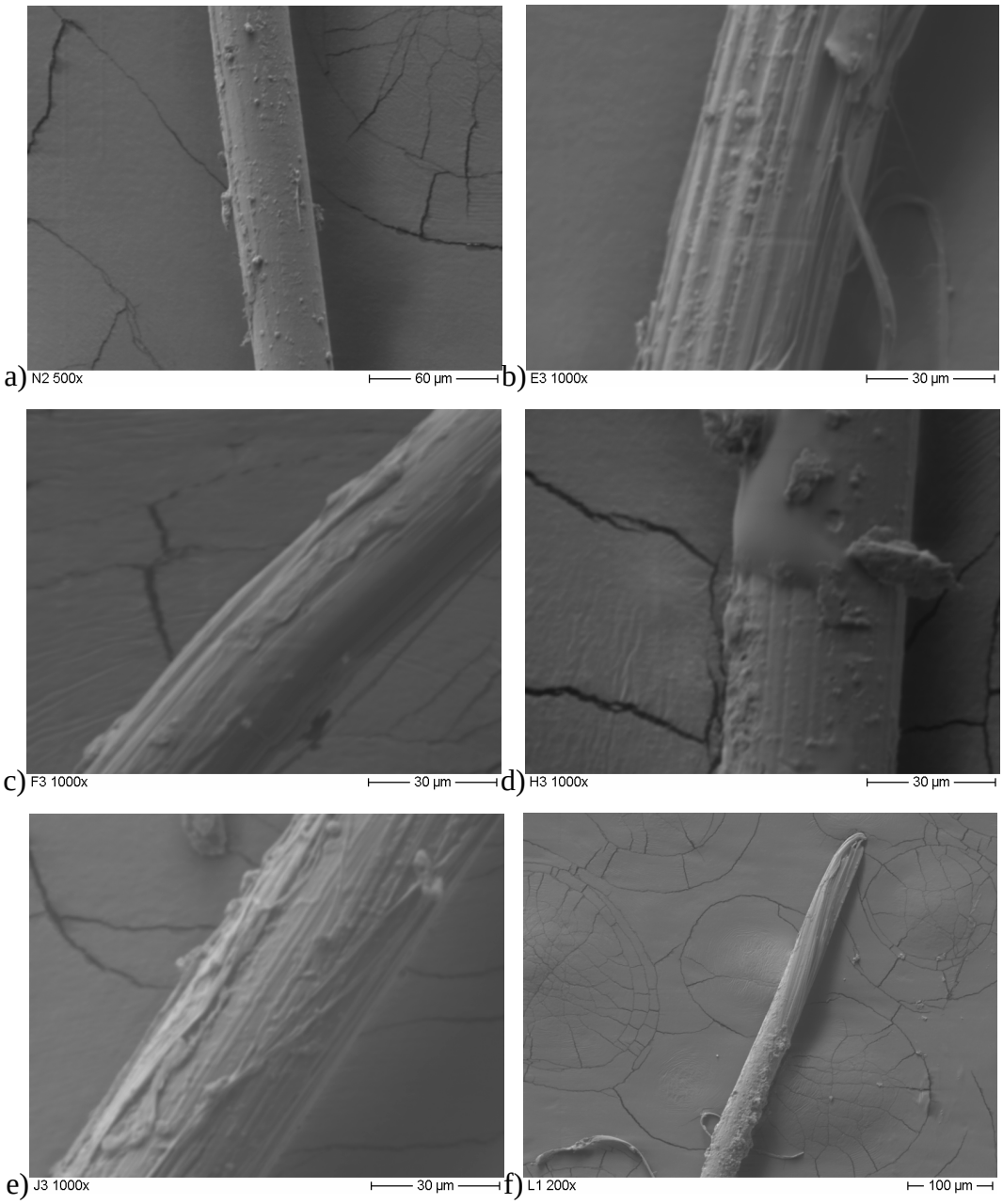

Figure 3.35 a) SEM picture of an unused fibre. b) to f) SEM pictures of pull-out fibres with the pull-out rate ranging van 0.01 mm/min, b), to 100 mm/min, f).

To further investigate the possible cause of the slip-hardening effect, the pulled out fibres were closely inspected to see if strips of fibre were scratched off the surface of the fibre that would cause the damage lines. These strips would get stuck between the fibre and the matrix and would increase the confining pressure and thus increase the frictional resistance. Numerous fibres were found that had loose strands that were still lightly attached to the fibres. This can be seen in Figure 3.36. There were also pieces of fibre found left behind in the matrix after complete pull-out as shown in Figure 3.37. This clearly shows that fibre remains that were scratched off the surface

during pull-out are a cause of the slip-hardening effect of these pull-out tests, but there is no proof that this is the only cause of slip-hardening.

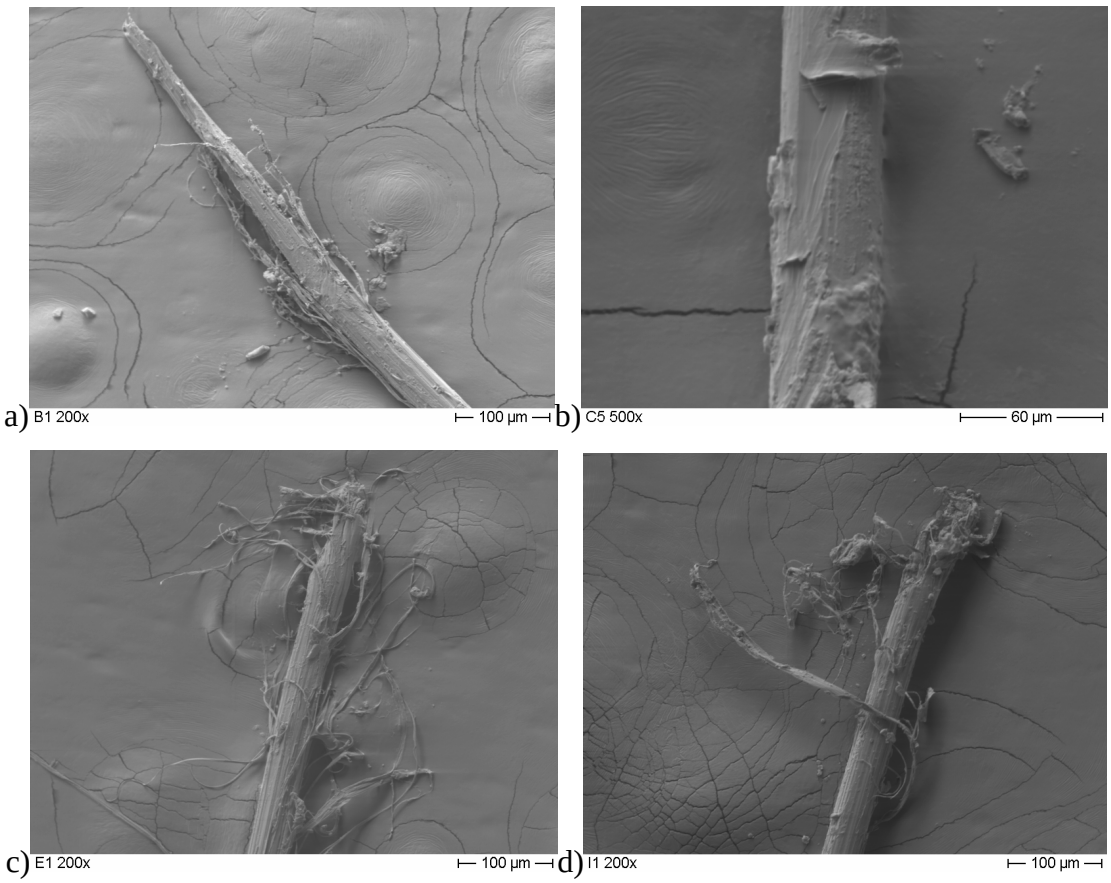

Figure 3.36 Surface damage to a pulled out fibre.

To prove the phenomenon that fibre rupture can occur even after full fibre debonding and some slippage has taken place, a SEM picture was taken of the inside of a test sample of which the fibre ruptured during pull-out. This phenomenon would be proved if the remaining part of the fibre in the matrix did undergo some slippage, i.e. the end part of the fibre is not in its original position. The SEM pictures in Figure 3.38 clearly show this. The remaining part of the fibre has slipped and the end of the embedded side is shown to be the cut end of the fibre and the other end of the fibre still embedded in the sample was clearly ruptured.

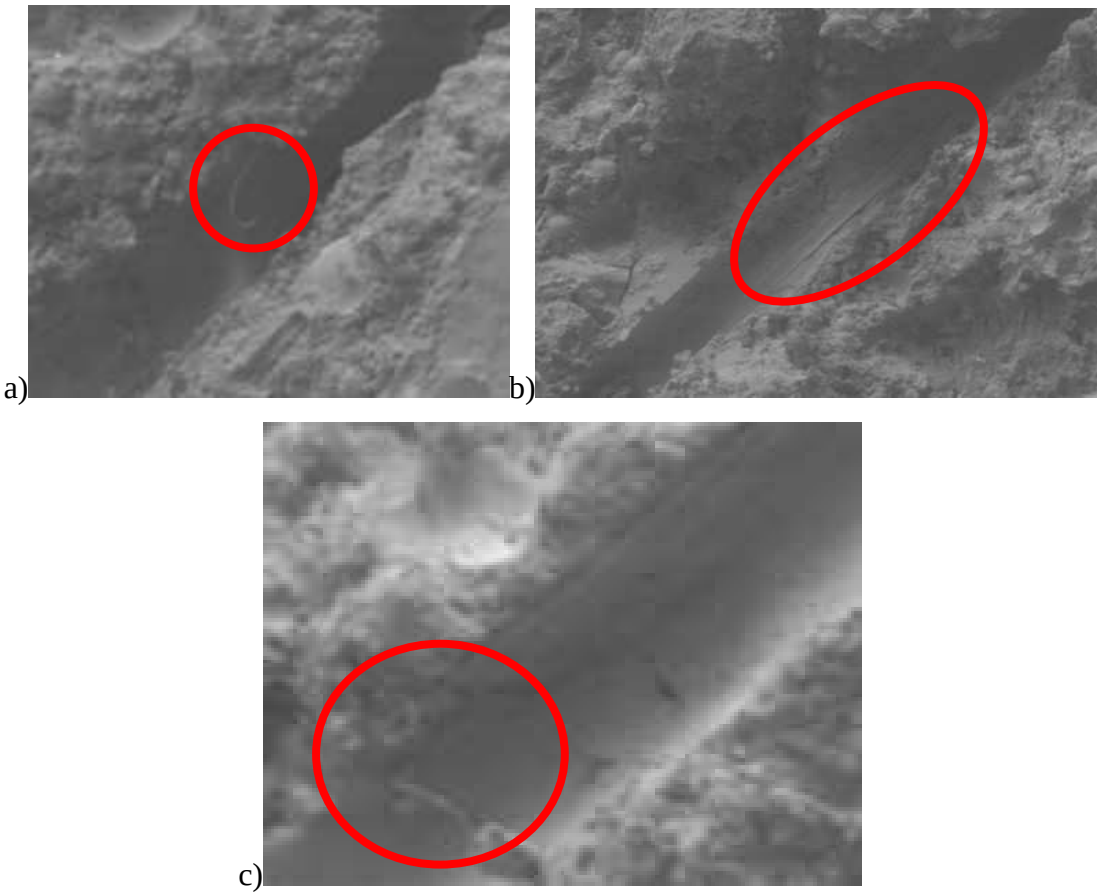

Figure 3.37 Signs of remains of fibre in test sample after pull-out.

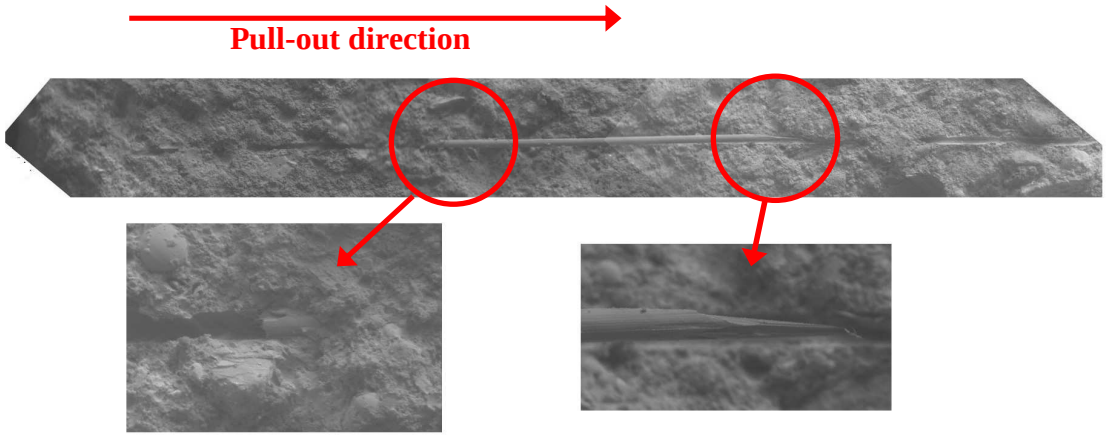

Figure 3.38 SEM picture showing the two ends of a fractured fibre that remained in the test sample.

3.3.4 Discussion

Firstly, the phenomenon of apparent strength of the fibres described earlier in Section 3.3, would cause the fibres to fracture at a much lower stress than the ultimate fibre strength if they are embedded in the matrix. In Figure 3.39 the maximum fibre stresses are shown for the fibres that ruptured during embedment length tests. These stresses are calculated by dividing the force by the cross sectional area of the fibre. It is important to note that the values for the embedment length between 1 mm and 2 mm are statistically incorrect as they only represent the fibres that ruptured. Fibres that had a higher ultimate resistance due to statistical distribution will not reflect on the graph as they did not rupture, but they pulled out completely. For this reason the rupture stresses of the fibres that were embedded in this range were neglected for the calculation of the average fibre rupture strength.

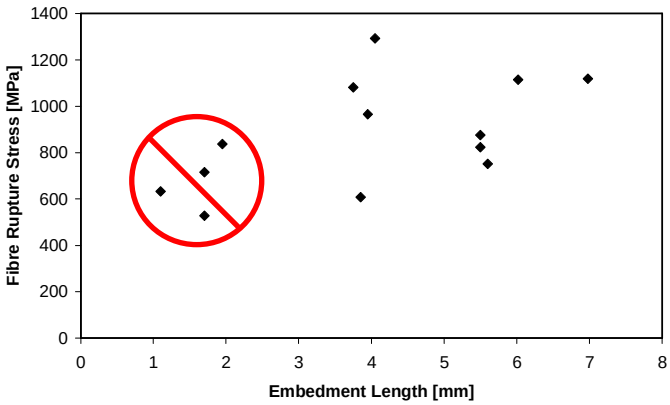

Figure 3.39 The maximum fibre stress for the fibres that ruptured during the embedment length tests with the disregarded results clearly shown.

The average fibre rupture strength was calculated to be 959 MPa with a COV of 22.4 %. A large COV was to be expected due to the large variation of the type of damage to the fibres that is believed to cause this premature rupture. The apparent strength of the fibres found is 61 % of the indicated strength (1560 MPa) of the fibres supplied by Kururay. This corresponds well with the results of Redon et al (2001) that found the apparent strength to be 60 % for the same type and almost the same diameter fibre (44 μm compared to 40 μm used in this study).

The embedment length tests showed a strong trend that the longer the embedment length, the higher the likelihood of the fibre fracturing during a pull-out test. This phenomenon comes as no surprise, as Redon et al 2001, Lin et al 1999,

Kanda and Li 1998, Yang and Li 2005 and Li et al 2002 all prescribed an embedment length less than 1.2 mm for successful pull-out of a fibre. This value could however vary as the matrix-fibre interface varies with different matrix compositions. A theoretical critical embedment length, $L_{critical}$ can be found by balancing the resistance of a fibre due to a uniformly distributed interfacial shear resistance, τ, and the strength of a single fibre, as follows:

$$\sigma_{ultimate\,of\ \ fibre}\,\pi\frac{d^2}{4} = \tau\pi d\,L_{critical} \qquad (3.7)$$

Using a value of 1560 MPa for the ultimate strength of the fibre, $\sigma_{ultimate\ of\ fibre}$, a diameter, d, of 40 μm, and a $L_{critical}$ of 3.9 mm an extreme value of τ = 4 MPa is found. If the apparent strength phenomenon is taken into account, the $L_{critical}$ is found to be 2.4 mm. These values do not correlate with the experimental findings due to the negligence of the slip-hardening effect.

An important phenomenon that was completely unexpected was the reduction of the τ_0 with the longer embedment length (Figure 3.30 b)). All the micro-mechanical models shown in Chapter 2 rely on an assumption that the interfacial shear resistance is uniformly distributed along the fibre interface. Figure 3.30 b) shows that this is not the case and the value of τ_0 increases substantially when the embedment length of the test is reduced.

A possible explanation is that the Poisson's ratio of the fibre plays an important role in the distribution of the interfacial shear resistance of the fibre. The interfacial shear resistance would reduce if the axial stress in the fibre increases due to the Poisson's ratio effectively reducing the confining pressure which causes the frictional resistance. This is an important phenomenon that requires further investigation. This effect would not play a role in the analysis of the results of the fibre pull-out rate tests as the embedment lengths of these tests were within a relatively small range.

A trend was seen in the fibre pull-out rate tests that showed that the faster the pull-out speed, the higher the probability of fibre rupture. The probability ranged from 0 % of fibre rupture at the lowest testing rate to 80 % at the highest testing rate. There are not enough test results to show a true statistical probability distribution, but the trend is clear. This is an alarming result as this shows that the fracture mechanism of ECC may change if the loading rate changes.

The value of initial interfacial shear resistance, τ_0, showed an increase of 91 % from the lowest to the fastest pull-out rate. This result contradicts the results of Yang and Li (2005) who found no influence of rate on the value of τ_0. The embedment length used by Yang et al (2005) was 0.5 mm which is less than half the embedment length used in this study. The embedment length plays an important role in the magnitude of τ_0 as shown in Figure 3.30 b), and could also influence the mechanism that causes the time-dependant resistance increase and thus explaining the difference found compared to Yang et al (2005).

The maximum fibre resistance, τ_{max}, showed an even higher increase with an increase of loading rate. It increased by 153 % from the lowest to the highest pull-out rate. This can be explained by the increase of the slip-hardening coefficient, β. β increased from around 0 to 0.18 with the increase of pull-out rate. A higher β would result in an even higher fibre resistance during pull-out, hence the larger increase of τ_{max} compared to increase of τ_0. The increase of β is also a trend that was not found by Yang et al (2005) who found no change of β by increasing the pull-out rate.

Due to the strong increase of τ_0 and β, the ultimate strength of the tensile tests on the dog bone specimens reported in section 3.1.3 should also show a strong increase with a higher loading rate. This is however not the case. A possible explanation is that, due to the increase of τ_0 and β, the probability of fibre rupture increases during tensile testing and would result in a lower ultimate strength than expected, as fewer fibres are available for the load transfer over a crack plane.

On Figure 3.34 and Figure 3.35 it is clear that surface damage occurs during pull-out. The damage is in the form of long, straight scratch marks on the fibres. It can also be seen in Figure 3.36 that as a result of these scratch marks, pieces of fibre are scraped off the fibre surface and the loose strands can be seen still partially fixed to the fibre. In Figure 3.37 it is shown that some of the fibre strands remain in the matrix after pull-out. These fibre strands are believed to be the cause of the slip-hardening effect. The loose strands are lodged between the fibre and the matrix and effectively increase the confining pressure that would in turn increase the frictional resistance. The damage is not always uniformly distributed as can be seen on the photos, thus the large variation of the slip-hardening coefficient, β.

No clear effect could be seen on the surface damage of the fibres that can be related to the pull-out rate from Figure 3.35. It is even more difficult for the higher loading rate, as seen in Figure 3.35 f), as the fibres ruptured during the higher pull-out

rate tests, thus leaving no part of the fibre that can be investigated for surface damage that was originally embedded in the matrix. Also, the damage would differ along the fibre and the damage patterns due to the heterogeneity of the matrix. All this makes the exercise of finding a change of surface damage at different pull-out rates a difficult task if a visual inspection is to be used as a measure.

The increase of resistance of the values of τ_0 and β can be explained if the matrix is assumed to be of a visco-elastic nature, as is the case for any cement-based matrix. With the slower pull-out rates, the matrix has more time to redistribute the pressure and thus effectively reduce the confining pressure on the fibre during the pull-out of the fibre. The frictional resistance is linearly dependant on the confining pressure according to Coulomb's friction law. The redistribution would then reduce τ_0 at lower pull-out rates. The same can be said for the slip-hardening coefficient. Any stress concentrations acting on the fibre due to the lodging of the fibre strand scraped off would be reduced. The value of β would then also be reduced at lower strain rates as has been seen in the results.

3.4 Concluding Summary

Experimental tests were done with the scale ranging from a single fibre pull-out test to tests on a structural-level to investigate the effect of the loading rate on the mechanical behaviour of ECC.

On the single fibre level, embedded fibres were pulled out using a range of pull-out rates. A strong increase of the fibre pull-out resistance was found with an increase of the pull-out rate. The probability of fibre rupture during pull-out significantly increased with an increase of the pull-out rate. Another significant finding unrelated to the time-dependant behaviour is that the interfacial shear stress is not uniformly distributed along the embedded surface of the fibre. This conclusion can be drawn as $\tau_{0,}$ which is calculated assuming a uniformly distributed shear stress, was found to be strongly dependant on the original embedment length.

On the macro-level, the strain rate of direct tensile tests was varied to investigate the effect of the loading rate on the tensile material properties. A strong increase was found on the first cracking strength with an increase of strain rate, which is typical of a cement-based material. For the ultimate tensile stress however, only a

slight increase was found with an increasing loading rate. This is in contrast with the single fibre tests which showed a strong increase of the fibre pull-out resistance. The increase on the single fibre level is not reflected on the macro-level due to the failure mechanism shifting towards fibre rupture instead of fibre pull-out with an increase of loading rate.

For the structural-level, rate-dependant tests were done using three point bending tests. The deflection rate was varied by almost 4 orders of magnitude. The same trends for the first cracking and ultimate strengths were found as for the tensile tests. The ultimate deflection, which is an indication of the ductility, however, showed a decrease with increase of deflection rate compared to the tensile ductility which remained constant over the loading rates. This is explained by the rate dependence of the first cracking stress which dictates the size of the region of multiple cracking which is related to the ductility of the flexural response.

Creep tests are required for the further investigation of the time-dependant response if the material is exposed to a sustained load.

CHAPTER 4

Experimental Creep and Shrinkage of ECC

The ductile tensile behaviour is what sets ECC apart from ordinary concrete. The compressive behaviour is also more ductile compared to ordinary concrete, but the real benefit is attained when ECC is used to resist a force or displacement load in flexure. ECC, as shown earlier, can undergo up to 5 % strain in tension while retaining tensile stress capacity. An important question is however if the material can sustain the load over a period of time without considerable creep which can cause premature, unexpected failure or cause serious serviceability problems.

It is unthinkable to execute a creep test for every type of ECC application before it is utilised commercially. A simplified method is required to aid the designer when designing the long term behaviour of a structure or structural element consisting in part or fully of ECC. As a first step in creating a simplified model, the creep behaviour has to be thoroughly investigated and the mechanisms responsible for the time-dependant strain increase, understood. For this, creep tests were performed on different size scales, i.e. on a macro-level and meso level, for one specific ECC mix.

For the macro-level, uniaxial tensile creep and shrinkage tests were performed. As a further investigation into the creep behaviour, tensile creep tests were done on specimens that were pre-cracked, therefore referred to as cracked section creep tests. These tests were done to investigate the effect that cracking has on the creep behaviour. Lastly, single fibre creep tests were performed together with embedded fibres that were pulled out of the matrix at a constant force to see the effect of creep on the fibre-matrix interface characteristics.

4.1 Shrinkage and Tensile Creep Tests

Doing creep tests in tension presents considerable difficulty and Neville (1970) admitted that even for short term tests, applying a uni-axial tensile load to concrete proves to be an intricate task. The applied load needs to be about an order lower than in compression due to the low resistance of concrete in tension. This has the result that the shrinkage strains occurring during testing may be larger than the actual creep strain, thus very accurate methods need to be used to measure the displacement. Sealing a specimen to prevent any moisture migration to and from the specimen, which is required to attain the basic creep, is not an easy task over a long period of time (Wittman and Roelfstra 1980).

Nevertheless, it is inevitable that uni-axial creep tests are required for the characterisation of the time-dependant behaviour of ECC.

4.1.1 Experimental test setup

To be consistent with all the experimental tests, specimens with the same shape and dimensions were used as in Chapter 3. As these tests were planned to be executed over a period of more than 6 months, a test setup had to be designed where numerous of these specimens could be placed under different sustained loads for a long period of time.

The creep test setup was designed and built to apply the load with free hanging weights acting on the specimens with a lever arm. The load is applied to two specimens in series. Due to the action of the specific lever arm arrangement chosen, the load of the weights is increased by a factor of 4. The setup can be seen in Figure 4.1.

The shrinkage tests were done with the same type of specimens. The specimens were placed on two frictionless rollers on a table. The strain was measured in the same way as for the creep tests. The setup is shown in Figure 4.2 b).

The environment in the room where the tests were performed was controlled to be at a constant temperature of 23±1 ˚C and a relative humidity of 65±5 %.

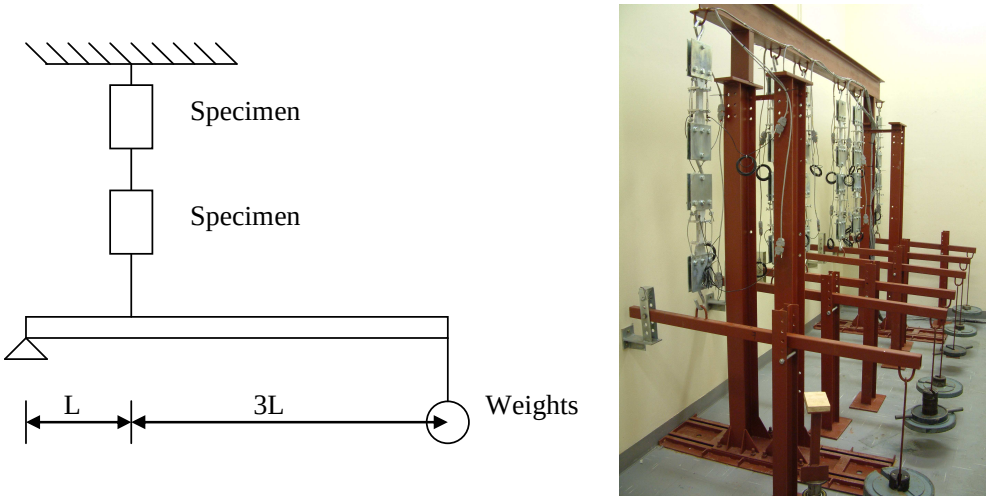

Figure 4.1 The tensile creep setup using a method of lever arm to apply the load.

a) b)

Figure 4.2 a) The load application clamps as well as the strain measuring device. b) The shrinkage test setup.

The clamps used to grip the specimen and the strain measuring setup is the same as those in Chapter 3. A photo is shown in Figure 4.2 a).

4.1.2 Experimental test program

Two sets of tests were done for the tensile creep tests. One set was unsealed and allowed to dry, and the other was sealed with the brush applied sealant. The effectiveness of the sealant and the effect this has on the results will be discussed in the next two sections.

An appropriate tensile load was chosen to be 50 % of the average ultimate resistance. The specimen at the top of the setup had a slightly higher applied load due to own weight of the specimen and clamps below it. In the analyses of the results, a compensation was made to incorporate this increased load.

The loading of 50 % of the ultimate was chosen for a few reasons. Firstly, to ensure that no cracking of the matrix occurs during the duration of the test, the load had to be well below the cracking stress of the matrix. When the matrix cracks, the properties of the material changes as the load is then transferred by the fibres in the cracked section. The effect of fibre creep and the time-dependant pull-out of fibres then also play a role and this will be investigated in Sections 4.2 and 4.3. The cracking stress was found to be between 70 % and 80 % of the ultimate load. However, unexpected cracking did occur during the creep tests and will be discussed in the following sections.

Secondly, the load had to be chosen as low as possible to insure that the creep compliance is still proportional to the applied stress, but the effect of creep had to be significant enough to be measured accurately. It was decided that a load of 50 % would be adequate to achieve these goals.

For the shrinkage test, four specimens were tested. Two of the specimens were left unsealed and the other two sealed as in the case of the creep tests.

A summary of the test program for the creep and shrinkage tests is shown in Table 4.1.

Table 4.1 The test program for the creep and shrinkage tests.

	Unrestrained		Loaded at 50 % of ultimate load	
	Sealed	Unsealed	Sealed	Unsealed
Number of specimens	2	2	2	2

Two specimens were used for each type of test. The ultimate load was chosen as 2.79 MPa which is the average ultimate load for the direct tensile tests at a normal or standard testing speed, i.e. a strain rate of 104 μ/s in this case which causes failure between 2 and 5 minutes. The applied load cannot be objectively referred to as half the tensile capacity, as the tensile capacity, especially the first cracking strength, varies according to the loading rate. The creep load is applied over a time of about 1

second, which leads to a loading rate of approximately 146 μ/s if the E-modulus is taken as 9.2 GPa, which is the same as the normal testing strain rate.

The mix, mixing procedure and method of curing were exactly the same as for the tensile tests described in Chapter 3, save for the specimens that were not sealed. These specimens were left in the water until an age of 14 days before taken out to test and were kept moist with a light paint brush until the test started. The period between the removal of the specimens from the water and the start of the test was not more than 30 min.

4.1.3 Results

The readings taken from the strain measuring devices were transformed to give a reading of strain in percentage. The readings were taken over a gauge length of 88 mm. The results of the shrinkage tests are shown in Figure 4.3. The time is expressed in days with the zero point at the time of the commencing of the tests, i.e. at a specimen age of 14 days.

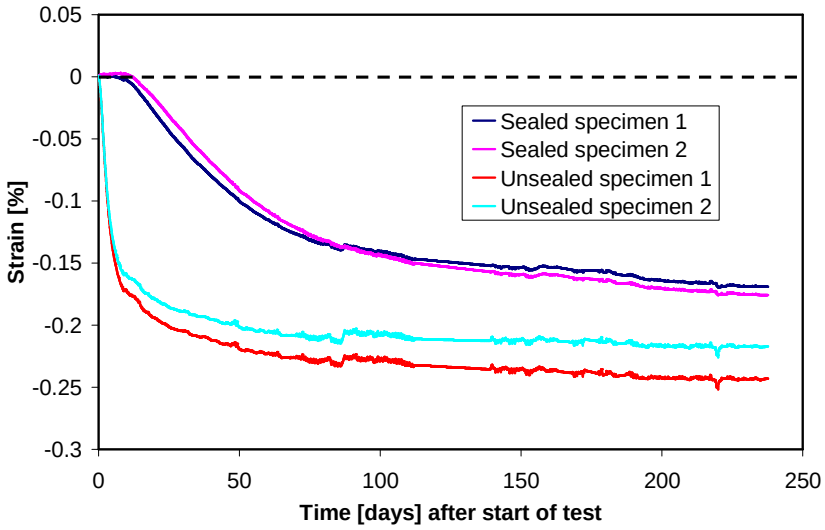

Figure 4.3 The shrinkage results for a period of 240 days, i.e. 8 months.

The response of the unsealed specimens is a typical response for a cement-based material. At the initial stage a large amount of shrinkage can be seen and the shrinkage rate reduces as time goes by. The shrinkage strain apparently stabilizes at an average strain of 0.23 % after about 200 days of drying.

The response of the sealed specimen is somewhat unexpected. The material showed no shrinkage but rather a small amount of swelling in the first 8 days of testing, after which shrinkage started. After about 50 days, the rate decreases but the shrinkage continues. At a time of 240 days, the time the tests were ended, the shrinkage has almost stabilized, but an increasing trend remains.

To investigate this strange phenomenon of the sealed specimens, the humidity was increased from 65 % to 85 % in the climate room after the tests were ended after a period of 8 months. If moisture movement was completely prevented to and from the specimen in the sealed tests, the increase of humidity should have no effect on the strain readings. The responses of the specimens after the increase of humidity are shown in Figure 4.4 and a clear effect on the strain due to the increase of humidity can be seen for both the sealed and the unsealed specimens.

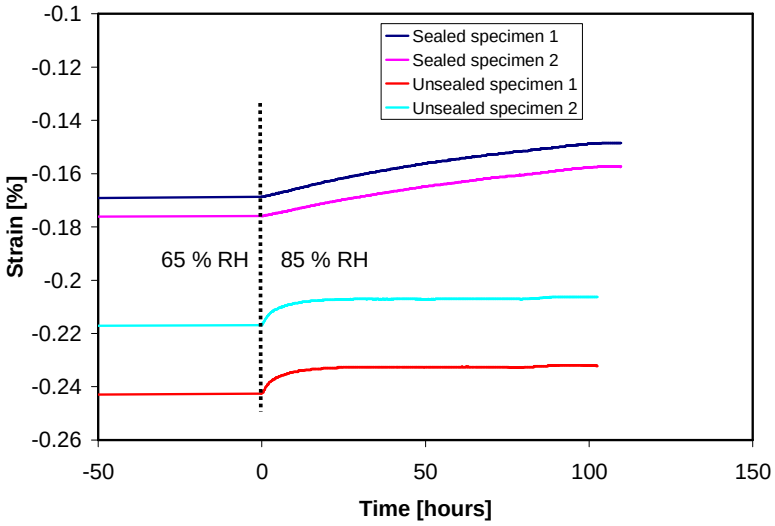

Figure 4.4 The effect of an increase of humidity on the shrinkage specimens after they were allowed to dry for 8 months.

A clear difference can however be seen between the sealed and shrinkage specimens. The unsealed specimens showed a sudden increase of strain, i.e. a swelling. The swelling stabilized within 24 hours. The sealed specimens also showed swelling, but at a much lower rate.

Without full explanation of the swelling trends, it is clear that the sealed specimens are sensitive to a change in the external humidity. Therefore, the conclusion can be drawn that the sealed specimens were not sealed completely, or in other words, the sealant was permeable. Due to this permeability, the painted

specimens will be referred to as the "sealed" specimens for the rest of this dissertation. The significance of the results of the "sealed" tests will be discussed in the next section.

The creep responses of the loaded specimens are shown in Figure 4.5. It is clear that even though the specimens were loaded in tension at 50 % of the tensile capacity, the shrinkage of the specimens still played a dominant role. The "sealed" specimens showed some deviation in the first 50 days, but after that the strain readings started to converge. The unsealed specimens however showed a clear difference between the two specimens from the start. The reason for this becomes clear if one looks closer at the strain readings of the first day for these specimens.

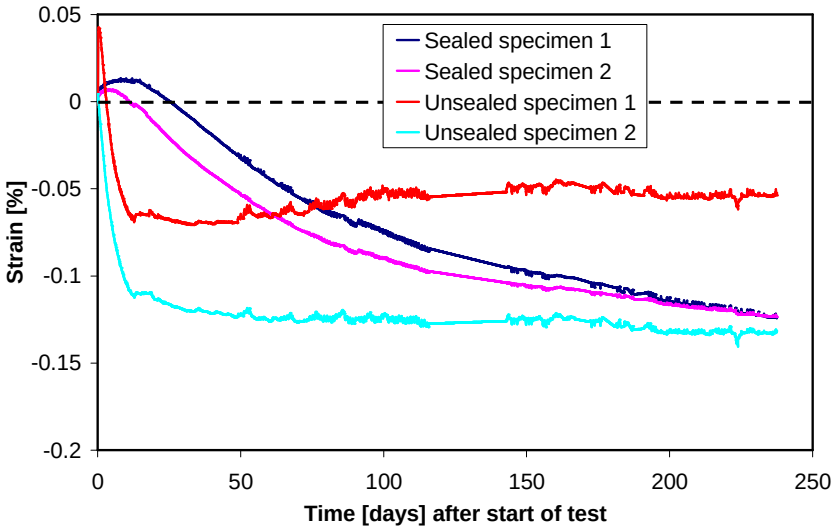

Figure 4.5 The strain readings of the creep specimens.

In Figure 4.6 a) the strain readings of the unsealed creep specimens are shown for the first 25 hours after loading. About 4 hours after the load application, a crack formed in the one specimen. The increase of strain can be seen in Figure 4.6 a) and a photo of the crack is shown in Figure 4.6 b) to prove that it was indeed a crack that formed and not an error in the strain readings. Thus, a large difference in time-dependant deformation is caused by cracking.

a)

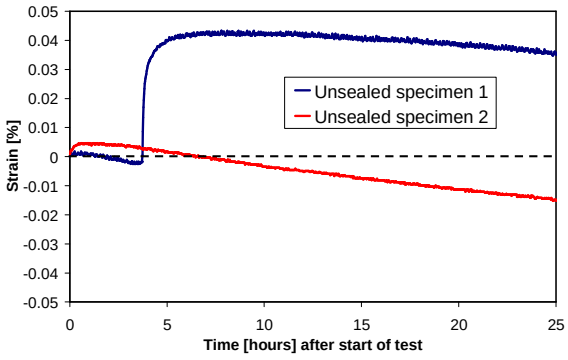

b)

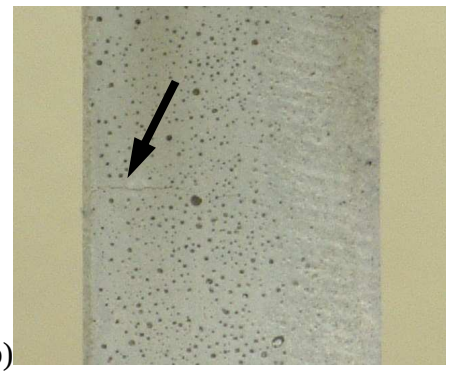

Figure 4.6 a) The strain readings of the unsealed creep specimens for the first day of loading. b) The crack that formed after 4 hours in specimen 1.

To attain the total creep, i.e. creep strains including basic as well as drying creep if applicable, for both the unsealed and "sealed" specimens, the shrinkage strains need to be deducted from the creep strains. As there are only two specimens per test and one specimen for the unsealed creep tests because the one specimen that cracked is discarded in these calculations, the average results are not representative of the true average time-dependant behaviour. The results will however give a good indication of the range of creep values expected. Therefore, the deductions are not done with the average readings of the tests, but rather with the range of readings. All the combinations of the creep and shrinkage results are deducted from each other and then an envelope which contains the maximum and minimum values are drawn. The envelopes of the creep results are shown in Figure 4.7 for the unsealed and "sealed" creep results.

4.1.4 Discussion

Firstly, the permeability of the "sealed" specimens is discussed. It has been shown in the previous section that the "sealed" specimens were still permeable after sealing and thus the specimens experienced some drying shrinkage, but at a lower rate than the unsealed specimens. The responses of the "sealed" shrinkage and creep specimens are in a narrow band and show the same, and in some cases even less deviation compared to the unsealed specimens. This can be seen in Figure 4.3 and Figure 4.5. This is a

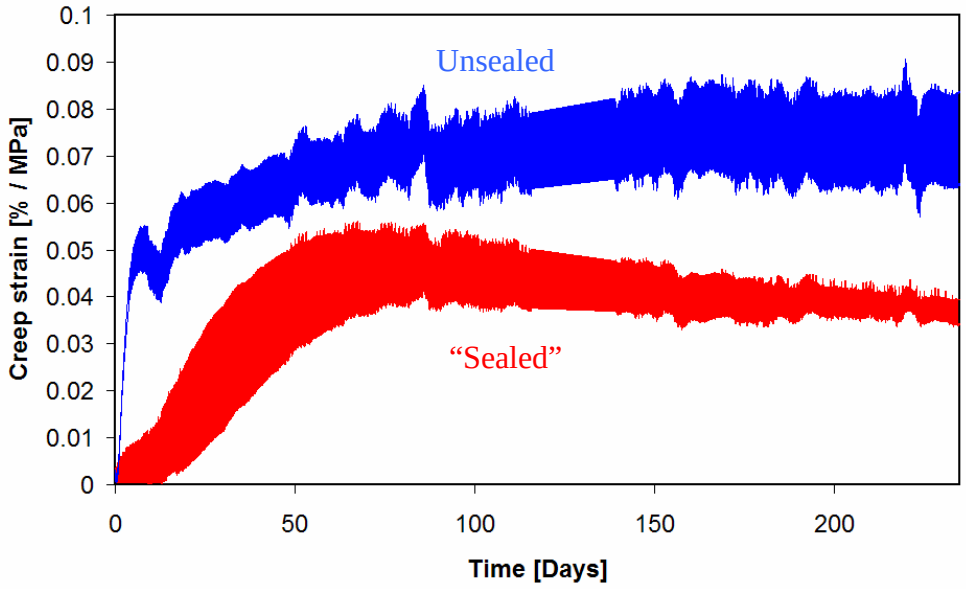

Figure 4.7 Envelopes of the calculated total creep strains for the unsealed and "sealed" creep tests.

good indication that the permeability of the sealing material is uniform and that the moisture migration from the specimen to the environment is not due to inconsistent application of the sealant or weak spots that would allow irregular moisture movement. The rate of moisture movement is thus believed to be the same for all the painted specimens as the same application procedure was used for the painting of all the specimens. The results of the "sealed" shrinkage and "sealed" creep tests can now be analysed and discussed knowing that the difference between the unsealed and "sealed" specimens is the rate of drying. This resulted in the detection of useful trends as the effect of the rate of drying can now be seen on the shrinkage and creep responses. The true basic creep can however not be calculated.

Next, the swelling phenomenon at the start of the shrinkage tests of the "sealed" specimens is discussed. If the sealant that was used had a constant permeability, the "sealed" specimens would start shrinking immediately, but at a lower rate than the unsealed shrinkage specimens. However, the specimens first showed signs of swelling and the strain only became negative (in the direction of shrinkage) after about 7 days of drying as shown in Figure 4.8. A possible explanation for the late shrinkage is that the sealant only became permeable after 7 days. This does not explain the swelling. Also, there was no sudden start of shrinkage after a few days that could support this theory.

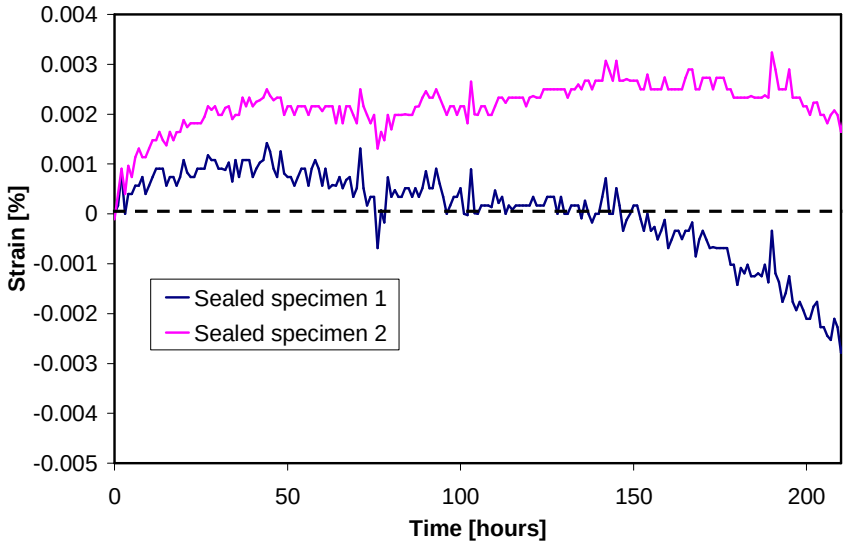

Figure 4.8 The shrinkage of the "sealed" specimens in the first few days of testing.

Kovler (1996) sheds some light on this matter. When doing tensile creep tests on ordinary concrete he found that the sealed specimens showed some swelling. This is unexpected as the mechanism of swelling is normally attributed to the saturation process of the material or the increase of the relative humidity of the environment, but no moisture movement towards the specimen was allowed due to the sealing of the specimens. Swelling of concrete in general is believed to be caused by one or more of the following mechanisms (Kovler 1996):

1. Capillary stress caused by changes in the vapour pressures in the capillary pores.
2. The disjoining pressure.
3. Changes in the surface free energy.
4. The movement of water between the interlayers.

Vapour pressure is an important mechanism in hygral deformation. This was first pointed out by Freyssinet (1951). When water saturated concrete is allowed to dry, the vapour pressure in the capillary pores are not in equilibrium with the environment. To restore the balance, water is evaporated from the capillary pores until the vapour pressure is in equilibrium with the environment. The vapour pressure is then reduced in the capillary pores and results in shrinkage of the pores, and in return, causes shrinkage of the material.

This mechanism can be explained using the Young-Laplace equation for the pressure difference over a liquid film which is:

$$\Delta p = \frac{2\gamma}{r} \qquad (4.1)$$

with γ the surface tension and r the radius of the meniscus and for small capillaries as in the case of concrete, the radius of the capillary pore. Δp is the vapour pressure difference over the liquid surface, i.e. the difference between the vapour pressure of the liquid and the air in the capillary. γ stays constant for water if the temperature does not change, thus if the difference of the vapour pressure increases, the radius of the capillary has to be reduced to satisfy Equation 4.1.

When a specimen is sealed, Kovler (1996) postulates that a sudden increase of vapour pressure may be found in the capillary pores. If the vapour pressure is increased, the pressure difference between the absorbed water and the air in the capillary pores is decreased. To satisfy Equation 4.1, the radius of the capillary pores has to increase. The increase of size of the capillary pores causes an increase of material length on the macroscopic scale causing a swelling phenomenon. The reader is referred to Kovler (1996) for an in depth discussion of this mechanism.

It has now been shown that the increase of strain found after sealing the specimen may be attributed to this swelling phenomenon, but there is no experimental proof of this. For this reason the shrinkage results will not be adjusted to compensate for the swelling and will be analysed and discussed without any alteration. The swelling effect is however eliminated when the total creep is calculated as both the loaded and unrestrained "sealed" specimens are subjected to this swelling phenomenon.

This phenomenon, i.e. swelling of concrete when sealed, is especially important for tensile creep tests as the recorded creep strains can be up to an order less than for compressive creep tests due to the lower applied load. Nevertheless, it is not explored further in this study.

Finally, remarks are made on the magnitude of creep strains found. It is common practice to relate creep responses to a creep compliance or a creep coefficient, also known as a creep factor. The creep compliance factor, C_c is defined as the creep strain over a period of time per unit of stress as follow:

$$C_c = \frac{\varepsilon_c}{\sigma} \qquad (4.2)$$

With C_c the creep compliance, ε_c the creep strain and σ the applied stress. The creep coefficient is defined as:

$$\Phi = \frac{\varepsilon_c}{\varepsilon_e} \qquad (4.3)$$

with ε_e the elastic strain. It is useful to determine the long-term material stiffness, E_{long}, using:

$$E_{long} = \frac{E}{1+\Phi} \qquad (4.4)$$

with E the E-modulus at the time of loading.

It is commonly accepted that at 8 months, around 70 % of the 30 year creep has occurred (Kong & Evans, 1987) for ordinary concrete. If the assumption is made that the increase of creep of the ECC matrix is expected to be the same as ordinary, structural concrete, the magnitude of creep is summarised in Table 4.2 using Equation 4.2 and Equation 4.3. It is important to note that these creep values are strongly dependant on the specimen size as the creep strains include drying creep. For this reason the values are not compared to values of ordinary concrete.

Table 4.2 The creep results summarized.

	Creep compliance, C_c [mm/m/MPa]		Creep Coefficient, Φ [-]	
	8 months	30 years	8 months	30 years
Unsealed specimens	0.68	0.98	6.3	9.0
“Sealed” specimens	0.38	0.53	3.5	4.9

4.2 Cracked Section Creep Tests

In section 4.1 the creep of an uncracked ECC section was investigated and quantified. The true benefit of ECC is only utilised after the material has cracked. The creep of a cracked section is thus important as it would be the condition of the material during normal, intended use of ECC. For this reason tensile creep tests were done on ECC specimens that were cracked under controlled conditions before the tensile creep load was applied.

4.2.1 Experimental test program

The test setup and specimen preparation used for these tests are exactly the same as section 4.1, except that the specimens were cracked before they were tested. They were subjected to a direct tensile load in the tensile setup described in section 3.1 up to a level of 1 % strain at a strain rate of 104 μ/s. The specimens were loaded with the creep load within an hour after the cracking.

Eight specimens were tested and the test program is summarised in Table 4.3. The sustained load levels are expressed as a percentage of the ultimate strength which was defined for Table 4.1.

Table 4.3 Test program for the cracked creep specimens.

Loading as % of ultimate strength	30 %	50 %	70 %	80 %
Actual applied stress [MPa]	0.81	1.32	1.87	2.11
Number of specimens	2	2	2	2

Photos were taken of the specimens after they were cracked before the creep load was applied and again periodically during the creep tests. These photos are not of sufficient resolution to distinguish all the cracks or crack sizes. Note also that these specimens were sealed. These photos do however give an indication of how the damage evolved during the creep test.

Tests were also done to investigate the reloading of the specimens after they were prepared for the creep tests. This is important as no reference is available for the total, non-recoverable strain condition after the specimens are removed from the Zwick MTM and then taken to the creep load frame. The results will assist in attaining the correct starting point of the creep in a stress-strain graph of the specimen. For these reloading tests, four specimens were loaded to 1 % strain, unloaded and then loaded again past 1 % strain. The loading and unloading were all done at a strain rate of 104 μ/s.

4.2.2 Results

Firstly, before the creep results can be interpreted, the starting strain position for the creep tests was determined, as the starting position is unknown due to the permanent deformation caused by the pre-cracking of the specimens. To determine this starting

strain value, reloading tests were done on four specimens and the results are shown in Figure 4.9.

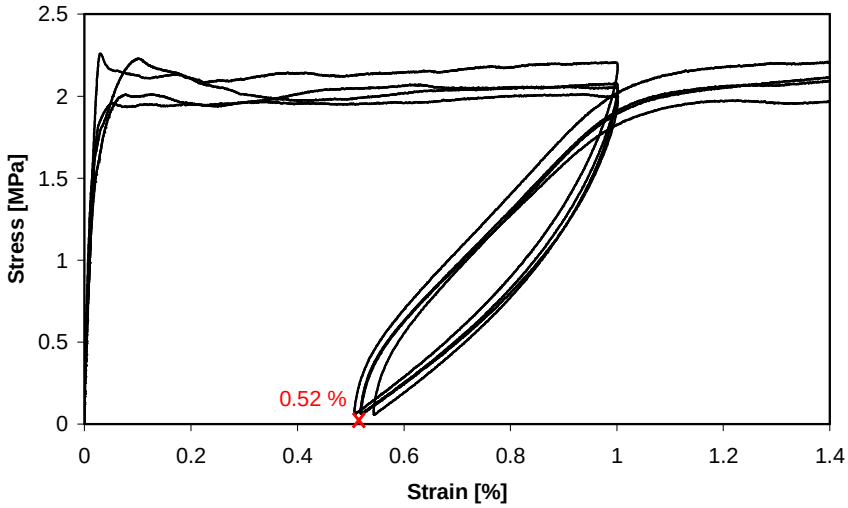

Figure 4.9 The results of the reloading tests with the estimated starting strain position for the creep tests indicated with a red cross.

To calculate the total time-dependant strain of the creep tests, this initial strain loading shown in Figure 4.9 as well as the strain increase due to the load application were deducted from the strain readings. These results include any other time-dependant response, e.g. shrinkage, and the increase (or decrease) of strain is thus called time-dependant strain rather than creep strain. The results are shown in Figure 4.10 a) for the individual time-dependant strains of the specimens. The averages for each loading percentage are shown in Figure 4.10 b).

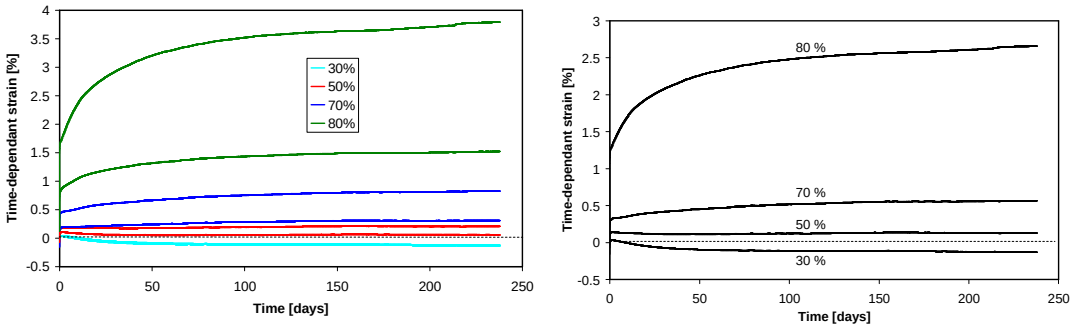

Figure 4.10 a) The individual time-dependant strains for the cracked creep tests. b) The average time-dependant strains for each loading percentage.

The shrinkage strain was not subtracted from the results shown in Figure 4.10 as the magnitude of shrinkage is unknown. The specimens were “sealed” as discussed in

section 4.1, but due to the cracks, the seal was broken and moisture loss could occur more freely. The moisture loss would however not be as fast as the case for an unsealed shrinkage specimen. It is however clear in Figure 4.10 that the creep dominates the time-dependant behaviour. Only at the load of 30 % was the shrinkage dominant. A possible solution to reduce the problem of the unknown shrinkage is to allow the specimens to become in equilibrium with the environment before the commencing of the creep tests. This would however under estimate the typical creep behaviour as a cement-based material that has dried before load application shows almost no creep (Pickett 1942).

To investigate the early time-dependant strains, i.e. the strain within the first day after loading, the first 5 hours is shown in Figure 4.11. This graph gives an indication that further crack formation occurred during the first hours after loading. Any further crack formation causes a sudden increase of strain as pointed out in Figure 4.11.

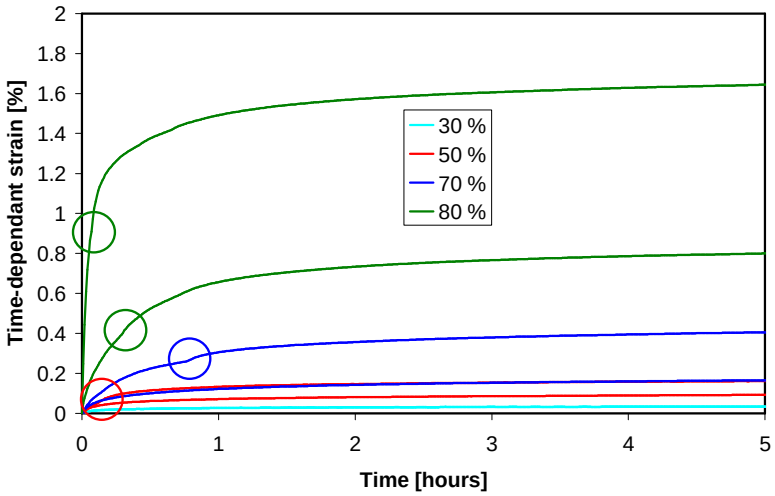

Figure 4.11 The time-dependant strain during the first 5 hours of loading. Jumps in the responses are marked to indicate possible crack formation.

To gain perspective of these time-dependant strain they are represented on a stress-strain graph together with typical tensile test results. This is done in Figure 4.12, which also shows representative tensile results from the tensile strain rate tests described in Chapter 3. The two specimens of each loading percentage are marked with red and blue indicators respectively. The points where the creep started are indicated with a black cross. The total time under sustained load of each indicator is also shown.

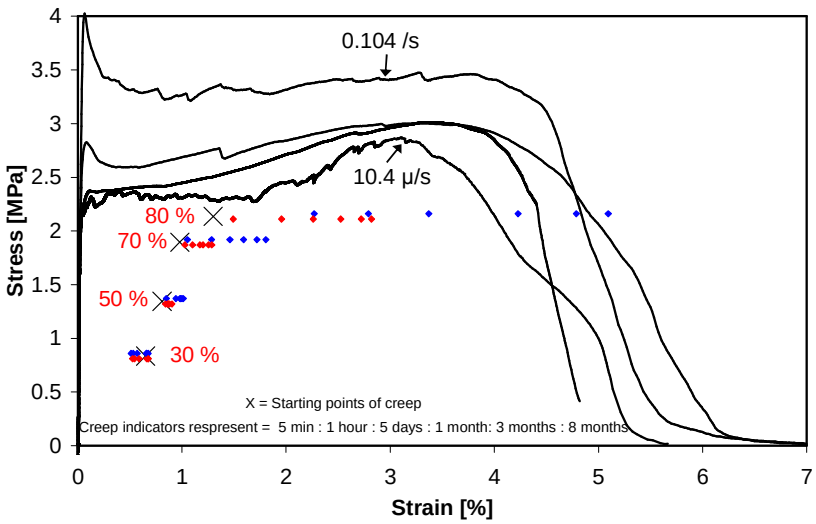

Figure 4.12 The time-dependant strains of the creep tests are shown together with representative tensile results from Chapter 3. For each loading % the individual results are shown in blue and red indicators so that they can be interpreted separately.

The creep shown in Figure 4.12 is alarmingly high. One of the specimens loaded with a 80 % creep load crept beyond the softening branches of the tensile test. After 8 months this specimen still showed no signs of failure. For a specific set of notched concrete beams under sustained loading, it was found that failure occurs when the flexural response reaches the softening branch of the static test results (Zhou 1992). This is however not the case for these ECC specimens, as the mechanism that causes the strain increase over time is not the same as for ordinary concrete.

Photos of the crack pattern of this specimen are shown at different times under sustained loading in Figure 4.13. The quality of the photos and sealant on the specimens make it difficult to determine if more cracks initiated after time. It is however clear to see is that the cracks widened in time.

4.2.3 Discussion

The creep tests reported in this section are different to the tests of Section 4.1 as the tests in Section 4.1 were on uncracked specimens while these test specimens were pre-damaged. The tests in this section were loaded at a load lower than what caused the pre-damage. These tests represent material on which an event occurred which mobilised the strain hardening capacity of the material, e.g. earthquake or extreme live loading, after which the load was reduced to a lower, sustained load.

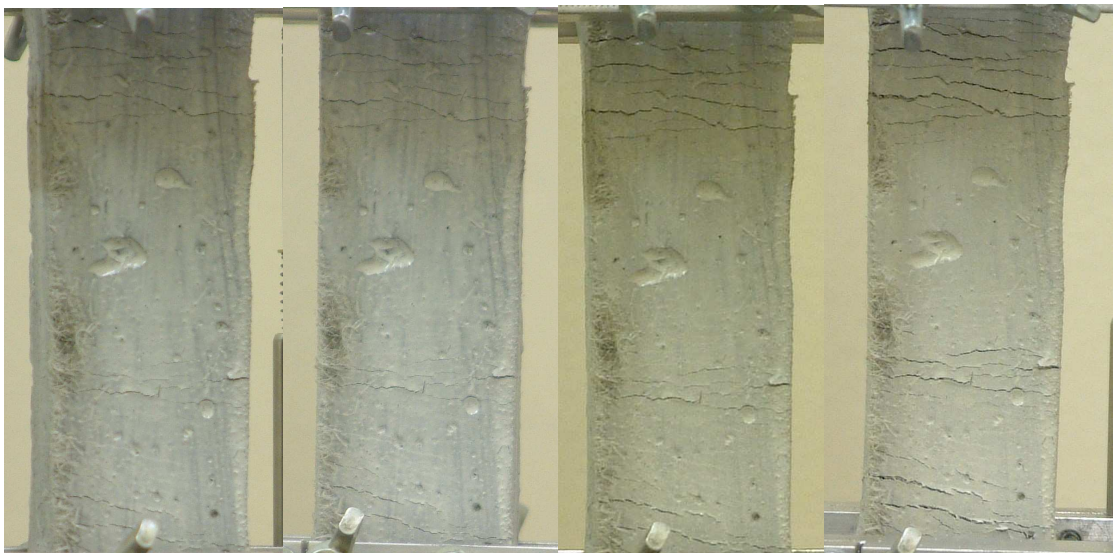

Figure 4.13 Photos taken of one of the cracked creep specimens loaded at 80 %. The time after loading is from left to right: 30 min, 12 hours, 6 days and 8 months.

To further analyse the results the creep compliance, C_c, is calculated. The average time-dependant strains at the end of the 8 months are taken and the shrinkage of the "sealed" test specimen was subtracted. As discussed earlier, more shrinkage occurred than the "sealed" specimens due to the cracks, thus these calculated values can be considered conservative. The C_c's are then calculated using Equation 4.2. The values are shown in Figure 4.14.

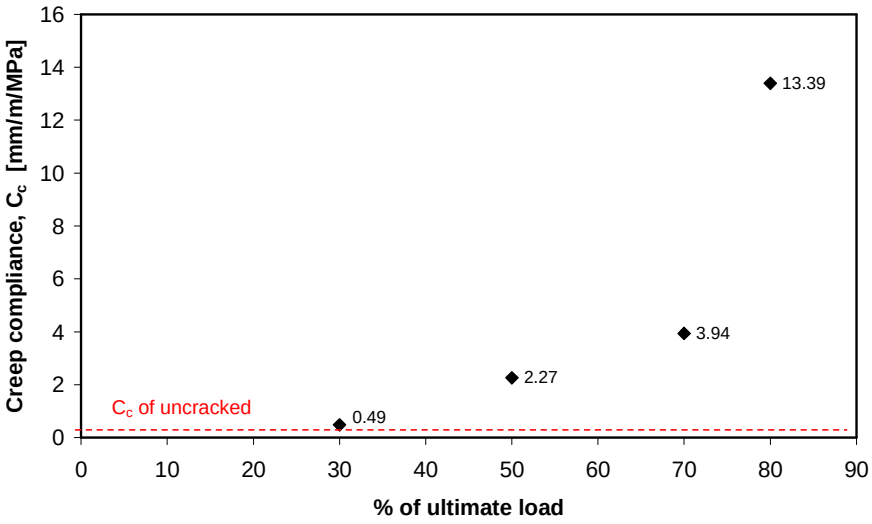

Figure 4.14 The creep compliance, C_c, of a cracked section loaded at different levels. The values of C_c are indicated on the graph and a red dotted line represents the C_c of the uncracked material if the creep response is assumed to be linearly dependant on the stress.

Note that the C_c of the 30 % loading is close to the value for the uncracked material. However, for the higher sustained load the C_c values were far more than the uncracked sections and in the case of the 50 % loading it is more than 4 times that of the uncracked sections.

From these results the creep compliance of a cracked or uncracked section appear to be the same up to a loading value of 30 % of ultimate load. Beyond the 30 % loading the creep compliance of the cracked section increases exponentially. This increase could only be attributed to an increase in number of cracks and/or the increase of the crack widths. A crack width increase could only be caused by the creep of fibre and/or the time-dependant pull-out of fibres and will be investigated later in this chapter.

The mechanism of this increased creep can be further investigated on the macro-level by looking at the photos of the one specimen loaded at 80 % shown in Figure 4.13. The cracks clearly widened over time. Although the quality of photos and the sealant prevent a conclusion on the formation of new cracks, there are signs on Figure 4.11 that new cracks formed in the first hour of the creep load application.

4.3 Single Fibre Creep and Time-Dependant Pull-Out

To investigate the mechanism causing the increased creep of ECC when the material is cracked, creep tests were done on the single fibre level. The cause of the cracks widening under constant load shown in the previous section can be due to fibre creep and/or the time-dependant pull-out of fibres from the matrix. Both these mechanisms were investigated with experimental tests and are discussed in the following sections.

For the time-dependant pull-out creep tests, two sets of tests were done, one set of which the fibre had already debonded from the matrix, and the other had no previous debonding of the fibre. For the fibre creep test, the length change of a fibre was monitored during a constant load application.

4.3.1 Test setup

For the time-dependant fibre pull-out creep tests, the same test setup was used as in Section 3.3. Due to the long duration (up to 70 hours) of the tests, the displacement

readings of the bottom crosshead are insufficient for accurate pull-out displacements. The bottom platen of the testing machine is not fixed for rotation around the vertical axis and a small rotation does occur over time. Movement does not occur during normal testing, but if a test occurs over a period of more than 24 hours, a slight movement can be found. For these force controlled tests, such movement would not influence the test, but it would cause the displacement readings to be inaccurate due to the adjustment of the bottom platen by the control unit to insure a constant load.

For this reason the pull-out displacements were measured with an alternative method. A microscope with a 1 Mega-pixel camera was used to take photos at given intervals. These photos were used to obtain the pull-out displacement by scaling. The thickness of the fibre, i.e. 40 μm, was used as a scale reference. A photo of the microscope used can be seen in Figure 3.25.

The fibre creep tests were done with a similar test setup as the rate-dependant fibre pull-out tests shown in Figure 3.26, except that another fibre mounting plate was fixed to the bottom base plate as shown in Figure 4.15 so that both ends of the fibre could be glued. The creep deformation of the fibre was also measured by scaling from the microscope photos.

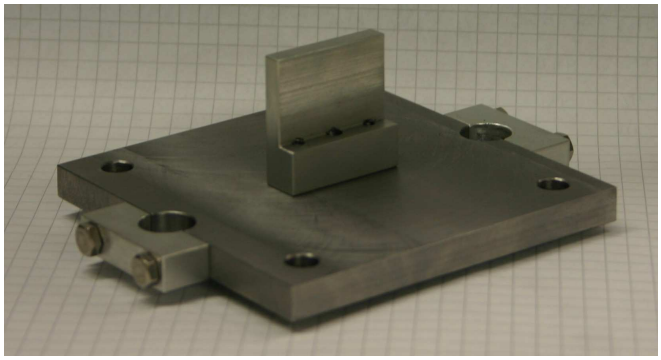

Figure 4.15 The fibre mounting plate fixed to the bottom base plate.

4.3.2 Test program

As mentioned earlier, the time-dependant fibre pull-out tests were split into two groups, i.e. a group of which the fibres were not debonded before the test started, and the other the fibres were fully debonding along the embedment length of the fibre. Full debonding was achieved by pulling the fibre out at a constant rate until the response indicated that full debonding occurred, as described in Section 3.3.

The same mix, mixing procedure, curing and method of preparation of the test samples were used as described in detail in Chapter 3.

Three tests of each set were done at a load of 50 % of the average τ_0 found in Section 3.3, i.e. 2.4 MPa. The load was kept constant until the fibre pulled out completely. The test program is summarised in Table 4.4 together with the actual initial embedment lengths of each test.

Table 4.4 Test program for the time-dependant fibre pull-out creep tests.

	Debonded tests			Fully bonded tests		
Number of specimens	3			3		
Actual embedment lengths [mm]	1.3	1.3	1.4	1.4	1.5	1.35
Loading, τ_0 [MPa]	1.2 MPa			1.2 MPa		

For the fibre creep test, only one fibre was tested. This test was to get an indication of the fibre creep, as the test setup is not ideal for determining the creep characteristics of the fibre. The fibre was loaded at 50 % of its ultimate capacity, i.e. 50 % of 1560 MPa which relates to a force of 1.01 N. The force was kept constant for a duration of 60 hours and photos were taken with the microscope at specific time intervals which were used to determine the time-dependant increase of the length of the fibre.

4.3.3 Test results

All the time-dependant fibre pull-out creep tests resulted in failure, i.e. the fibre pulled out of the matrix over a period of time. The time to failure of the tests are indicated in Figure 4.16 for each set of tests, i.e. debonded and non-debonded fibres, independently, together with the average values.

For the calculation of the pull-out displacement of the fibres the method of using microscope photos was used as described in the previous section. An example of this method is shown in Figure 4.17.

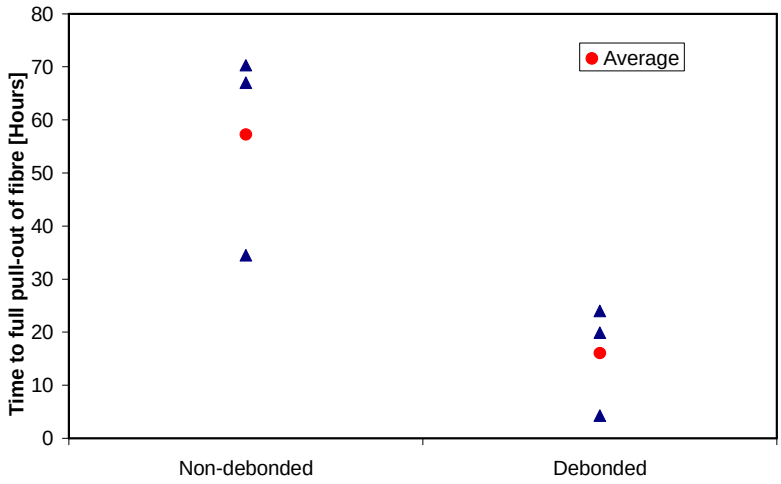

Figure 4.16 The time to failure for the time-dependant fibre pull-out creep tests loaded at 50 % of ultimate resistance.

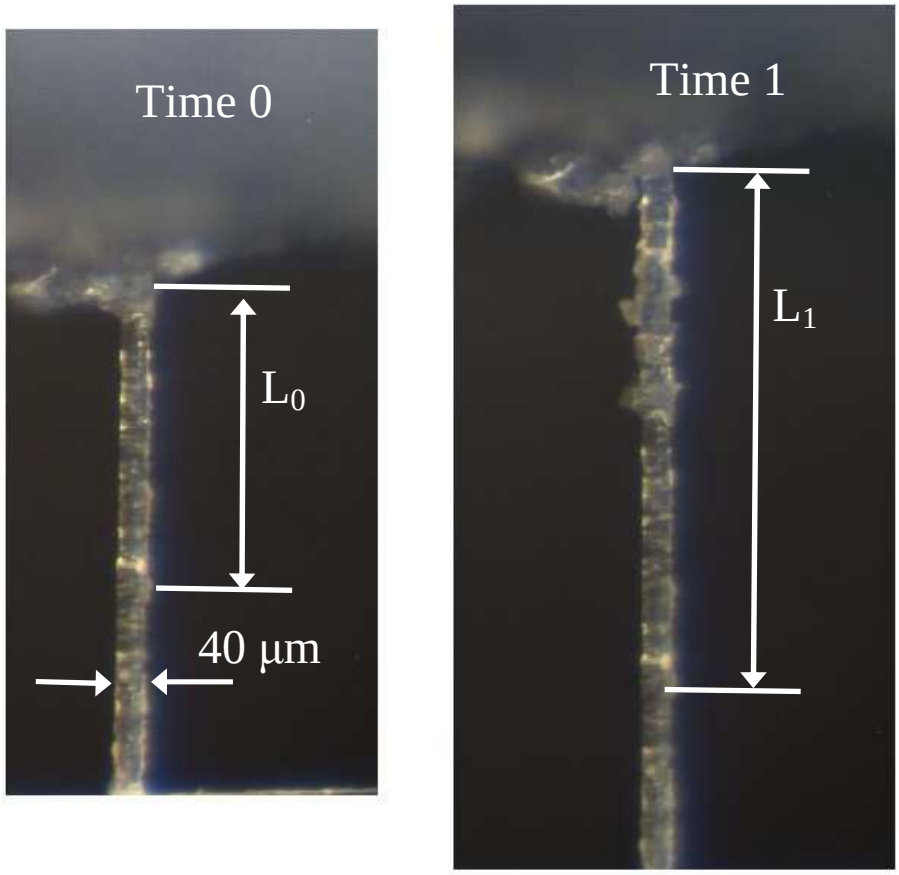

Figure 4.17 An example of the fibre pull-out displacement calculation using the microscope photos with the pull-out displacement at Time 1 being the difference between L_0 and L_1. The fibre diameter is used as a scale.

The fibre pull-out displacements over time calculated using the aforementioned method are shown in Figure 4.18. The failure occurred directly after the last shown reading.

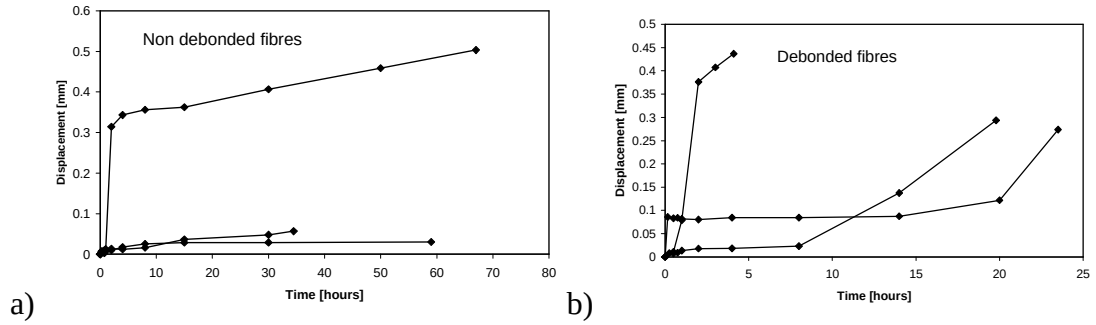

a) b)

Figure 4.18 The fibre pull-out displacements over time shown for the non debonded, a), and debonded fibres, b).

For the fibre creep test, the microscope method was used to determine, in this case, the increase of the length of the fibre over time. For this, two marks were identified on the fibre and the distance between these two marks was measured using the microscope photos over a period of 60 hours, shown in Figure 4.19. The measured lengths are shown in Figure 4.20. A line is also shown in the graph to indicate what the measured lengths would be if a small amount of creep, i.e. 0.5 % linearly occurred over 60 hours. The fibre was loaded at 780 MPa, i.e. half the tensile capacity of the fibre.

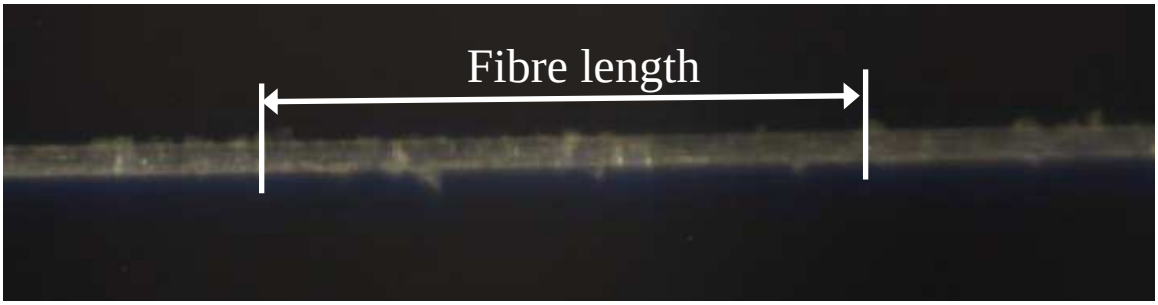

Figure 4.19 The fibre length measured using the microscope photo method over a period of 60 hours.

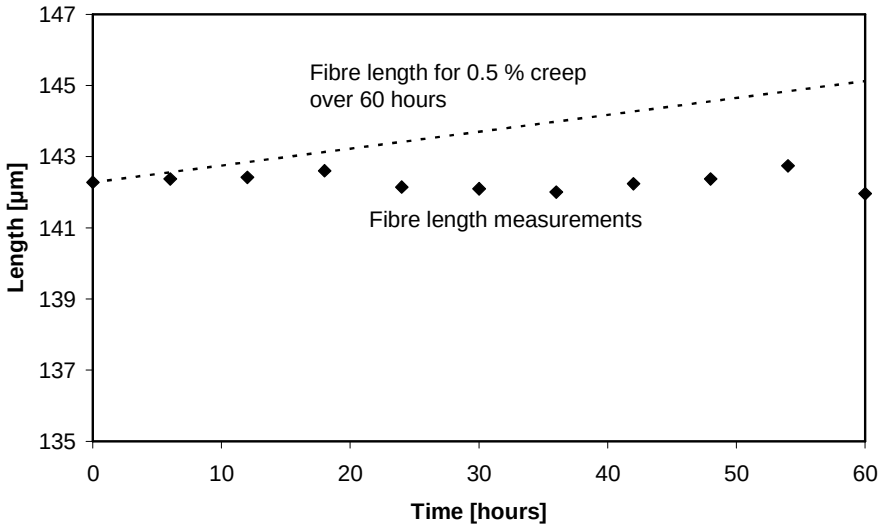

Figure 4.20 The length measurement of the fibre creep test together with a line to indicate what the response would be if a linear creep of 0.5 % over 60 hours would realise.

4.3.4 Discussion of results

It is alarming to note that all the fibres tested for the fibre pull-out creep test pulled out within 70 hours at a load as low as 50 % of the expected strength. This shows that creep fracture is possible on this small scale.

The average time to pull-out for non-debonded creep tests was 57 hours while for the debonded tests, 16 hours. This shows that after the full debonding of a fibre in the matrix, the resistance to creep reduces significantly.

The responses of the pull-out displacements of the fibres plotted against time in Figure 4.20 shows no clear trend for the rate of pull-out at a constant load. There is however an indication that the debonded fibres tend to start pulling out as soon as the load is applied, while the non-debonded fibres show initial resistance to the load in the first part of the test.

The results of the single fibre pull-out creep tests are not representative of the true conditions in an ECC material. Firstly, the embedment lengths of the tests were between 1.3 and 1.5 mm while the embedment length in the ECC matrix under investigation is up to 6 mm, i.e. half the fibre length. Secondly, no fibres were tested that were embedded at an angle to simulate real orientations in a matrix with randomly oriented fibres. Thirdly, the applied load in the fibre creep tests is higher than the load per fibre in a tensile test on an ECC specimen. The equivalent uniformly distributed stress over a crack plane can be calculated with:

$$\sigma_{crack\ plane} = \frac{4 L_e \tau V_f}{d} \qquad (4.5)$$

When assuming that 2 % of the crack plane is bridged by fibres (V_f), all the fibres are embedded at 1.2 mm (L_e) and a uniform shear resistance (τ) of 1.2 MPa exists on the fibres' interface, the distributed stress over the crack plane is calculated as 3.36 MPa.

For the fibre creep tests however, no sign of creep was observed within the measured resolution. If there was any creep of the fibres, it was less than 0.5 % over 60 hours, as seen in Figure 4.20. It can be shown with a small numerical example that even creep of 0.5 % of the fibres is negligible. For this example it is assumed that only the part of the fibre that is pulled out of the matrix in a crack can undergo creep. If there are 10 cracks over a gauge length of 80 mm, and each crack width is conservatively chosen at 100 μm, the added length to the specimen due to the fibre creep if the fibres are tensioned at 800 MPa, once again very conservative, would be 5 μm. If this is expressed in terms of strain over the gauge length, it would increase the creep compliance, C_c by only 0.063 mm/m/MPa which is insignificant compared to the values of Figure 4.14. The fibre creep is thus negligible in this application.

To conclude, it is found in this section that fibre creep does not contribute to the crack widening phenomenon found under a constant creep load and that the crack widening phenomena can be attributed to the time-dependant pull-out of the fibres. Creep fracture did occur on this level, but at a load higher than the maximum capacity of ECC in tension.

4.4 Concluding summary

In this chapter, creep and shrinkage tests were done to further investigate the time-dependant behaviour of ECC. Creep tests were done not only on the tensile macro-level, but also on the single fibre level.

On the single fibre level it was found that the fibres alone, under a relative high tensile load, do not show any significant creep. However, the fibres embedded in the matrix which were loaded with a creep load did show significant creep. At a sustained pull-out force of half the total pull-out resistance, fibres pulled out completely after an

average of 57 hours. However, if the fibres were debonded in the matrix before the onset of the creep load, the average pull-out time was reduced to 16 hours. This clearly shows that the time-dependant pull-out of the fibres is an important source of time-dependant behaviour.

Tensile creep tests on the macro-level showed that the creep behaviour of an uncracked section of ECC is typical of a cement-based material. An unexpected, yet significant finding was that a creep specimen loaded at 50 % of the ultimate strength cracked within 4 hours after the application of the creep load. This process of crack formation brought forth a significant increase in the tensile creep strain and creep rate.

To experimentally simulate the creep behaviour of a cracked ECC section, specimens were loaded to 1 % tensile strain before a creep load was applied. Creep loads ranged from 30 % to 80 % of the ultimate strength. It was found that the creep of a cracked section is significantly more than that of an uncracked section. The creep strains also increased substantially with an increase of the creep load. Indications are that new cracks are formed in the early stage of sustained loading while over the long term, the crack widths were shown to increase over time. This widening can be attributed to the time-dependant fibre slippage over the crack planes.

A logical conclusion can be made that the tensile creep deformation of ECC consists of three parts, namely the matrix creep, the time-dependant crack formation and the time-dependant fibre pull-out. It was also shown that the magnitude of the creep deformation is dependant not only on the creep load, but also the current deformation of ECC caused by cracking.

CHAPTER 5

Modelling of ECC Mechanical Behaviour

Computational modelling of building materials becomes more and more important for structural design of complex structural systems, but also the optimisation of structural elements. With accurate material models it is possible to test structural elements without physically building them and testing them in laboratories.

Nonlinear constitutive models for concrete have been used in finite element analyses for the past three to four decades, but are still improving in the accurate representation of the mechanical response and fracture of concrete. In the late 1960's, two landmark papers, Rashid (1968) and Ngo and Scordelis (1967), were published which are known to be the first steps of finite element modelling of the fracture of concrete. For a summary of the further development of computational concrete models the reader is referred to De Borst (2002). A problem with complex constitutive models is however that they are not usable by design engineers as a design tool due to the complex nature of many of the models and the time consuming solution algorithms required. Nevertheless, finite element analysis is a robust and accurate numerical solution to structural mechanics. A finite element framework is used in this research project to numerically analyse the structural behaviour of ECC.

Several scholars have simulated ECC behaviour with finite element methods. Kabele (2000) formulated a model to simulate the mechanical behaviour of ECC using a smeared cracking approach. Despite acknowledging that a discrete cracking model would be best for the final localising crack, Kabele decided to use a smeared cracking approach for the localisation. This is due to the uncertainty of the position of the final localising crack. Another model was proposed by Han et al (2003). This model was created to simulate the behaviour of ECC under cyclic loading to test the

improvement of structural response if ECC elements are used to dissipate energy during earthquake loadings. Computational modelling of ECC was also performed by Simone et al (2003) who used an embedded discontinuity approach for the final material softening. This method would have the same kinematic characterisation as one obtained with interface elements (the reader is referred to Rots (1986) for a discussion of interface elements) for discrete cracking, but does not require remeshing procedures. Their conclusion was that it did not simulate the experimental results of ECC satisfactorily due to the simplicity of the model.

5.1 Constitutive Model

The two most widely used and accepted approaches for the numerical modelling of the mechanical behaviour and fracture of concrete are a continuum damage mechanics approach and a continuum elasto-plasticity model. Both can be implemented as a smeared cracking approach, i.e. the strains caused by the crack openings are added to the total strain of a material point compared to discrete crack modelling where specific interface elements are placed strategically to act as crack openings. The discrete cracking approach is not suitable for ductile materials such as ECC because the crack position and path is not always known beforehand. To automate the appropriate placement of interface elements in the discrete modelling process, an intricate remeshing technique would be required to incorporate cracking of ECC. In this research project a smeared cracking approach is chosen.

Even though the damage mechanics and elasto-plasticity approaches can be implemented to give similar results in most cases, a clear difference can be seen in the unloading behaviour of these two models. Using a standard damage approach the material would exhibit full unloading, i.e. no residual strains when the stress is released. This type of unloading is also referred to as full secant unloading. Plasticity on the other hand, will have residual strain when unloaded and the unloading would take place with the same gradient as the initial elastic loading. These effects are shown schematically in Figure 5.1.

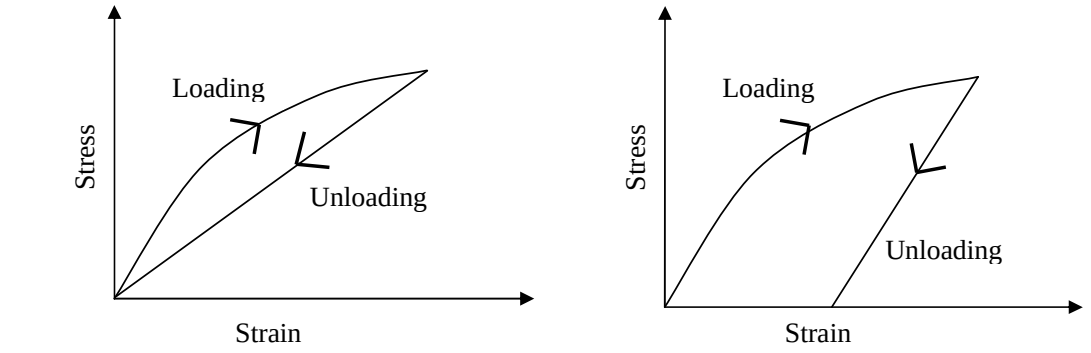

Figure 5.1 The unloading behaviour of a), a damage formulation and b), a plasticity implementation.

Another important difference between the two models is the fracture or yielding criterion. Plasticity based constitutive models use a stress based yielding criterion or limit function. This implies that the non-linear behaviour is driven by a stress limitation formulation. Limit functions for the compression and tension can be combined to produce a multi-surface limit function/criterion (Feenstra 1993, Van Zijl 2000).

A damage approach, in contrast, uses a strain based fracture criterion. The formulation used to determine the state of damage is calculated using the current strain condition (De Borst 2002).

The physical interpretation of the unloading of these models is that a damage approach implies that the crack openings in the material will close completely when the material is unloaded. With plasticity, however, cracks will not close during unloading as the strain caused by the cracking is permanent. Not one of these two models is true to the actual response of a cement-based material. The correct representation would be obtained by a combination of the two models. In Figure 2.3 the unloading behaviour of ECC is shown to be in between secant unloading and elastic unloading. For the purpose of this research project, the damage approach is chosen for fracture of ECC.

5.1.1 Constitutive Damage Mechanics

The basic relation used in an elastic computational model is:

$$\bar{\sigma} = \bar{\bar{D}}^{e}\bar{\varepsilon} \qquad (5.1)$$

The stress vector, $\bar{\sigma}$:

$$\bar{\sigma} = \begin{Bmatrix} \sigma_x \\ \sigma_y \\ \tau_{xy} \end{Bmatrix} \quad (5.2)$$

is related to the strain vector, $\bar{\varepsilon}$:

$$\bar{\varepsilon} = \begin{Bmatrix} \varepsilon_x \\ \varepsilon_y \\ \gamma_{xy} \end{Bmatrix} \quad (5.3)$$

via the elastic stiffness matrix, $\bar{\bar{D}}^e$:

$$\bar{\bar{D}}^e = \frac{E}{1-\upsilon^2}\begin{bmatrix} 1 & \upsilon & 0 \\ \upsilon & 1 & 0 \\ 0 & 0 & (1-\upsilon)/2 \end{bmatrix} \quad (5.4)$$

with E the material stiffness and ν the Poisson's ratio. Note that these vectors and matrix are shown for the plane stress case.

The damage approach is based on the reduction of the stiffness of the material when damage evolves, using a damage indicator scalar, ω, which ranges from 0, no damage, to 1, total damage, as follows:

$$\bar{\sigma} = (1-\omega)\bar{\bar{D}}^e\bar{\varepsilon} \quad (5.5)$$

The relation shown in Equation 5.5 can also be expressed in rate form as:

$$\dot{\bar{\sigma}} = (1-\omega)\bar{\bar{D}}^e\dot{\bar{\varepsilon}} - \dot{\omega}\bar{\bar{D}}^e\bar{\varepsilon} \quad (5.6)$$

The formulation of ω and its derivative are shown in the next sections.

5.1.2 Damage evolution

To model the ECC behaviour based on a one-dimensional tensile response, a scalar is required to represent the strain vector of any material point. This is done with an equivalent strain, $\tilde{\varepsilon}$, which is a one-dimensional representation of the current strain condition. The particular equivalent strain definition chosen for the current model will be defined in section 5.2. Damage is considered to initiate once a threshold strain level is exceeded. In ECC, the dominating source of nonlinearity is cracking, so the threshold strain is a positive equivalent strain value defined as $\tilde{\varepsilon}_0$. Once this threshold is breeched, damage accumulates, described by a damage loading function as:

$$f(\tilde{\varepsilon}) = \tilde{\varepsilon} - \tilde{\varepsilon}_H \qquad (5.7)$$

with $\tilde{\varepsilon}$ an equivalent strain and $\tilde{\varepsilon}_H$ an equivalent strain history variable which represents the largest equivalent strain achieved up to the current point in time. The so-called Kuhn Tucker loading-unloading conditions apply:

$$f \le 0, \quad \dot{\tilde{\varepsilon}} \ge 0, \quad f\dot{\tilde{\varepsilon}} = 0 \qquad (5.8)$$

This means that, if the previously largest equivalent strain level is exceeded, i.e. the damage loading function (Equation 5.7) is positive, the damage level increases, and the history parameter $\tilde{\varepsilon}_H$ is updated to the new, increased level to ensure that the damage loading function remains non-positive. If the damage loading function (Equation 5.7) is negative at a material point, the threshold is not exceeded either because the material is undamaged or it is unloading, ω and $\tilde{\varepsilon}_H$ remain unchanged, i.e. the state of damage at the material point does not increase. Note, however, that the state of damage cannot decrease, as it is considered irreversible. The stress level depends on the strain and damage level. When loading occurs beyond the threshold strain, i.e. damage occurs, $\tilde{\varepsilon}_H$ becomes the current equivalent strain and the stress is found as a function of $\tilde{\varepsilon}_H$:

$$\sigma = \sigma(\tilde{\varepsilon}_H - \tilde{\varepsilon}_0) \qquad (5.9)$$

If Equation 5.9 is combined with Equation 5.5, considered in one dimension, the damage variable becomes:

$$\omega = 1 - \frac{\sigma(\tilde{\varepsilon}_H - \tilde{\varepsilon}_0)}{E\tilde{\varepsilon}} \qquad (5.10)$$

The damage variable can now be related to the uni-axial tensile behaviour of ECC as schematised in Figure 5.2. Note that the typical pseudo strain hardening tensile response, as discussed in Chapter 2 is simplified and represented by a tri-linear stress-strain relation. The damage index variable ω can now be solved directly from Equation 5.10 and the linear representations of the strain hardening and strain softening regimes. This leads to expressions for strain hardening: ($\varepsilon_0 \le \tilde{\varepsilon}_H < \varepsilon_{sh} + \varepsilon_0$):

$$\omega = 1 - \frac{\sigma_{tu} - \sigma_{fc}}{E\varepsilon_{sh}} + \frac{\varepsilon_0(\sigma_{tu} - \sigma_{fc}) - \sigma_{fc}\varepsilon_{sh}}{E\varepsilon_{sh}} \tilde{\varepsilon}_H^{-1} \qquad (5.11)$$

$$\frac{\partial \omega}{\partial \tilde{\varepsilon}_H} = \frac{\sigma_{fc}\varepsilon_{sh} - \varepsilon_0(\sigma_{tu} - \sigma_{fc})}{E\varepsilon_{sh}} \tilde{\varepsilon}_H^{-2} \qquad (5.12)$$

and for strain softening: ($\varepsilon_{sh} + \varepsilon_0 \le \tilde{\varepsilon}_H < \varepsilon_{tu} + \varepsilon_0$):

$$\omega = 1 + \frac{\sigma_{tu}}{E(\varepsilon_{tu} - \varepsilon_{sh})} - \frac{\sigma_{tu}(\varepsilon_{tu} + \varepsilon_0)}{E(\varepsilon_{tu} - \varepsilon_{sh})} \tilde{\varepsilon}_H^{-1} \qquad (5.13)$$

$$\frac{\partial \omega}{\partial \tilde{\varepsilon}_H} = \frac{\sigma_{tu}(\varepsilon_{tu} + \varepsilon_0)}{E(\varepsilon_{tu} - \varepsilon_{sh})} \tilde{\varepsilon}_H^{-2} \qquad (5.14)$$

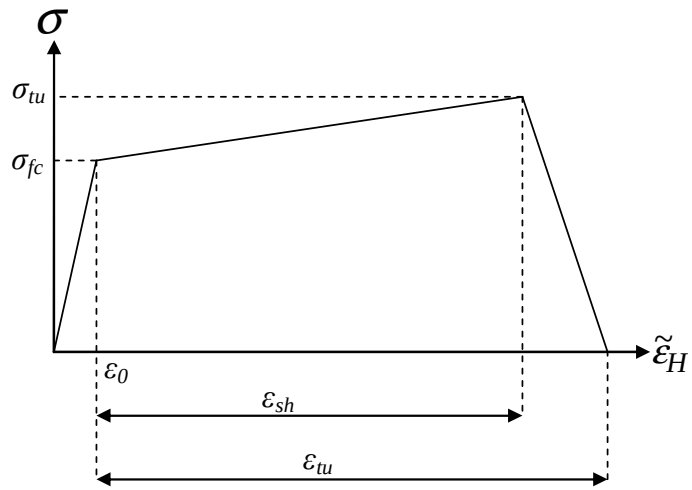

Figure 5.2 Tri-linear representation of the tensile response of the material.

The derivatives of the damage variable with regard to equivalent strain for the respective hardening and softening regimes are given in Equations 5.12 and 5.14. They are required to define a tangent modulus, also known as the Jacobian, in a finite element implementation. The Jacobian will be discussed in the next section.

5.1.3 Jacobian

An accurate estimation of the current stiffness is beneficial for efficient numerical solution of the global non-linear response. This is effectively combined with a regular Newton Raphson or arc-length methods. To acquire the expression for the current stiffness, $\dot{\omega}$ of Equation 5.6 has to be partially differentiated to read:

$$\dot{\omega} = \frac{\partial \omega}{\partial \tilde{\varepsilon}_H} \frac{\partial \tilde{\varepsilon}_H}{\partial \tilde{\varepsilon}} \frac{\partial \tilde{\varepsilon}}{\partial \bar{\varepsilon}} \dot{\bar{\varepsilon}} \qquad (5.15)$$

with

$$\frac{\partial \tilde{\varepsilon}_H}{\partial \tilde{\varepsilon}} = 1 \quad \textit{when loading} \qquad (5.16)$$

$$\frac{\partial \tilde{\varepsilon}_H}{\partial \tilde{\varepsilon}} = 0 \quad \textit{when unloading} \qquad (5.17)$$

The partial derivative of the equivalent strain with regard to the strain vector will be shown in the next section. Equation 5.15 can now be substituted in Equation 5.6 to produce:

$$\dot{\bar{\sigma}} = \left[\overline{\overline{D}}^{e} \left(1 - \omega - \frac{\partial \omega}{\partial \tilde{\varepsilon}_H} \frac{\partial \tilde{\varepsilon}_H}{\partial \tilde{\varepsilon}} \frac{\partial \tilde{\varepsilon}}{\partial \bar{\varepsilon}} \bar{\varepsilon} \right) \right] \dot{\bar{\varepsilon}} \qquad (5.18)$$

The Jacobian is the terms between the square brackets in Equation 5.18.

5.2 Equivalent Strain

For the damage evolution to occur, a scalar representing the strain condition at a certain material point is required and is called the equivalent strain. Using this one dimensional representation of the strain vector it is possible to use the results of a direct tensile test as parameters for the damage evolution as shown in Figure 5.2.

The two most commonly used definitions for equivalent strain are the elastic energy:

$$\tilde{\varepsilon} = \frac{1}{2} \bar{\varepsilon}^{T} \overline{\overline{D}}^{e} \bar{\varepsilon} \qquad (5.19)$$

and the maximum principal strain:

$$\tilde{\varepsilon} = \sqrt{\frac{1}{2} \bar{\varepsilon}^{T} \overline{\overline{P}}_T \bar{\varepsilon}} + \frac{1}{2} \bar{\pi}^{T} \bar{\varepsilon} \qquad (5.20)$$

with

$$\overline{\overline{P}}_T = \frac{1}{2} \begin{bmatrix} 1 & -1 & 0 \\ -1 & 1 & 0 \\ 0 & 0 & 1 \end{bmatrix} \qquad (5.21)$$

$$\bar{\pi} = \begin{bmatrix} 1 \\ 1 \\ 0 \end{bmatrix} \qquad (5.22)$$

For tensile dominated boundary value problems it makes sense to relate the equivalent strain directly to the maximum principal strain. This means that damage is considered to evolve in the direction of the maximum principal tensile strain, once the threshold strain level is exceeded. This implies a rotating crack concept, as the principal strain direction at a material point may change during loading and an increase of strain in any direction will add to the crack width included in the total strain.

When using the maximum principal strain definition for the equivalent strain and a uni-axial tensile load is applied to an element, the tensile response computed, referred to as mode I response, produces exactly the same response as the prescribed constitutive law shown in Figure 5.2. However, if a biaxial stress is applied, the correct constitutive behaviour is not produced. This is due to Poisson's ratio. For the case of pure shear, referred to as mode II, which is equivalent to diagonal tension-compression, a reduced resistance is computed. These two responses, mode I and mode II, are compared in Figure 5.3. By simple stress analysis of the two boundary value problems, the stress limit ratio for a given principal strain value is given by the ratio:

$$\frac{\sigma_1^{Mode\ II}}{\sigma_1^{Mode\ I}} = \frac{1}{1+\nu} \qquad (5.23)$$

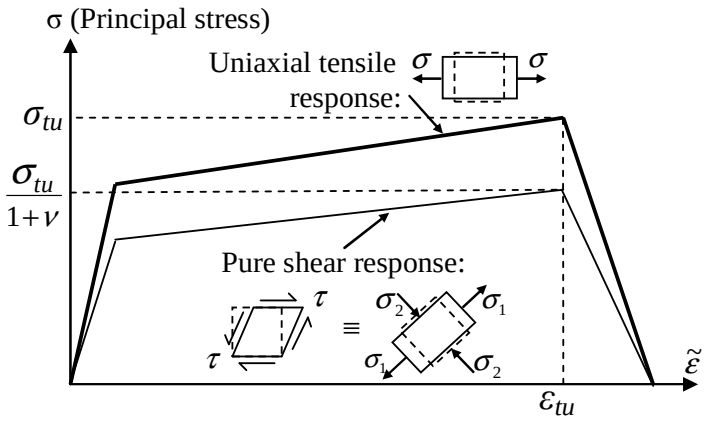

Figure 5.3 The effect of the maximum principal strain as the definition for the equivalent strain on the mode II response compared to a mode I response.

For high values of Poisson's ratio applicable for ECC in the order of $0.3 < \nu < 0.35$ a significantly reduced resistance in shear is computed when using the maximum principal strain definition for the equivalent strain. For this reason, a new definition of the equivalent strain is formulated in this research as:

$$\tilde{\varepsilon} = \frac{1}{(1+\upsilon)}\sqrt{\frac{1}{2}\bar{\varepsilon}^T \overline{\overline{P}}_T \bar{\varepsilon}} + \frac{1}{2(1-\upsilon)}\bar{\pi}^T \bar{\varepsilon} \qquad (5.24)$$

With this formulation the uni-axial tensile response is left unaltered, and the pure shear response is now equal to the uni-axial tensile response when shown as a principal stress against the new equivalent strain. However, when the response is shown against the principal strain, a larger deformability is computed for the pure shear case, as shown in Figure 5.4.

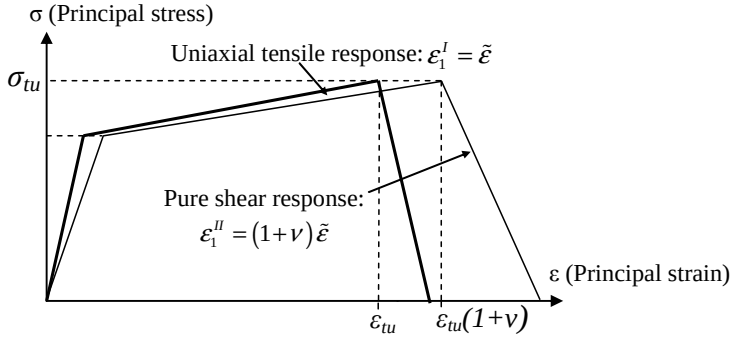

Figure 5.4 The response with the modified equivalent strain definition shown as the maximum principal stress against the principal strain.

The effect of the new definition of the equivalent strain can also be shown with a simple numerical example. For this example a material stiffness is chosen as 1, and the stress at which the damage threshold is passed also 1. This would imply that the equivalent strain at which the damage should begin is 1. A Poisson's ratio value of 0.35 is used. The damage evolution relies on the equivalent strain in order to produce the correct state of damage, thus if the produced equivalent strain is incorrect, the response would be incorrect. If a bi-axial stress condition is applied to an element with the first principal stress, σ_1, equalling 1 and the second principal stress, σ_2, ranging from -10 to 10. The equivalent strain should be 1 for all the values of σ_2 ranging from -10 to 1, as the value of σ_1 stress equals the damage threshold. The values of the maximum principal strain as well as the modified equivalent strain are plotted in Figure 5.5.

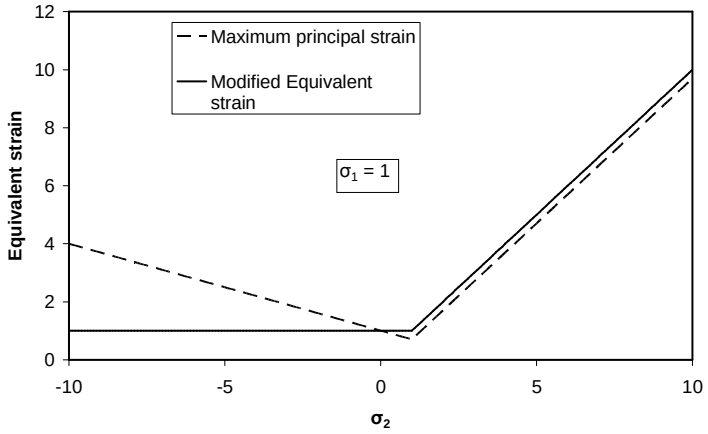

Figure 5.5 A numerical example to show the effect of the definitions of the equivalent strain in a bi-axial stress condition.

It is clear that the maximum principal strain definition does not give the correct values in a bi-axial loading condition. The modified equivalent definition does however give the desired results.

The modified definition of equivalent strain is chosen for this research due to the improvement of the shear response. The derivatives of the equivalent strain with regard to the strain vector are required to complete the expression of the Jacobian (Equation 5.18) in the previous section. The derivative coordinates are:

$$\frac{\partial \tilde{\varepsilon}}{\partial \varepsilon_x} = \frac{1}{2(1-\upsilon)} + \frac{1}{2(1+\upsilon)}\left((\varepsilon_x - \varepsilon_y)^2 + {\gamma_{xy}}^2\right)^{-0.5}(\varepsilon_x - \varepsilon_y) \qquad (5.25)$$

$$\frac{\partial \tilde{\varepsilon}}{\partial \varepsilon_y} = \frac{1}{2(1-\upsilon)} - \frac{1}{2(1+\upsilon)}\left((\varepsilon_x - \varepsilon_y)^2 + {\gamma_{xy}}^2\right)^{-0.5}(\varepsilon_x - \varepsilon_y) \qquad (5.26)$$

$$\frac{\partial \tilde{\varepsilon}}{\partial \gamma_{xy}} = \frac{1}{2(1+\upsilon)}\left((\varepsilon_x - \varepsilon_y)^2 + {\gamma_{xy}}^2\right)^{-0.5}\gamma_{xy} \qquad (5.27)$$

5.3 Mesh Objectivity

As shown previously in this chapter, attempts have been made by other researchers to simulate ECC with the finite element method. They have however not investigated the final material softening in depth and no author has shown mesh-independence for their numerical models.

Kabele (2000) used a method similar to the crack band model of Bazant and Oh (1983) to relate the crack opening displacement of the localising crack to strain by using a crack band width. The crack band width is dependant on the element size and the angle of the crack in the element. The choice of the crack band width was used to ensure that the correct amount of energy will be dissipated regardless of the mesh size. However, no analyses were presented that showed the independence of mesh size. The author believes that the model of Kabele (2000) is mesh dependant.

Not much detail was given to the final localising of the material in Han et al (2003). An ultimate strain was simply chosen for the final point of localisation, i.e. where the material resistance in tension becomes zero. No method for determining the ultimate strain was proposed and it is uncertain how the values can be attained. This model will result in strong mesh dependence as no material length scale was introduced.

The constitutive law for the softening in the model of Simone et al (2003) was formulated as a displacement based crack opening relation. The crack opening for the complete force transfer loss was taken as half the fibre length. The mesh dependence of this model was not reported.

The problem of mesh-bias has thus not been addressed for strain hardening type materials such as ECC and deficiencies still exist when modelling the softening of ECC.

The basis of the problem of mesh-biased numerical models of concrete is that the energy dissipation corresponding to crack growth and widening is mesh dependant if it is not addressed appropriately. For correcting this mesh-dependency, the crack band model works well for ordinary concrete as the energy associated is related to the constitutive law by means of a crack band width which is normally a function of the element size and the angle of the crack crossing the element. This ensures that the correct amount of energy is dissipated when the material localises.

For this method to work, the boundary conditions should assure that only one row of elements goes into localisation. This is often the case for brittle and quasi-brittle materials, e.g. concrete. For the case of ECC of which the softening branch of the tensile material response has orders of magnitude more energy dissipation compared to ordinary concrete, the situation is quite different. The higher energy dissipation can cause a large area of elements to soften while global hardening is still achieved before only a single row of elements will soften to cause global softening. This will result in every element in this region to dissipate the energy related to a single crack, thus the more elements in this region, the more localising cracks, thus a higher global energy dissipation, which would result in a mesh-dependence.

The existence of a region that undergoes local softening before global softening will be demonstrated by means of an analytical example of a three point bending test. For this, it must be shown that the moment at a section away from the middle section which has the maximum bending moment, is big enough to cause softening in that section. To illustrate this, the boundary conditions of the three point bending setup are shown in Figure 5.6 a) with the bending moment distribution in Figure 5.6 b). The formulation for M_y is:

$$M_y = M_m \left(1 - \frac{2y}{L}\right) \qquad (5.28)$$

shown in Equation 5.28 with M_m the moment at the midspan.

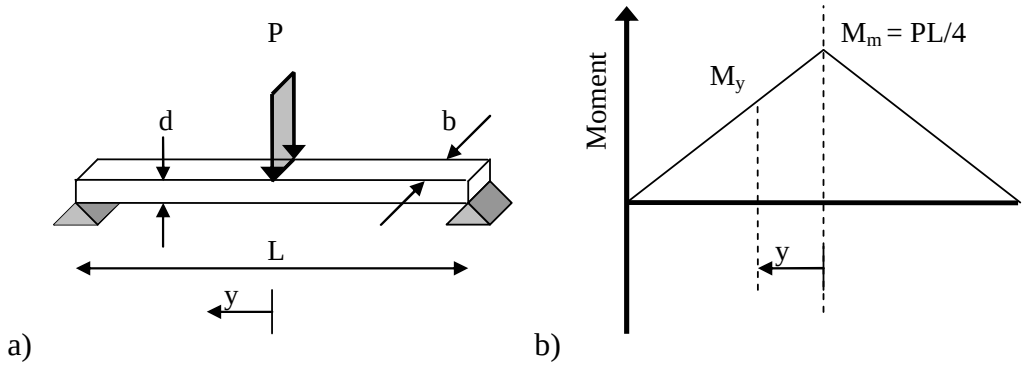

Figure 5.6 a) Three point bending illustration. b) Bending moment distribution.

For this example, the compressive behaviour is assumed to have no limit as the tensile behaviour is believed to cause global softening. The moment will be calculated from the point where material softening is about to start and the neutral axis of the beam is almost at the uppermost position in the beam. As the neutral axis is believed not to move significantly from this position, an assumption is made that the neutral axis is at the top of the beam section. This is done to simplify the mathematical derivation. This simplification is justified as the purpose of the example is only to show that material softening can occur away from the centre of the beam before the onset of global softening.

When looking at a section of the beam and assuming that a flat cross section remains flat and perpendicular to the beam centroid axis, the strain distribution is taken as linear as shown in Figure 5.7 a) with ε_x as:

$$\varepsilon_x = k\,x \qquad (5.29)$$

The tensile constitutive behaviour is shown in Figure 5.7 b) with σ defined as:

$$\sigma = \frac{\sigma_u - \sigma_{fc}}{\varepsilon_{sh}} k\,x + \sigma_{fc} \qquad for\ 0 \le x \le \frac{\varepsilon_{sh}}{k} \qquad (5.30)$$

$$\sigma = -\frac{\sigma_u}{\varepsilon_{tu} - \varepsilon_{sh}} k\,x + \frac{\sigma_u \varepsilon_{tu}}{\varepsilon_{tu} - \varepsilon_{sh}} \qquad for\ \frac{\varepsilon_{sh}}{k} < x \le \frac{\varepsilon_{tu}}{k} \qquad (5.31)$$

and ε_x replaced using Equation 5.29.

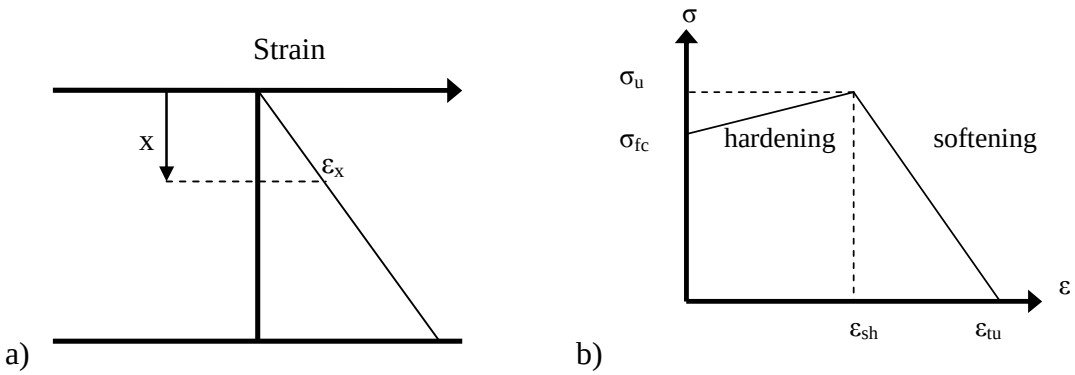

Figure 5.7 a) The strain distribution. b) The constitutive tensile behaviour.

The moment resistance of a section can be calculated as follows:

$$M = \int_A \sigma(x) x \, dA \qquad (5.32)$$

Using Equations 5.30 and 5.31, the moment resistance of a section with a constant width b can be derived for two cases. Firstly the case where no softening has occurred in the section as shown in Figure 5.8 a) and the second, material softening has started as in Figure 5.8 b). The moments for the two cases are derived as follow:

$$\frac{M_1}{b} = \frac{\sigma_u - \sigma_{fc}}{3\varepsilon_{sh}} k d^3 + 0.5 \sigma_{fc} d^2 \qquad (5.33)$$

$$\frac{M_2}{b} = \frac{\varepsilon_{sh}^2}{6k^2}\left(\sigma_{fc} + 2\sigma_u\right) - \frac{\sigma_u k}{3(\varepsilon_{tu} - \varepsilon_{sh})}\left(d^3 - \frac{\varepsilon_{sh}^3}{k^3}\right) + \frac{\sigma_u \varepsilon_{tu}}{2(\varepsilon_{tu} - \varepsilon_{sh})}\left(d^2 - \frac{\varepsilon_{sh}^2}{k^2}\right) \qquad (5.34)$$

x_l is the position where softening starts, expressed as:

$$x_l = \frac{\varepsilon_{sh}}{k} \qquad (5.35)$$

and shown in Figure 5.8 b).

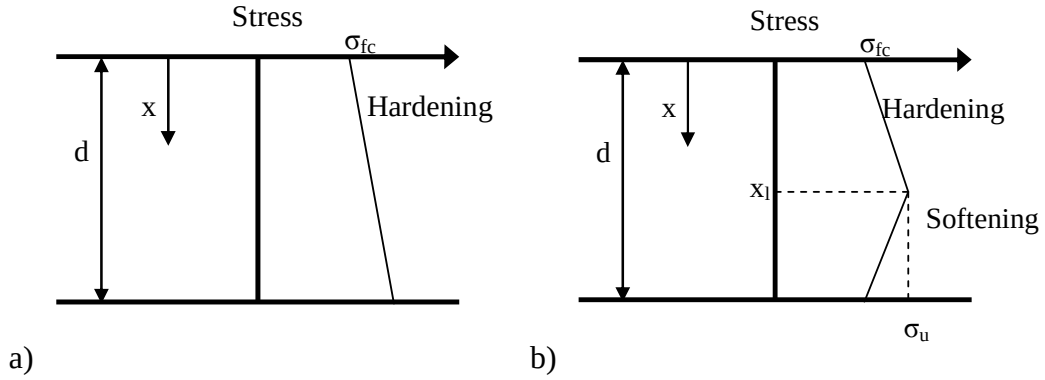

Figure 5.8 a) The stress distribution in a section with no softening. b) The stress distribution in a section after the onset of softening.

The maximum moment resistance for the first case is when the strain at the bottom edge becomes ε_{sh}, i.e. $k = \varepsilon_{sh}/d$. This moment is called the M_{sh}, and expressed as:

$$M_{sh} = \frac{1}{6} d^2 \left(2\sigma_u + \sigma_{fc}\right) b \qquad (5.36)$$

To calculate the maximum moment resistance if the material is softening, the derivative of Equation 5.34 with regard to k is required. The value of k for which the derivative is zero is:

$$k^3 = \frac{\varepsilon_{sh}\left(\varepsilon_{sh}\sigma_{fc} - \varepsilon_{tu}\sigma_{fc} + \varepsilon_{tu}\sigma_u\right)}{\sigma_u d^3} \qquad (5.37)$$

Upon substitution of Equation 5.37 to Equation 5.34 into find the maximum moment, called M_{max}, it can be shown mathematically that for the following conditions:

$$\varepsilon_{tu} > \varepsilon_{sh} \qquad (5.38)$$

$$k > \frac{\varepsilon_{sh}}{d} \qquad (5.39)$$

$$d, \varepsilon_{sh}, \varepsilon_{tu}, \sigma_{fc}, \sigma_u, b > 0 \qquad (5.40)$$

$$\sigma_{fc} \leq \sigma_u \qquad (5.41)$$

the value of M_{max} is always larger than M_{sh}. This has the effect that when material softening occurs in this example, the global response of the beam will still show hardening. A region of the material will go into softening before global softening will occur. The size of the region on the bottom edge of the beam can be found by calculating y in Equation 5.28 with $M_y = M_{sh}$ and $M_m = M_{max}$.

Concluding this example, one can say that there are two phases of softening. The first phase is when the material starts to soften, but the global response is still showing hardening. This softening is spread out over a region at the bottom of the beam. Physically, numerous cracks will start softening. This phase is named regional softening.

The next phase is when the global behaviour starts showing softening and localisation takes place, i.e. a single crack widens while the other cracks which have already started to soften, will unload. This phase is named localised softening.

These two phases are shown graphically in Figure 5.9.

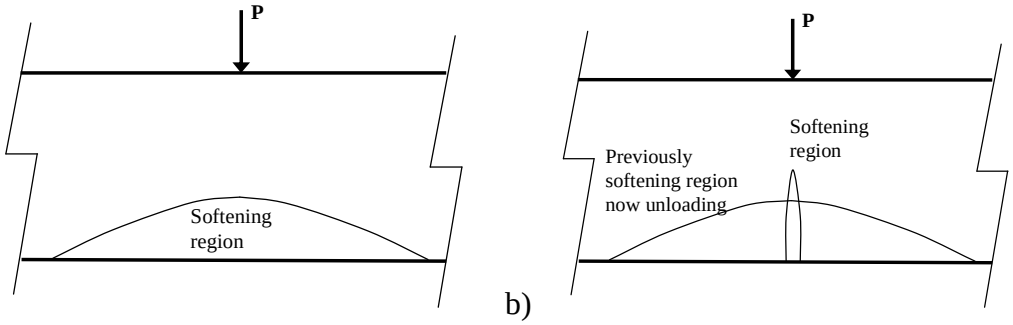

Figure 5.9 The two phases of softening. a) Regional softening. b) Localised softening.

When using the finite element method to compute the global response numerically, ε_{tu}, shown in Figure 5.2 and 5.7 b), would have to be defined for every element while assuring mesh-independence. Elements undergoing the different phases of softening would need different definitions of ε_{tu}. The softening is physically not defined by a strain as in the case of Figure 5.2 and 5.7 b), but as a crack opening displacement over which the softening occurs. The softening is simplified by a linear relation to the crack opening, shown in Figure 5.10 with the softening length defined as L_s.

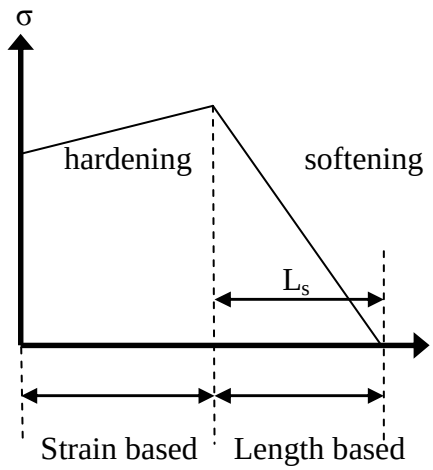

Figure 5.10 Length based softening criteria

For the second phase, localised softening, only one crack widens while the rest are unloading and it is localised to a single row of elements. This requires that ε_{tu} is defined so that the correct energy is dissipated, i.e. the energy of only one crack. To attain the correct ε_{tu}, L_s would have to be divided by a correct length scale. The length scale, L_e, would be a function of the element size, in this case the square root of the element area:

$$L_e = \sqrt{Element\ \ Area} \qquad (5.42)$$

$\varepsilon_{tu\ LocS}$, the value of ε_{tu} for the case of localised softening, is:

$$\varepsilon_{tu\ LocS} = \varepsilon_{sh} + \frac{L_s}{L_e} \qquad (5.43)$$

This value will ensure the correct energy dissipation during this phase.

This formulation of ε_{tu} will not work for the regional softening phase as the energy dissipation is calculated so that there is only one crack per element. This has the effect that the amount of localising cracks is related to the number of elements, causing a strong mesh-dependence. A different formulation is required for the ε_{tu} during the regional softening phase which is mesh independent. For this another physical material parameter is required, namely the crack spacing, S, i.e. the average

distance between two cracks that can undergo softening during the regional softening phase.

With the crack spacing, the number of cracks that will be localising in an element during regional softening can be calculated and thus insuring the correct energy dissipation. The calculation of $\varepsilon_{tu\ RegS}$ is as follows:

$$\varepsilon_{tu\ RegS} - \varepsilon_{sh} = No\ of\ cracks\ in\ element \times softening\ strain\ for\ a\ single\ crack \quad (5.44)$$

$$\varepsilon_{tu\ RegS} = \varepsilon_{sh} + \frac{L_e}{S}\frac{L_s}{L_e} = \varepsilon_{sh} + \frac{L_s}{S} \quad (5.45)$$

There are now two definitions for ε_{tu} and it would be useful if they can be attributed independently to the correct elements' constitutive laws. However, a large number of elements in an analysis can undergo regional softening and only certain elements could experience localised softening. Also, the elements that would undergo localised softening would first undergo regional softening.

Within the constitutive law of an element it is impossible to determine whether the material is undergoing regional softening or localised softening without a non-local approach. And if it was possible to disguise the different phases, it would still be difficult to change from one softening path to another softening path. This becomes clear with the graphical presentation of Figure 5.11.

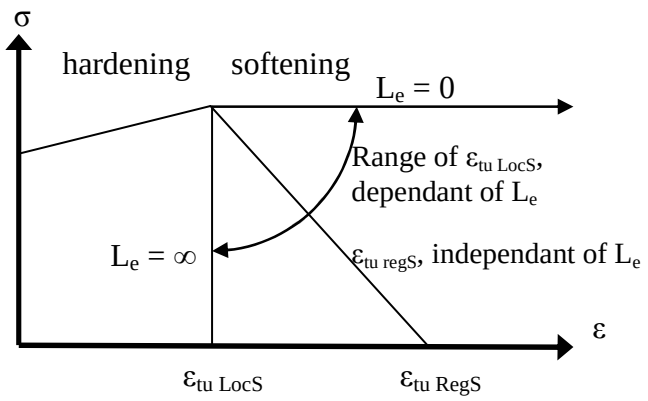

Figure 5.11 The range of the different ε_{tu} with regard to the element size, L_e.

A pragmatic and reliable solution is to ensure that the two definitions of ε_{tu} produce the same results, i.e. the softening lines fall on each other in Figure 5.11 implying that $\varepsilon_{tu\ LocS} = \varepsilon_{tu\ RegS}$. For this to occur, the value of L_e should be the same as S. Thus, the element size should be the same as the crack spacing. Using this approach would ensure that only one crack can localise in an element.

A solution is thus possible which addresses the energy dissipation problem of numerical analyses of ECC during localisation. The solution requires a prescribed element size in the area where regional softening would occur.

A new material parameter, the crack spacing, is now indirectly added to the constitutive law. This value can be determined experimentally from uniaxial tensile tests, as was done in Chapter 3.

5.4 Concluding Summary

In this chapter a constitutive model has been presented that can simulate the mechanical behaviour of ECC numerically. This model is based on a damage mechanics approach to model the phenomenological tensile behaviour of ECC.

The importance of a correct equivalent strain definition, which is required for the damage evolution, was shown. The definition was modified to more accurately simulate the bi-axial behaviour of ECC. Further experimental work is however required to find the true bi-axial behaviour before the modelling can be improved further.

The mesh objectivity of this model was also investigated. It was shows that it is not possible to create a mesh-independent model for ECC without using a non-local approach. A solution was found by introducing another material parameter, namely the crack spacing. If the element size is the same as the crack spacing in the region where material softening occurs, the correct energy dissipation is ensured theoretically during localising.

CHAPTER 6

Constitutive Model Verification

The constitutive model derived in Chapter 5 has to be verified to show that the model can simulate the mechanical behaviour of ECC accurately. The constitutive model was implemented in Diana version 8 using the "User Supplied Subroutine" option. The model verification was done by comparing analysis results with experimental results.

Normally, two types of experimental tests are required for verification. Firstly, a set of tests are done to derive the material model parameters and secondly, a different type of experimental test is performed which represents a structural application, for instance a beam under flexural loading. The results of the simulation of the structural test are compared to the experimental response.

In this chapter, the material model parameters were taken from the tensile tests reported in Chapter 3 and finite element analyses of the flexural tests also reported in Chapter 3 were performed and compared. As a second verification, the shear prediction was investigated by doing a simulation of the Iosipescu shear tests performed by Shang (2006).

6.1 Flexural Test Simulation

Finite element analyses of the flexural tests reported in Chapter 3 were performed. For the constitutive model to be verified, analyses of the flexural tests using parameters derived from the tensile tests of Chapter 3 should simulate the experimental results of the tests accurately. Due to the variation of the tensile results as well as the effect on

the parameters due to a change in strain rate, a parameter sensitivity study is required on the tensile parameters. Lastly, an investigation is done of the effect of fibre alignment in the flexural test specimens.

6.1.1 Model description

The flexural tests were modelled using linearly interpolated, four node plane stress elements. The finite element mesh is refined towards the middle of the beam with the size of the elements in the expected softening and localisation zone 1.33 mm x 1.33 mm. This dimension of the elements in the localisation zone is required to correlate with the crack spacing as explained in Chapter 5. The average crack spacing was found to range between 1.2 and 1.5 mm for the tensile tests. This multiple crack spacing is believed to be a material parameter and is assumed to be the same for any set of boundary conditions. The dimensions as well as the chosen mesh with the boundary conditions are shown in Figure 6.1. The plane stress thickness was chosen as 70 mm, corresponding to the width of the beam.

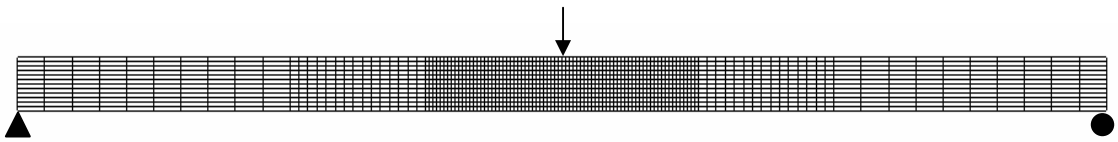

Figure 6.1 The finite element mesh of the flexural test together with the boundary conditions and the applied load.

A slight geometrical flaw was added to break the symmetry of the beam. If the beam was perfectly symmetrical, two final localising cracks will be found as it is not numerically possible for a single crack to occur in the centre of the beam. Two localising cracks do not occur in the experimental results due to the variability and heterogeneity of the material, thus a small geometric imperfection is justified. The geometric flaw was added by moving the node just left of the centre bottom node up by 1 % of the element length, i.e. 0.0133 mm, shown exaggerated in Figure 6.2. This small imperfection will not have a detrimental effect on the results of the analyses.

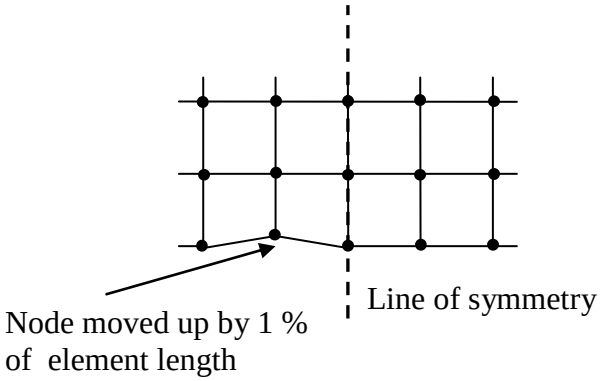

Figure 6.2 Geometric imperfection used to break the symmetry.

The force was applied using a concentrated point load at the centre top node. A force loading was chosen above a prescribed displacement so that an energy based arc length method could be used to solve the non-linear problem. A standard displacement control does not have the ability to trace snap-back behaviour that is possible when localising occurs in the beam. Snap back occurs when the temporarily stored energy induced by the applied load cannot all be absorbed by the localising crack. An example of snap-back is shown in Figure 6.3.

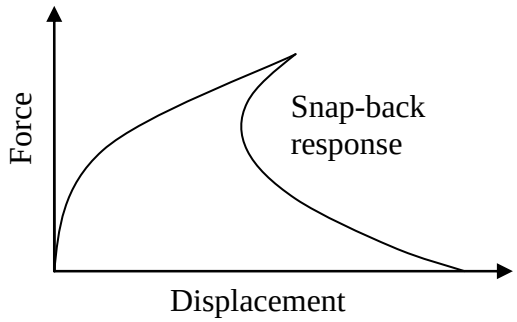

Figure 6.3 An example of snap-back behaviour.

6.1.2 Characterising of material model parameters.

For any constitutive model to produce accurate results, correct material model parameters are required. Parameters required for the developed ECC constitutive model are the material stiffness (E), Poisson's ratio (ν), first cracking strength (σ_{fc}) , ultimate strength (σ_u), tensile ductility (ε_{sh}) , softening length (L_s) as well as the crack spacing (S). The crack spacing is introduced with the element size in the expected softening area as explained in Section 5.3.

A uni-axial tensile test is the best method to attain the material model parameters. The responses shown in Chapter 3 of the tensile tests were, however, variable over the range of strain rates. Normally, material properties are taken from tensile tests done at just one rate of loading. As a first step of verification of the model, the results of the tensile tests done at a normal testing rate will be taken. The next step of the verification would be a parameter study to investigate the effect of the variation of the tensile material model parameters.

A normal testing rate is a testing rate that would take between 2 and 5 minutes to complete. In Chapter 3, the normal testing strain rate for tensile tests is 104 μ/s. The average parameters from these tensile tests as defined in Figure 5.2 are shown in Table 6.1.

Table 6.1 Material model parameters for the verification analysis

E	ν	σ_{fc}	σ_u	ε_{sh}
[MPa]	[-]	[MPa]	[MPa]	[%]
9200	0.35	2.23	2.79	3.90

A softening length, L_s, is also required for the analysis. This parameter cannot be deducted from the tensile tests of Chapter 3, as the displacement of the final localising crack should have been measured. This is not an easy task as the position of the localising crack is not known beforehand. The value of L_s was chosen as 6 mm, half the fibre length. This is a commonly accepted value for L_s (Kabele 2000, Simone et al 2003).

It is required to test if softening only occurred in the area expected, i.e. the area where the element size was chosen as the crack spacing. If localisation occurred in an area outside the prescribed element size, the mesh would have to be refined. In Figure 6.4 the area that underwent softening is shown with a contour plot. It is clear that the softening only occurred in the refined area. This test was done for all analyses reported in this thesis.

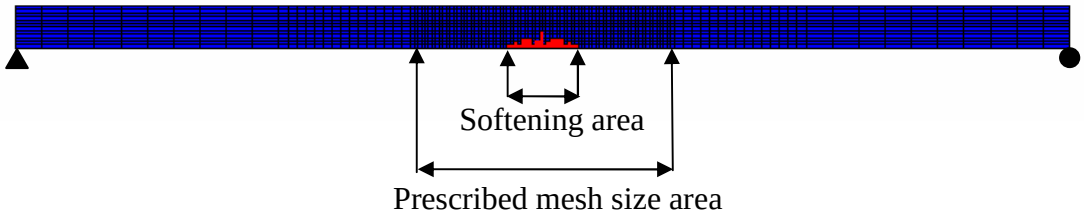

Figure 6.4 The local softening area is shown with red and only occurred inside the prescribed mesh size area.

6.1.3 Analysis results

The result, i.e. the applied force versus the displacement of node on which the load is applied, is plotted together with the experimental results of the normal flexural testing rate in Figure 6.5. The normal testing speed is a deflection rate of 83.3 μm/s.

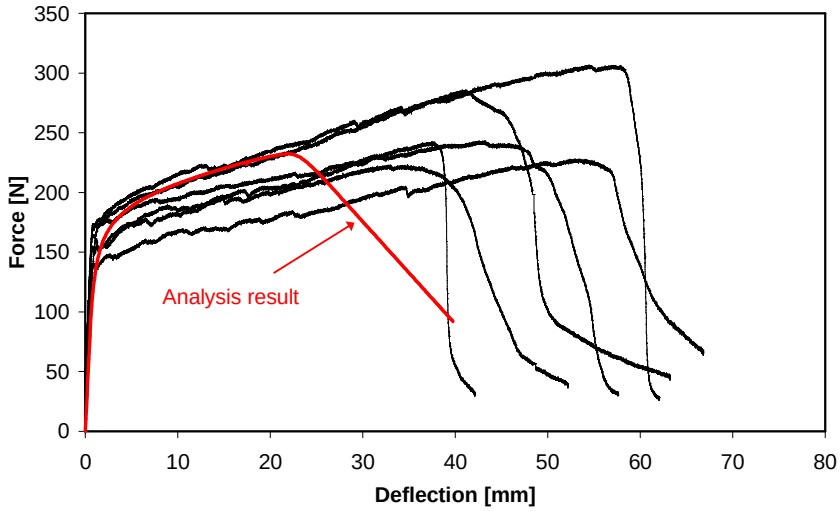

Figure 6.5 The analysis result compared to the experimental flexural results.

It is useful to see the area that is non-linear in the analysis, i.e. the area undergoing damage, as it gives an indication of the failure mechanism. In Figure 6.6 the contours of the equivalent strain are plotted at the point where the maximum load was reached. The equivalent strain is proportional to the level of damage and damage occurs if the equivalent strain is higher than the strain of the first crack, i.e. 242 μm/m in this case. The blue contour thus shows no damage, i.e. $\omega = 0$. It is also important to note that even though this analysis has yet to begin with global softening, local softening is already present, i.e. a equivalent strain of more than 0.039 m/m. In Figure

6.7 the localised crack can be seen during global softening. Due to the geometric flaw in the model, the localised crack occurred to the left of the line of symmetry.

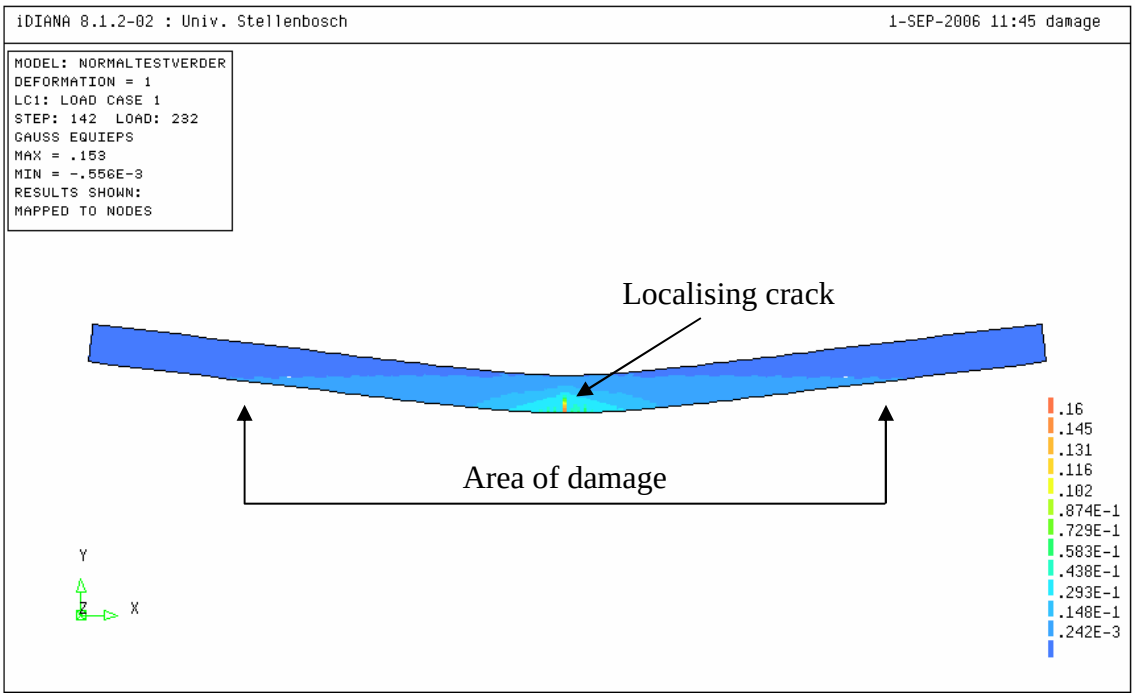

Figure 6.6 The contours of the equivalent strain shown on the deformed shape for the analysis at the maximum force.

If the material model parameters are based on the tensile tests at the normal testing rate, it is shown that the ultimate force is predicted within range, but the ductility is underestimated. The ductility was about half the experimental values. The shape of the response at the early stages of the analysis, i.e. up to 20 mm deflection, corresponds well with the experimental responses.

Many reasons exist why this difference in ductility is found. The most prominent reason is that the parameters taken from the tensile test are not necessarily the true material model properties. The tensile test is subject to certain boundary conditions that could influence the results. This will be investigated with a parameter study. Another aspect that could cause the dissimilarity is an edge effect. The length of the fibres is slightly less than the thickness of the test samples and may cause non-negligible orientation of fibres. These two reasons are investigated and discussed in the following sections.

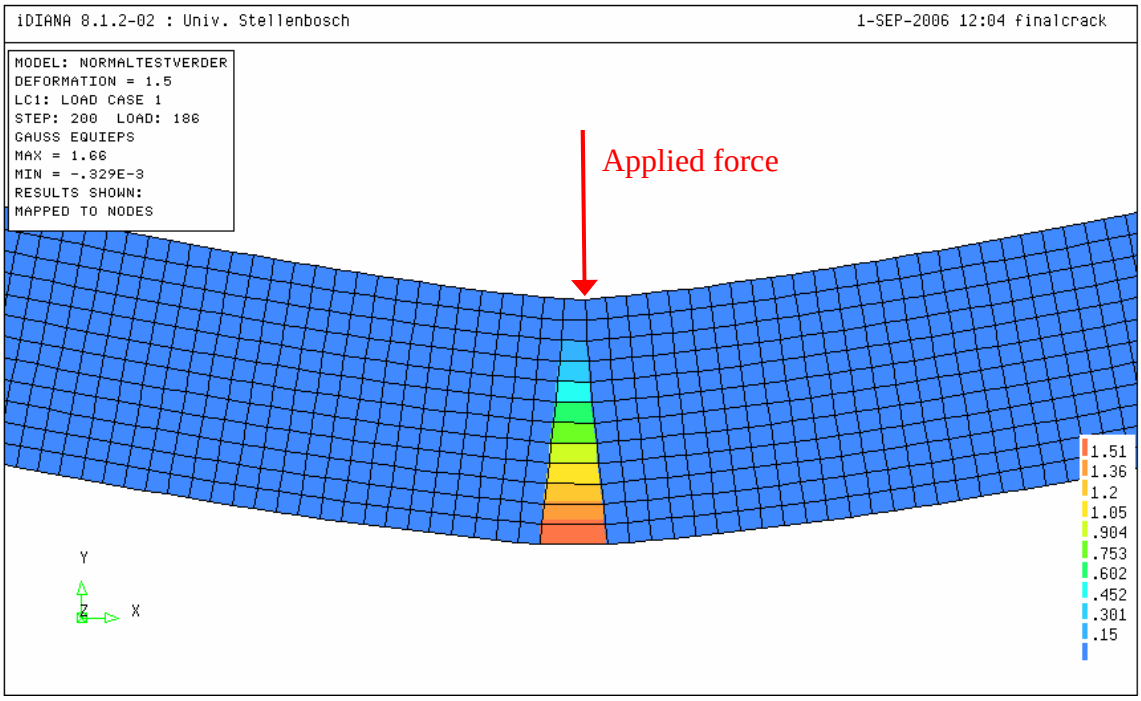

Figure 6.7 The final localisation crack shown. The equivalent strain is plotted on the deformed shape.

6.1.4 Parameter study

The material model parameters used in the analysis in the previous section were based on a set of tensile tests done at one testing rate. It was shown in Chapter 3 that the parameters are dependant on the strain rate, especially the first cracking strength, and also had a significant variation. For this reason, a parameter study will be done to investigate the effect of the different parameters on the analysis results.

The first cracking strength, denoted as σ_{fc}, is the parameter that varies the most with different loading rates and is the first parameter to be investigated. The σ_{fc} value over all the loading rates varied from 1.95 to 4.25 MPa. The high values of σ_{fc} was found when the loading rate started to reach a dynamic strain rate, which is not the case in the flexural test under investigation. A range from 1.95 MPa to 2.4 MPa was chosen for the parameter study on the first cracking strength which represents the lower tensile strain rates. Three analyses were done and the chosen material model parameters are shown in Table 6.2. Note that the analysis called Par2 is the same as the analysis in the previous section.

Table 6.2 Parameters for the parameter study on σ_{fc}.

Name	E	ν	σ_{fc}	σ_u	ε_{sh}	L_s
	[MPa]	[-]	[MPa]	[MPa]	[%]	[mm]
Par1	9200	0.35	1.95	2.79	3.90	6.0
Par2	9200	0.35	2.23	2.79	3.90	6.0
Par3	9200	0.35	2.40	2.79	3.90	6.0

The results of the three analyses are shown in Figure 6.8. A line is drawn that connects the maximum force values of the analyses results. The value of σ_{fc} does not influence the maximum force as much as it influences the ductility of the response. The maximum force reduces slightly with a decrease of σ_{fc}, however, the ductility of the response increases significantly with a decrease of the first cracking strength. The last mentioned phenomenon was expected and proves the postulation made in Chapter 3. The postulation is that a decrease of first cracking strength would cause an increase of the ductility of a flexural test even if the material ductility stayed constant. This phenomenon can be explained when looking at the area of damage, i.e. the area where the cracking threshold was breached. The spread of damage of the three analyses is shown in Figure 6.9. Note that when the first cracking strength is reduced, the area that undergoes multiple cracking increases, and thus an increase in the ductility of the global response is found.

The next parameter that was investigated is the ultimate strength, denoted as σ_u. This parameter did not change as much with the strain rate as σ_{fc} during the tensile rate tests, but did show a slight increase in the higher rate. In Chapter 3 it was shown that these values range from 2.5 to 3.6 MPa. Again, the high values will not be considered as they are at the high rates nearing dynamic rates. A parameter study was done with σ_u ranging from 2.5 to 3.0 MPa with the other parameters staying constant. The parameters of the three analyses are shown in Table 6.3. Note that Par5 has the same parameters as Par2 of Table 6.2.

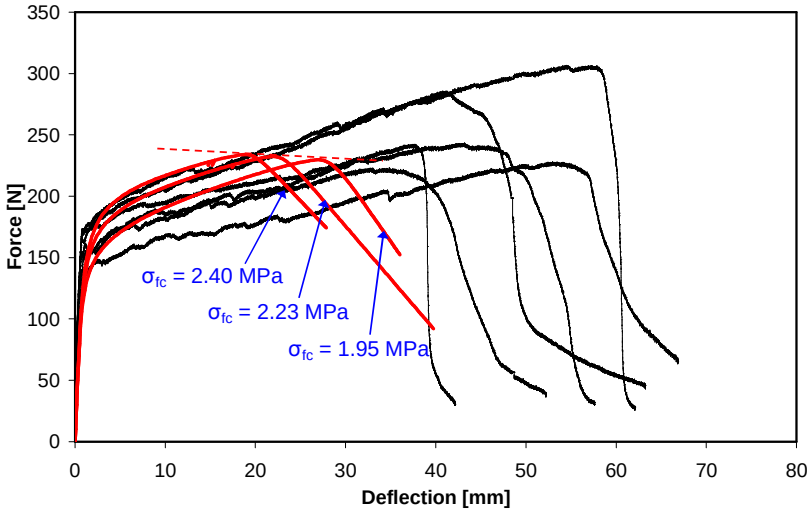

Figure 6.8 The effect of σ_{fc} on the flexural response of the analyses. The analyses are shown with the experimental results.

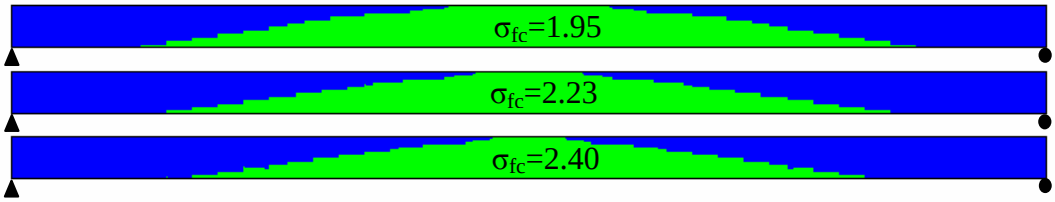

Figure 6.9 The spread of damage of the analyses for the parameter of the of σ_{fc}. The area that underwent damage, i.e. showed multiple cracking, is indicated in green.

Table 6.3 Parameters for the parameter study on σ_u.

Name	E	ν	σ_{fc}	σ_u	ε_{sh}	L_s
	[MPa]	[-]	[MPa]	[MPa]	[%]	[mm]
Par4	9200	0.35	2.23	2.50	3.90	6.0
Par5	9200	0.35	2.23	2.79	3.90	6.0
Par6	9200	0.35	2.23	3.00	3.90	6.0

In Figure 6.10 the results of the parameter study of σ_u are shown. With an increase in σ_u the ultimate strength and the ductility increased. From Par4 to Par5, σ_u increased by 11.6 % and the ultimate force increased by 10 % and from Par4 to Par6, a σ_u increase of 20 % caused a 17 % increase in flexural strength. It is clear that in this range of parameters the ultimate flexural strength is almost directly proportional to the ultimate strength.

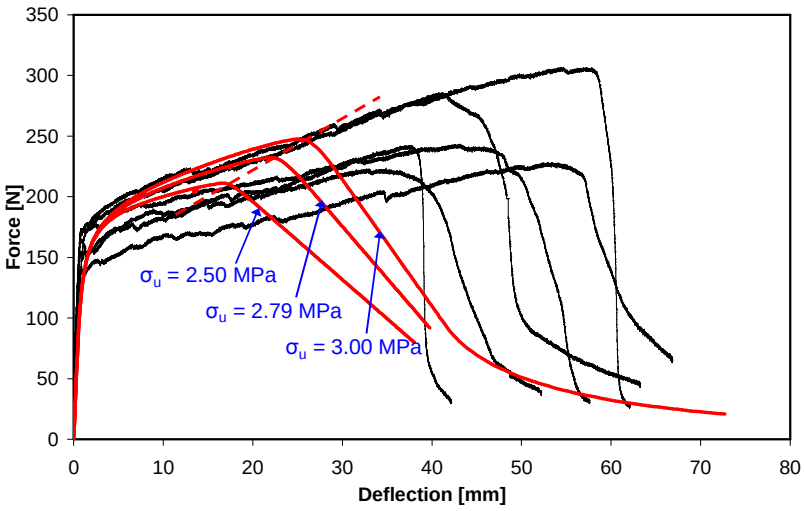

Figure 6.10 The effect of σ_u on the computed flexural response.

The tensile parameter which had the highest variation in the tensile testing was the ε_{sh}, the ductility, and no evidence was found that showed that the ductility changes with an increase of strain rate. The value of ε_{sh} was varied from 3.0 % to 4.8 % which is a representative variation of the ductility found in the tensile tests. The parameters for these analyses are shown in Table 6.4 and the results in Figure 6.11.

Table 6.4 Parameters for the parameter study on ε_{sh}.

Name	E	ν	σ_{fc}	σ_u	ε_{sh}	L_s
	[MPa]	[-]	[MPa]	[MPa]	[%]	[mm]
Par7	9200	0.35	2.23	2.79	3.00	6.0
Par8	9200	0.35	2.23	2.79	3.90	6.0
Par9	9200	0.35	2.23	2.79	4.80	6.0

The variation of ε_{sh} did not have as much influence as σ_{fc} and σ_u, but it is clear that an increase of ε_{sh} does increase the ductility of the flexural response, but has insignificant effect on the ultimate strength of the flexural response.

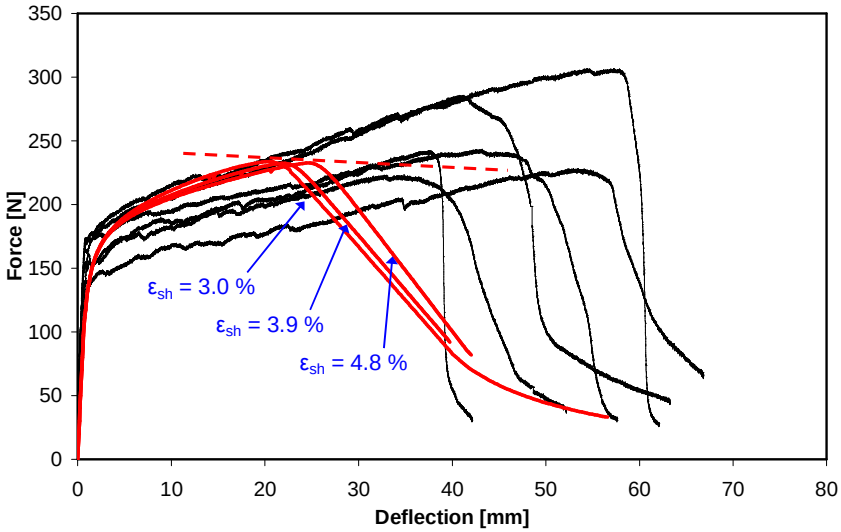

Figure 6.11 The results of the parameter study on ε_{sh}.

A parameter study was also done on the stiffness, E, and Poisson's ratio, ν. The analysis parameters are shown in Table 6.5 and Table 6.6 for E and ν respectively. The results are shown in Figure 6.12 and Figure 6.13. It was found that if the stiffness was lowered, the ductility of the flexural response did increase slightly, but not significantly. The variation in Poisson's ratio also had no significant effect on the results.

Table 6.5 Parameters for the parameter study on E.

Name	E	ν	σ_{fc}	σ_u	ε_{sh}	L_s
	[MPa]	[-]	[MPa]	[MPa]	[%]	[mm]
Par10	8000	0.35	2.23	2.79	3.90	6.0
Par11	9200	0.35	2.23	2.79	3.90	6.0
Par12	10400	0.35	2.23	2.79	3.90	6.0

Table 6.6 Parameters for the parameter study on ν.

Name	E	ν	σ_{fc}	σ_u	ε_{sh}	L_s
	[MPa]	[-]	[MPa]	[MPa]	[%]	[mm]
Par13	9200	0.30	2.23	2.79	3.90	6.0
Par14	9200	0.32	2.23	2.79	3.90	6.0
Par15	9200	0.35	2.23	2.79	3.90	6.0

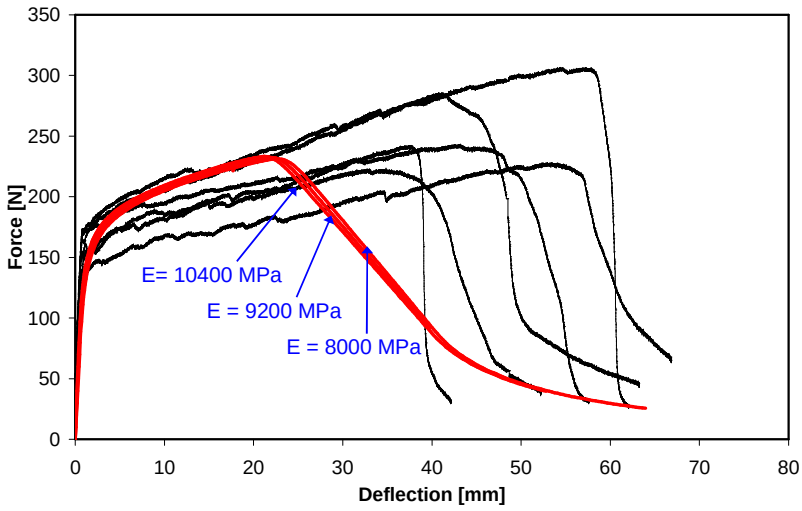

Figure 6.12 The results of the parameters study on E.

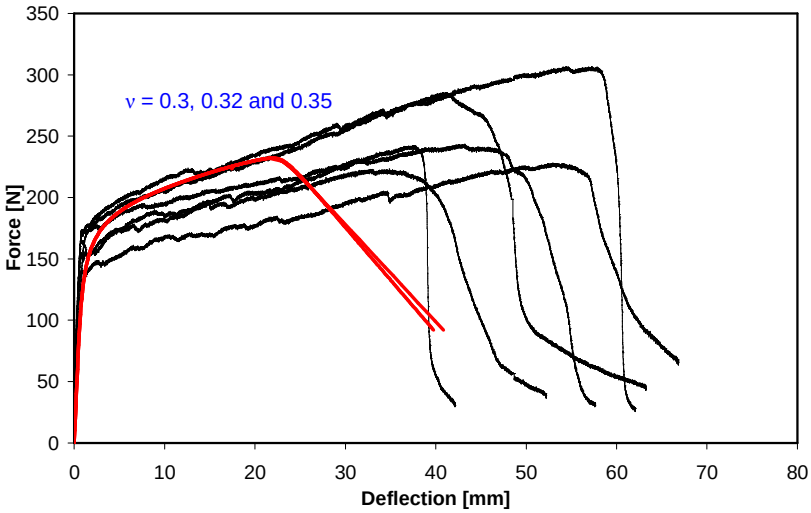

Figure 6.13 The results of the parameters study on ν.

Lastly, a parameter study was done on L_s, the softening length. As indicated in the previous section, the value of L_s cannot be deduced from an ordinary tensile test. The maximum value that L_s can be is 6 mm, as it is restricted by half the maximum fibre length. The value was varied from 4 mm to 6 mm. An L_s less than 6 mm would imply that some of the fibres rupture during the softening process. The analysis parameters are shown in Table 6.7 and the results of the analyses in Figure 6.14.

Table 6.7 Parameters for the parameter study on L_s.

Name	E	ν	σ_{fc}	σ_u	ε_{sh}	L_s
	[MPa]	[-]	[MPa]	[MPa]	[%]	[mm]
Par16	9200	0.35	2.23	2.79	3.90	4.0
Par17	9200	0.35	2.23	2.79	3.90	5.0
Par18	9200	0.35	2.23	2.79	3.90	6.0

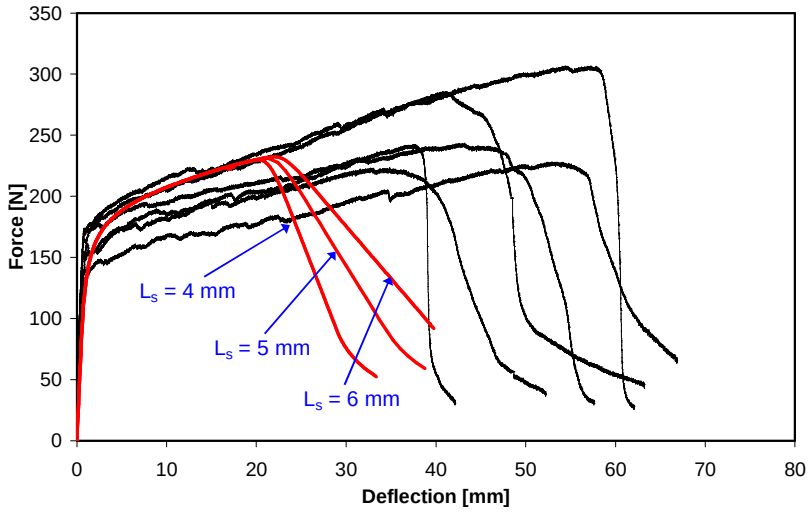

Figure 6.14 Results of the parameters study on L_s.

It is to be expected that the higher L_s values would increase the gradient of the softening branch as can be seen in Figure 6.14. It is also important to note that a higher L_s results in a higher maximum force of the response. This shows clearly that a size effect exists, as L_s is a length scale.

To conclude the parameter study on the tensile parameters, a final analysis is done to show the compounding effect of the different parameters. The parameters are chosen to give the maximum possible ductility, but still be within the range found in the tensile tests. The chosen parameters are shown in Table 6.8 and the result shown in Figure 6.15 together with the original analysis result from the previous section. It is acknowledged that the probability of this combination is low, but it shows how sensitive the analysis is with regards to the material parameters of which a relative large scatter is found experimentally.

Table 6.8 The final analysis to maximise the ductility.

Name	E	ν	σ_{fc}	σ_u	ε_{sh}	L_s
	[MPa]	[-]	[MPa]	[MPa]	[%]	[mm]
Par19	9200	0.35	1.95	3.00	4.80	6.0

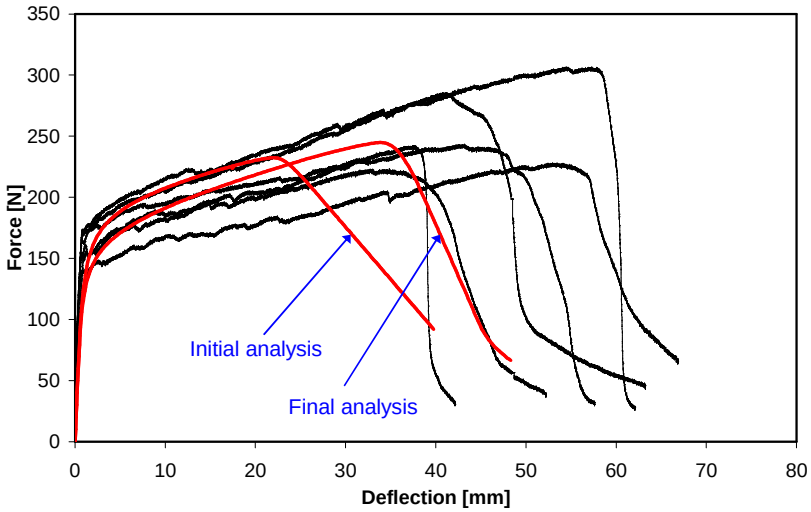

Figure 6.15 The results of the final analyses of the parameter study compared to the results using the initial material model parameters.

6.1.5 Influence of fibre alignment

The fibres in the direct tensile test as done in Chapter 3 are not completely randomly orientated and so also the fibres in the flexural specimens. A representation of the possible fibre orientation is shown in Figure 6.16. Note that the fibres drawn in the figure are rigid, unbendable fibres. PVA fibres are however bendable and the alignment of fibres along the edges will be even more profound as the ends of the fibres would bend to further the alignment.

The tensile strength and the strain hardening capacity in the region of the aligned fibres will increase. For the tensile test, the strain is evenly distributed along the depth of the specimen and an average response, that includes aligned and randomly orientated fibres, would result during the test.

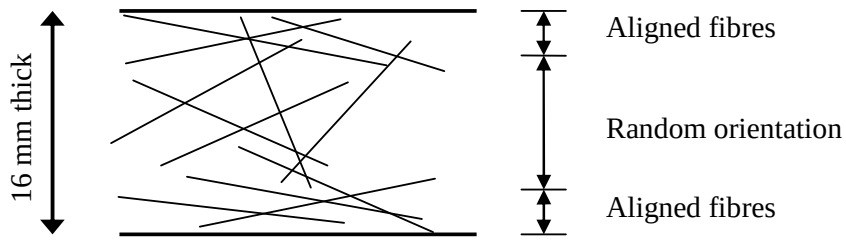

Figure 6.16 Alignment of rigid fibres along the thickness of a specimen.

In the flexural test however, the strain distribution is not equal through the thickness, but has a constant gradient as shown in Figure 6.17. In the region at the bottom of the section, the tensile strain would be the highest. This is also the region of the aligned fibres which results in a higher stress and strain capacity of the material. The capacity of the section could thus be significantly increased.

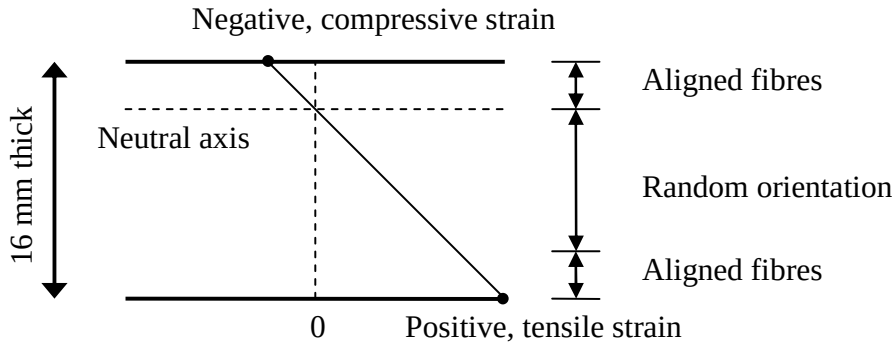

Figure 6.17 The strain distribution in a vertical section of the flexural beam specimen.

To numerically investigate the effect of the aligned fibres on the flexural result, analyses were done in attempt to capture this phenomenon. A beam with the same dimensions and boundary conditions as in the previous sections was modelled, save for the exception that the bottom 3 mm of the beam has different material model parameters. The bottom 3 mm was chosen to represent the area of which the fibres are aligned. The top 3 mm also has aligned fibres, but that area is in compression and the aligned fibres would have no significant effect on the material behaviour. The exact dimensions of the region of aligned fibres are unknown, so an estimate was made. This model description is shown schematically in Figure 6.18.

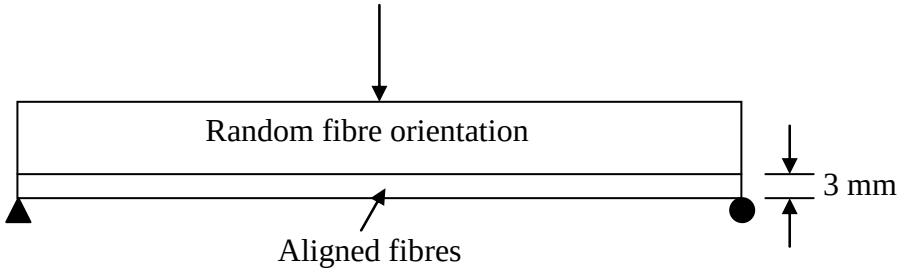

Figure 6.18 The model description that incorporates the area that represents the aligned fibres.

Two analyses, Fibal1 and Fibal2, were done with different material model parameters for the bottom 3 mm of the beam. For both these analyses the normal material model parameters as used for the initial analyses in the previous sections were used. A third analysis, Fibal3, was done using the material model parameters used in the final analysis of the parameter study. The material model parameters of the analyses are summarised in Table 6.9.

Table 6.9 The analyses to investigate the effect of the fibre alignment.

Name	Area	E	ν	σ_{fc}	σ_u	ε_{sh}	L_s
		[MPa]	[-]	[MPa]	[MPa]	[%]	[mm]
Fibal1	Centre and top	9200	0.35	2.23	2.79	3.90	6.0
	Bottom	9200	0.35	2.23	3.1	5.0	6.0
Fibal2	Centre and top	9200	0.35	2.23	2.79	3.90	6.0
	Bottom	9200	0.35	2.23	3.5	6.0	6.0
Fibal3	Centre and top	9200	0.35	1.95	3.0	4.8	6.0
	Bottom	9200	0.35	2.23	3.5	6.0	6.0

The results of the fibre alignment analyses are shown in Figure 6.19. A remarkable improvement was found with Fibal1 and Fibal2, of which only the material model parameters of the bottom 3 mm of the beam analyses were increased. However, with Fibal3, when the parameters of the middle and top areas were adjusted to correspond to the final analyses of the parameter study, a good correlation was found between the experimental results and the numerical results. Note that no attempt was made to quantify the effect of the fibre orientation on the material properties. This requires further experimental investigation. These analyses merely

serve as an example to show the effect that the fibre orientation could have on the analysis result.

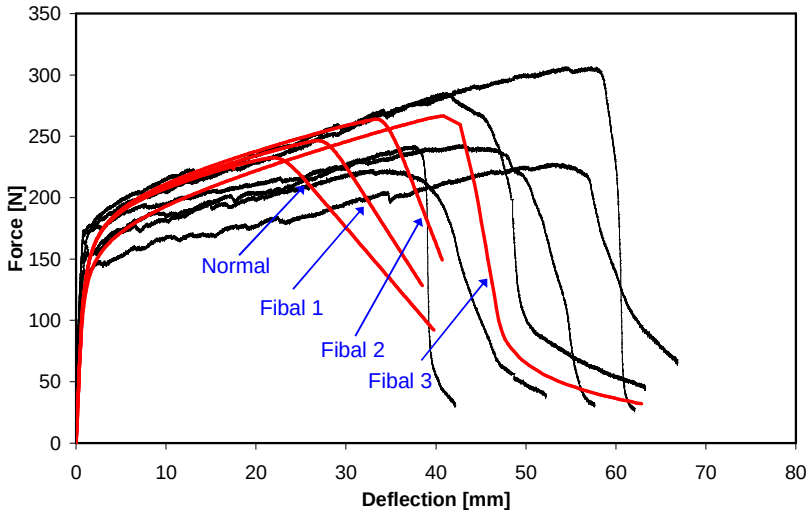

Figure 6.19 The results of the fibre alignment analyses compared to the experimental responses.

6.1.6 Discussion

It is clear from Figure 6.5 that the FEM model and the average parameters of a tensile test performed at a normal strain rate do not predict the flexural response accurately. When analysing a beam in flexure, the ductility was underestimated even though the maximum force was accurate. This underestimation is either due to incorrect material model parameters or as a result of inaccurate assumptions on which the constitutive model is based.

A parameter study was done on the material model parameters. It was shown in Figure 6.15 that the response can be improved by adjusting the material model parameters within the range of the experimental tensile results. The following effects were seen in the response of the flexural analyses during the parameter study:

- A decrease in the first cracking strength, σ_{fc}, showed a strong increase in ductility of the flexural response.
- An increase of the ultimate strength, σ_u, showed a strong increase in both the maximum force and the ductility of the flexural response.
- An increase of the ductility, ε_{sh}, resulted in the increase of the ductility of the flexural response, but does not alter the maximum force.

- A variation of the material stiffness, E, and Poisson's ratio, ν, did not have a significant effect on the flexural response.
- A decrease of the softening length, L_s, had a decrease of the maximum force as result and also a steeper gradient during the global softening.

The alignment of fibres near the edge of the specimens has a significant effect on the results of the flexural response. It was shown in the previous section that if the analyses were adjusted to incorporate the change of material model parameters, it is possible to more accurately simulate the structural response of the flexural beams. The change of the material model parameters was an estimation and further experimental work is required to quantify the effect of the alignment of fibres on the material properties.

6.2 Iosipescu Shear Test

An Iosipescu shear test was designed recently to investigate the shear behaviour of ECC (Shang 2006). The finite element simulation of this test method was chosen as a second verification of the constitutive model developed for ECC as the failure mechanism is predominately Mode II, i.e. shear failure, compared to the flexural tests which showed predominately Mode I failure, i.e. tensile failure.

6.2.1 Introduction to Iosipescu shear test

The shear tests on ECC by Shang (2006) investigated and quantified the shear behaviour and capacity of ECC. The Iosipescu shear test method was developed in the 1960's by Iosipescu (1967) to characterize the shear capacity of metals. This Iosipescu shear test setup was refined by Shang (2006) using linear finite element analyses to ensure the following for an ECC shear test specimen:

- A region should exist that undergoes pure and uniform shear during the linear and non-linear phase of the test.
- A unique relationship should exist between the applied load and the shear stress in order to quantify the shear resistance.
- Failure should occur in the region of pure and uniform shear.

The final design of the Iosipescu shear test specimen is shown in Figure 6.20 and the experimental test setup in Figure 6.21.

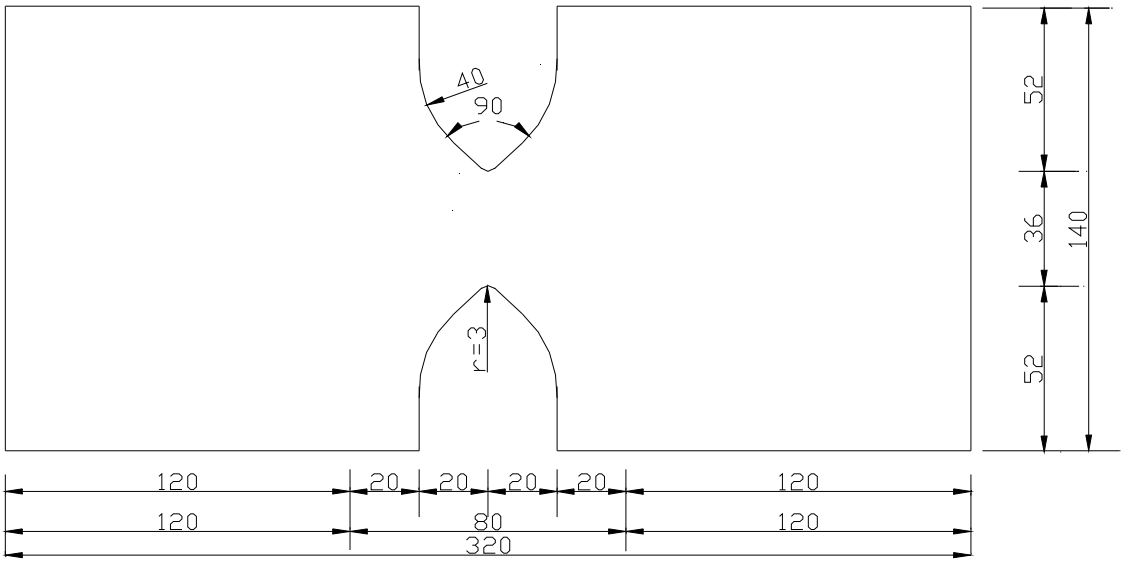

Figure 6.20 The refined Iosipescu shear test specimen for ECC (Shang 2006). All dimensions are in mm.

The expected direction of principal strain is diagonal across the notch area and was measured in the experimental test by means of a displacement measuring instrument, LVDT, over a gauge length of 22 mm as shown in Figure 6.22.

Figure 6.21 Experimental test setup for the Iosipescu shear test (Shang 2006).

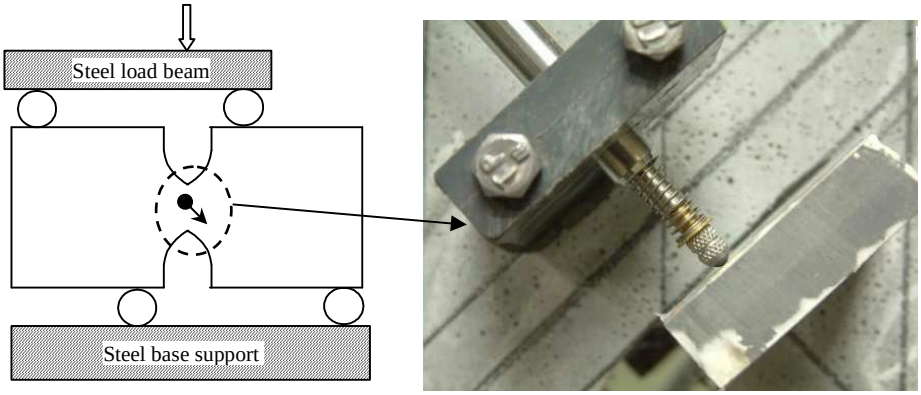

Figure 6.22 The placement of the LVDT to measure the diagonal strain across the notch area with a gauge length of 22 mm.

6.2.2 Finite element model

A finite element model was created to simulate the Iosipescu shear test. Four node, linearly interpolated, plane stress elements were used. The boundary conditions are shown in Figure 6.23. The mesh was refined in the notch area as it is the area where softening is to be expected. The mesh size in the notch area was as close as possible to 1.33 mm x 1.33 mm, as in the case of the flexural analyses in Section 6.1 to capture the softening objectively. The thickness of the plane stress element was chosen as 20 mm as it corresponds to the test specimen's thickness.

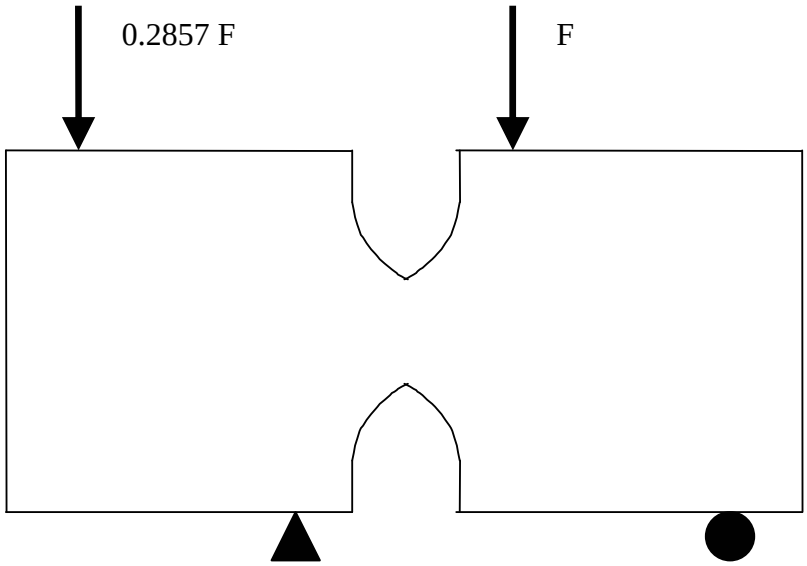

Figure 6.23 The Iosipescu finite element model boundary conditions and the applied force.

The load was applied using two concentrated point load on nodes as shown in Figure 6.23. The correct boundary conditions were ensured by applying the loads in a ratio as shown in Figure 6.23. This ratio is the effect of the equilibrium of the forces acting on the steel loading beam as shown in Figure 6.21 and Figure 6.22.

An energy based arc length solving method was chosen due to the instability of the loading process as small, local snap backs were expected. The material model parameters used are the tensile test parameters derived from tensile tests done by Shang (2006), as summarised in Table 6.10.

Table 6.10 Tensile test parameters for the Iosipescu analysis.

E	ν	σ_{fc}	σ_u	ε_{sh}	L_s
[MPa]	[-]	[MPa]	[MPa]	[%]	[mm]
8520	0.35	1.85	2.92	4.51	6.0

Note that the parameters mentioned in Table 6.10 are based on a single testing strain rate and only three specimens were tested. The average parameters for the three tests were used. The author believes that the parameters do not statistically represent the true material model parameters, but these parameters were used as they are the only parameters available.

6.2.3 Results of shear analysis

The result of the numerical analysis is shown together with the experimental results of Shang (2006) in Figure 6.24. The experimental results shown are the shear stresses of the tests plotted against the strain measured using the diagonal LVDT as shown in Figure 6.22. The shear stress was calculated by dividing the internal shear force at the notch by the notch area to give a uniform distributed shear force representation. This method of calculation was justified by Shang (2006) as he showed that the shear distribution over the notch area is close to uniform. The shear stress of the analysis results was calculated similarly using:

$$\tau = \frac{Internal\ shear\ \ force}{h \times t} = \frac{0.7143\,F}{38 \times 20} \qquad (6.1)$$

with h and t the height and thickness of the notch area respectively. Equation 6.1 is based on the same principle as for the experimental results. The value of F is defined in Figure 6.23. For the strain in the analysis, the distance between two nodes, 22 mm apart at 45 degree angle across the centre point of the notch area is monitored and expressed as an average strain over the a gauge length of 22 mm.

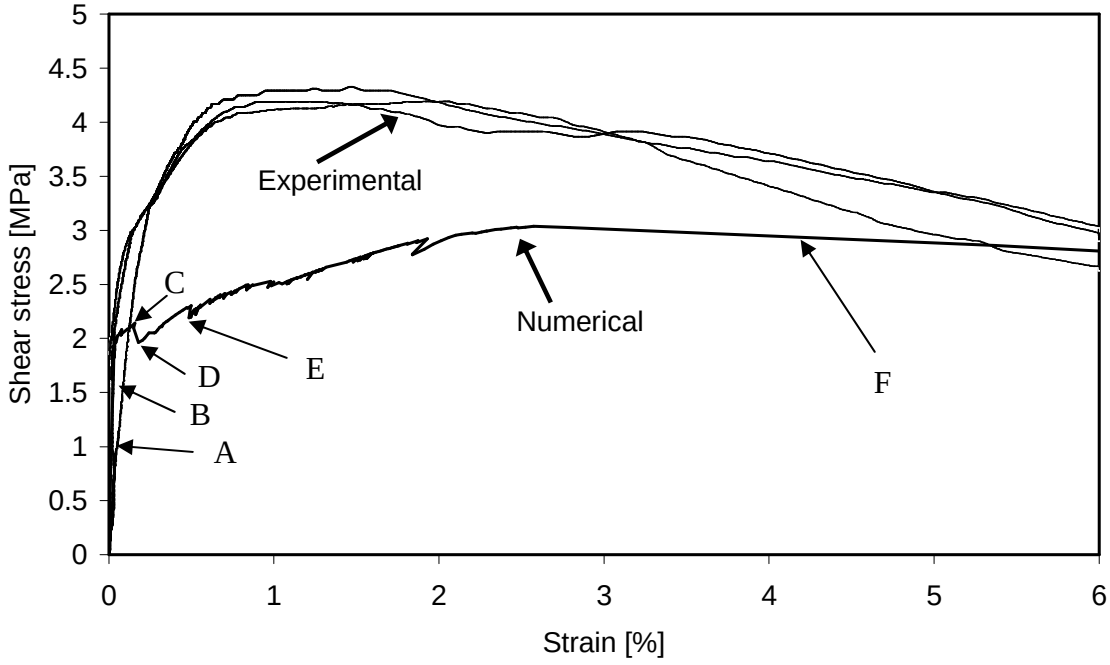

Figure 6.24 The numerical results of the shear test compared to the experimental results from Shang (2006).

The development and spread of damage during the analysis is important as it will give an indication of the failure mechanism. The equivalent strain, as defined in Chapter 6, is shown as contour plots in Figure 6.25 for the different stages of loading as shown in Figure 6.24.

To show that the final localising crack of the analyses corresponds with the final crack of the experimental results, a photo of the localised crack pattern from Shang (2006) is shown in Figure 6.26.

For the comparison of the diagonal (shear) tensile behaviour with the uni-axial tensile test responses that were used for the determination of the analysis parameters, the numerical result is shown together with the tensile test results on Figure 6.27.

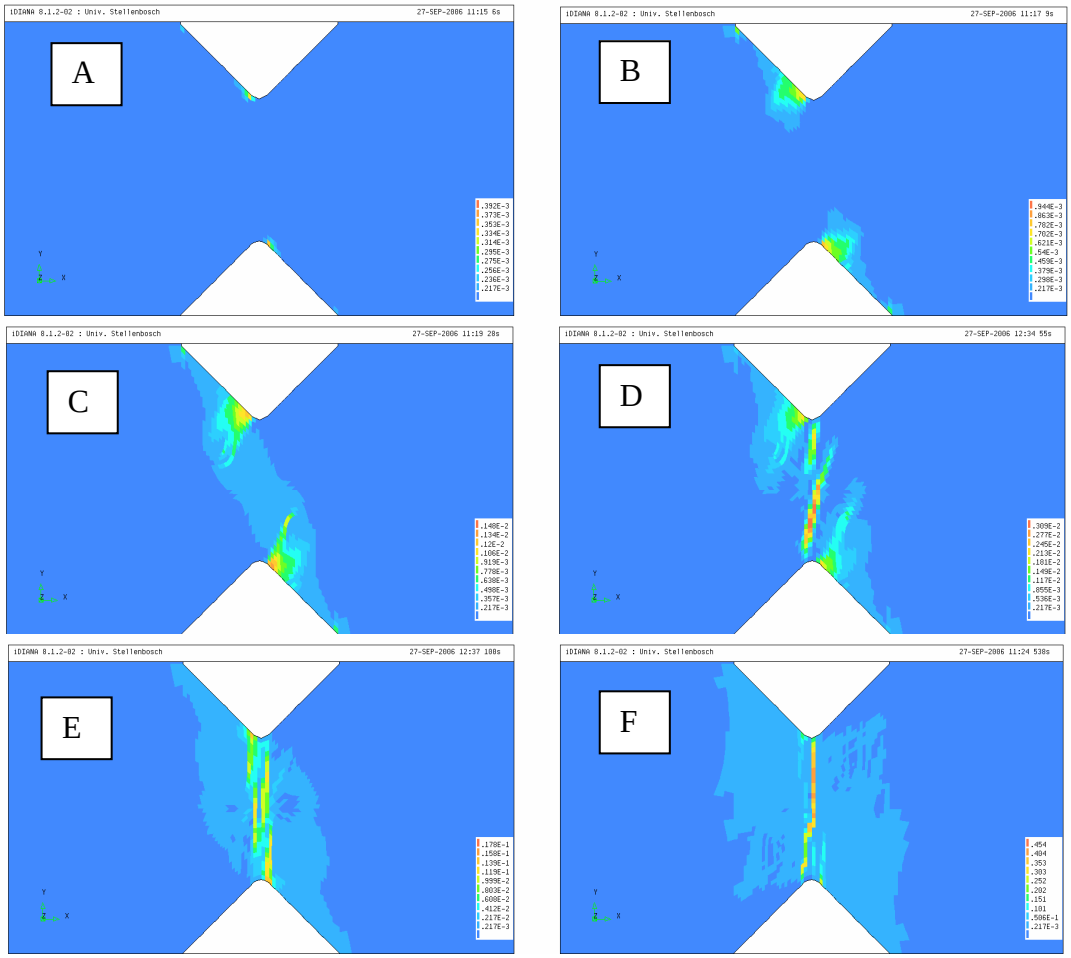

Figure 6.25 The equivalent strain is plotted in the notch area to show the development of damage during the analysis. The corresponding position on the global behaviour is shown in Figure 6.24.

6.2.4 Discussion

The average experimental maximum shear stress found by Shang (2006) was 4.24 MPa in the notch area while the maximum shear stress found in the analysis was 3.03 MPa. This is an underestimation of the shear resistance by 29 %. However, if the computed response is compared to the direct tensile tests from which the tensile parameters have been derived, a good match is found. Due to the equivalent strain definition in Chapter 5, the shear behaviour should have the same diagonal tensile response as the direct tensile response. This is the case as shown in Figure 6.27.

Figure 6.26 The final localising experimental crack pattern from Shang (2006).

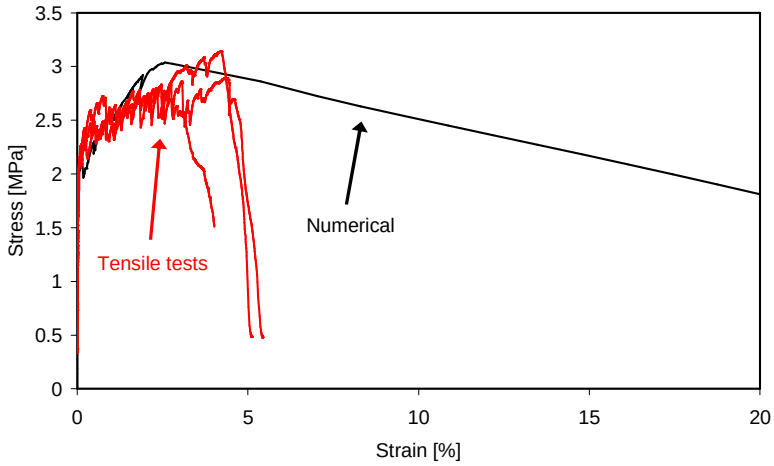

Figure 6.27 The numerical result shown together with the tensile test results from Shang (2006).

An important difference can however be seen in Figure 6.27 in the softening behaviour. The softening of the pure shear is more ductile than the direct tensile results. A reason for this can be explained by means of a schematic representation of the softening mechanism shown in Figure 6.28. For the tensile case only one localising crack occurs and the rest of the material unloads during localisation, however, numerous localising cracks occur which in turn lead to a much more ductile global softening response in the case of pure shear.

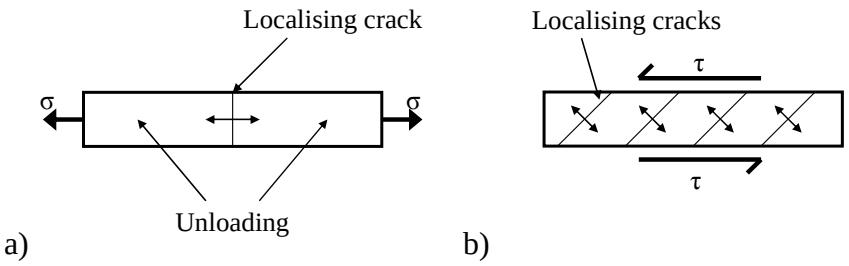

Figure 6.28 a) The localising mechanism in direct tension. b) The localising mechanism in pure shear.

It can be concluded that this model can predict the shear behaviour of ECC, but is conservative by about 30 %. An improvement can be made to the shear behaviour by modifying the equivalent strain definition. For this modification an in depth experimental study is required to characterise the bi-axial loading behaviour of ECC. The pure shear behaviour is only one case of bi-axial loading, thus the Iosipescu tests on their own are not enough for the modification of the equivalent strain for use in finite element analyses of a general shear dominated structural behaviour.

6.3 Concluding summary

In this chapter, verification analyses were done to investigate the accuracy of the constitutive model of ECC presented in Chapter 5. This was done by comparing the results of analyses of flexural and Iosipescu shear tests to experimental results. Secondly, parameter studies were done to investigate the effect of the scatter of the material properties as well as the influence of fibre alignment.

The flexural analyses showed that the model can predict the ultimate strength of a flexural beam, but the ductility was however underestimated. To explore possible reasons for this underestimation, a parameter study was done on the material properties as well as analyses to investigate the possible effect of the orientation of fibres at the edges of the specimen. It was found that a relative large change of the flexural analysis response can be found by changing the tensile material parameters within the scatter of the experimental results. The fibre orientation was shown to potentially have a significant effect on the analyses results. Further experimental work is however required to quantify the effect of the orientation of the fibres.

The analysis of the Iosipescu shear tests showed that the shear behaviour of the constitutive model underestimates the shear behaviour by 29 % for this specific test.

The source of this under prediction can be found in the assumptions of the model with regard to the bi-axial behaviour. An in depth experimental investigation is required to find the true bi-axial behaviour before the model assumptions can be improved.

CHAPTER 7

Modelling the Time-Dependant Behaviour

In this research project, experimental rate tests were done on the macro-level as well as the structural-level. Tensile tests represented the macro-level while the flexural tests represented the structural-level. The flexural test with the specific boundary conditions was chosen as one type of structural application of the material. If the boundary conditions would change, the rate effect found in the structural behaviour would change. A method is thus required to predict the rate-dependant behaviour of a structural element without executing a large number of tests for every type of structural member and boundary conditions.

For the prediction of the time-dependant behaviour of a structural element, different methods are proposed and discussed in this chapter using the constitutive model of ECC presented in Chapter 5. Finally, a time-dependant constitutive model is proposed for most versatile prediction of the response.

7.1 From Macro-level to Structural-level

7.1.1 Scope of prediction

As a first step in the prediction of the structural time-dependant behaviour, the constitutive model will be used with varying material model parameters. The tensile rate tests reported in Chapter 3 show that the strain rate has an effect on the tensile material model properties. A prediction of the rate-dependant behaviour of the flexural tests will be modelled by analysing the beam using the static constitutive model and varying the material properties corresponding to each tensile test strain

rate. The results of the analyses will then be compared to the rate-dependant flexural test results.

This method is based on the assumption that the strain rate throughout the structural test is uniform and stays constant during the test. This is however not the case due to the strain gradient as well as the non-linear behaviour of any structural element of ECC. It can however be said that if the failure mechanism does not change considerably, the strain rate at any material point in the flexural test would be linearly proportional to the deflection rate.

The results of these analyses would not be accurate for the reason of the non-uniform distribution of strain rate, but will be used to investigate the possibilities of this prediction method to identify trends that occur in the rate-dependant responses.

The strain rate of the tensile test must be related to the deflection rate of the flexural test to compare the results and identify trends. The method of linking strain rates used in Chapter 3 to compare the first cracking strength found in the tensile tests to the flexural tests, will be used. The strain rate at the bottom edge of the beam at the middle of the span was related to the deflection rate during elastic bending. This relation, shown in Equation 3.4, was used to compare the results.

For these analyses, the effect of the fibre orientation as discussed in Chapter 6 will not be incorporated as thorough knowledge of this mechanism is still lacking. The prediction of the ductility of the flexural tests is thus expected to be underestimated, as shown in Chapter 6. The trends would however give an indication whether this prediction method is successful.

7.1.2 Static analysis of the rate dependence

The average material model parameters found for each strain rate in the tensile rate tests were used as parameters for the constitutive model. The ultimate strength, σ_u, shown in Figure 7.1, will however be adjusted slightly. The average values at each strain rate do not indicate a clear trend over the strain rates. An increase from the lower rates to the higher rates was however found. To simulate this increase with an increase of the strain rate, a log-linear line is used to represent the trend of σ_u. The expression of this trend line is shown in Figure 7.1 and will be used to calculate the values of σ_u for the analyses.

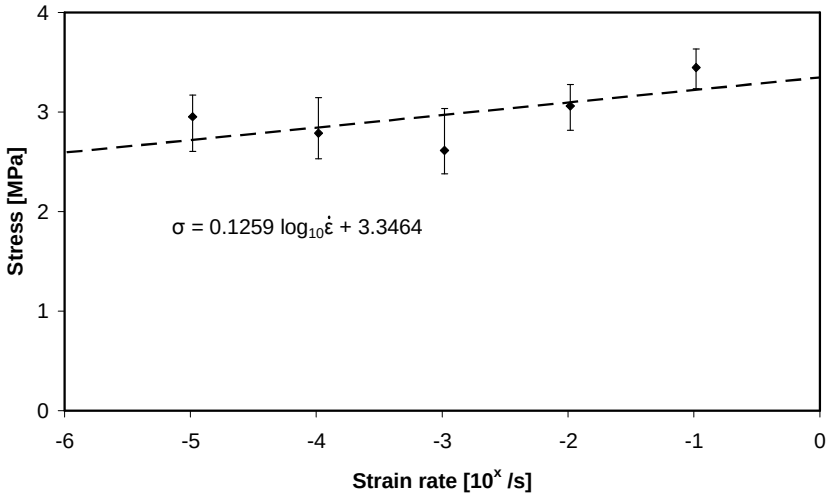

Figure 7.1 The log-linear trend line used to calculate the value of σ_u.

Five analyses were done corresponding to the five strain rates of the tensile tests. The parameters for these analyses are shown in Table 7.1. The tensile strain rate and the corresponding deflection rate as discussed in Section 7.1.1 are also shown in Table 7.1.

Table 7.1 The analyses parameters for the time-dependant analyses of the flexural beams.

Analysis	Strain rate [/s]	Deflection rate [mm/s]	σ_{fc} [MPa]	σ_u [MPa]	ε_{sh} [%]	E [MPa]	ν [ ]	L_s [mm]
Rate1	10.4μ	0.0174	2.13	2.72	4.8	9200	0.35	6
Rate2	104μ	0.174	2.23	2.85	4.8	9200	0.35	6
Rate3	1040μ	1.74	2.38	2.97	4.8	9200	0.35	6
Rate4	0.014	17.4	2.77	3.10	4.8	9200	0.35	6
Rate5	0.104	174	3.95	3.22	4.8	9200	0.35	6

The computed force-deflection responses of these five analyses are shown in Figure 7.2. To compare the results to the rate-dependant flexural tests, the first cracking force, ultimate force and the displacement at the ultimate force are extracted from the responses. The definitions of these three values are the same as in Chapter 3. The calculated values are shown in Figure 7.3 together with the values from the experimental flexural rate tests.

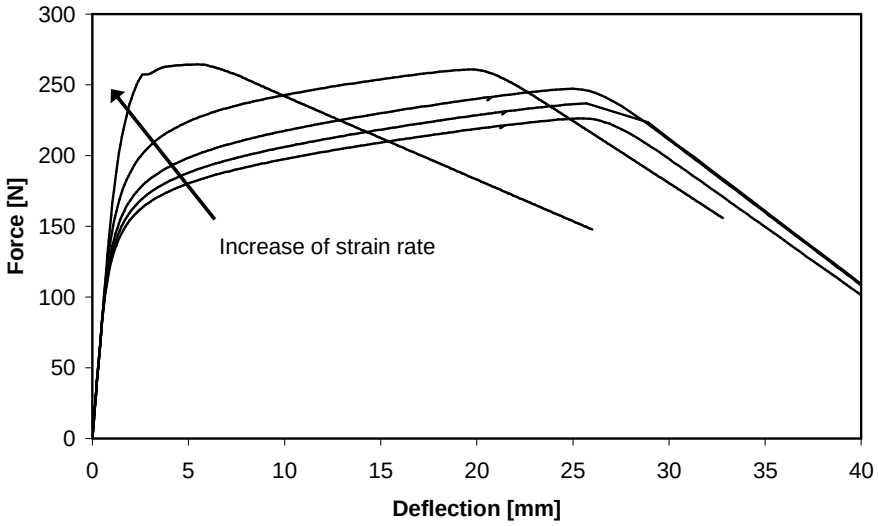

Figure 7.2 The computed responses of the time-dependant flexural behaviour.

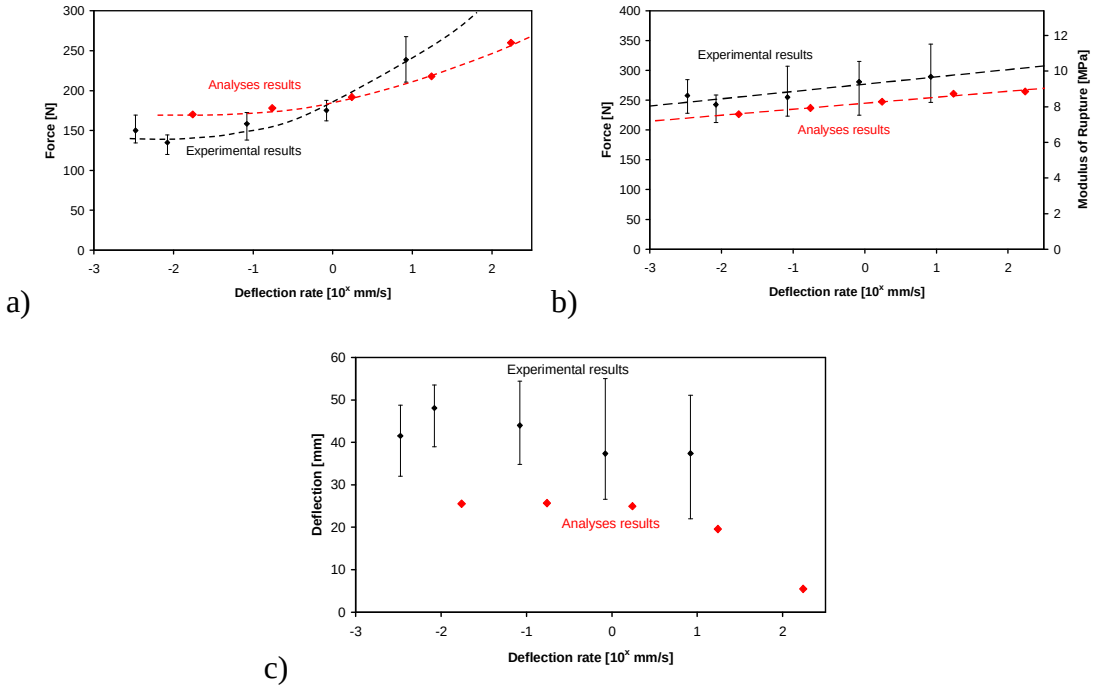

Figure 7.3 The comparison of the flexural rate tests with the prediction of the analyses with a) the first cracking force, b) the ultimate force and c) the deflection at the ultimate force.

A similar trend was found for the values of the first cracking force of the analyses compared to the results of the tests. A strong increase of the first cracking force can be seen in the high rates. The values correspond exactly at a deflection rate of 1 mm/s. The increase of the first cracking force with an increase of rate was however more prominent in the experimental tests, i.e. at high rate the analyses underestimated the force and at lower rates, overestimated the force.

The prediction of the ultimate force was more accurate and the same trend was found for the values of the ultimate force. Both sets of results showed a linear relation of the force to the logarithm of the deflection rate. The analyses underestimated the tested force values by approximately 9 %. The possible reasons for the underestimation are discussed in Chapter 6.

It was shown in Chapter 6 that the value of σ_u predominately influences the ultimate force of a flexural test using the given boundary conditions. If the unadjusted values were used as parameters as shown in Figure 7.1, the results in Figure 7.3 b) would have resulted in the same trend as the average values of σ_u.

The analysis results strongly underestimated the deflection at the ultimate force. The inaccuracy is up to 40 % of the tested values. This was however expected and is mainly ascribed to the fibre orientation in the thin elements and other aspects as described in Chapter 6. The important aspect to investigate is if a correlation could be found between the trends of the two result sets. A reduction of the ductility can be seen at high rates for both sets of results.

7.1.3 Conclusions

This method of predicting the rate-dependant behaviour of a flexural test is reasonably accurate, especially taking into account the assumptions that the strain rate is uniform and the uncertain relation between the strain rate and the deflection rate. The change of the ultimate strength with the deflection rate was predicted well and the first cracking force was reasonably well predicted. The displacement at the ultimate force was however underestimated and no conclusion can be drawn about the trend.

This method could however only predict the short term rate-dependant behaviour. The long term deflections or possible creep fracture cannot be incorporated in this way. In the next section, the long term displacements will be addressed.

7.2 Creep Deflection Prediction

In this section, the long term deflections of a beam in flexure will be computed using a creep limit determined by the constitutive model. The long term tensile properties will be used as parameters for the analyses.

7.2.1 Scope of prediction

The long term deflections will be predicted using the static constitutive model. The long term behaviour of any structural element is important as the time-dependant deflections may exceed the serviceability limit state. In the previous section, the rate-dependant material model parameters were used to predict the rate-dependent flexural behaviour. In this section, the same finite element model will be used, but the material model parameters will be adjusted to represent the long term creep behaviour with aid of the tensile creep tests. This will be used to determine the creep limit of the flexural tests.

Executing creep tests to determine the creep limit is not practical if a creep limit is required for every type of structural element. A numerical method is required that use the creep characteristics of the material to determine the creep limit and the creep fracture limit. This has been done with success for ordinary concrete and masonry (Van Zijl 2000), but no attempt has been made for ECC.

The method proposed here uses the tensile creep characteristics of ECC to determine the long term tensile parameters and will in turn be used to simulate the creep limit. This is an indirect method, but it will explore the possibilities of determining the long term behaviour. No experimental results are available of ECC creep and creep fracture behaviour in flexure, thus the success of this method cannot be verified.

No creep fracture was found during the 8 months of testing the tensile creep of ECC at the highest tested load, which is 80 % of the ultimate tensile force found at a normal testing rate. An assumption must be made at what load level the tensile creep fracture limit is and a sensitivity study on this value will be done to investigate the influence of this assumption. From the tensile creep results of Chapter 4 it was shown that the strain capacity is more during a long term creep test, thus a parameter study will also be performed to investigate the effect of an increase of the tensile strain capacity.

7.2.2 Analyses

The material model parameters for the constitutive model were adjusted to incorporate the long term tensile behaviour of ECC. Firstly, the E-modulus was changed to a long

term E-modulus. This can be done with Equation 4.4 using the creep coefficient, Φ. The value of Φ was estimated to be 9.0 over 30 years for the unsealed specimens, which is worst case scenario and will be used for the purpose of these analyses. This results in a value for long term E-modulus of 920 MPa and is shown schematically in Figure 7.4.

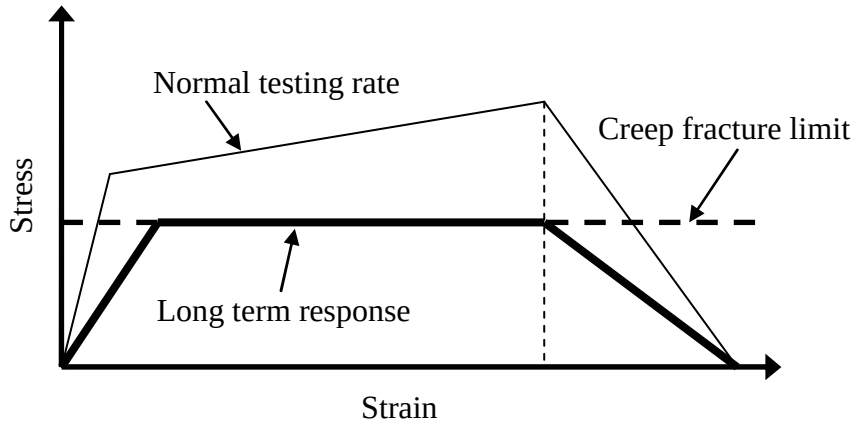

Figure 7.4 The long term tensile material model properties shown graphically together with the original, short term material model properties.

The creep fracture limit for the tensile properties is required to determine the ultimate strength of the material in tension as shown in Figure 7.4. The first cracking strength and the ultimate strength are assumed to be the same for the purpose of the determining the creep limit. As no creep fracture was found during the tensile creep tests after 8 months, a value was assumed. This value was based on the creep results expressed in Figure 4.16. The strain increased in one specimen at a 80 % load to about 5.2 % strain after 8 months. This value is well beyond the average strain capacity, but with no indication of creep fracture. This does however show that the material cannot with stand a load of 80 % over a long period of time within the normal strain capacity range. A value of 70 % is thus chosen to be the creep fracture limit. This value was chosen for the first cracking strength and the ultimate strength. A sensitivity study was also done to show the effect of the choice of the creep fracture limit and will include analyses with the creep fracture ranging from 50 % to 80 %.

The Poisson's ratio, the softening length and the strain capacity were chosen the same as for the short term material model parameters. These values together with the parameters for the sensitivity study of the creep fracture limit are shown in Table 7.2.

Table 7.2 The parameters for the creep limit determination analyses including a parameter study of the creep fracture limit.

Analysis	Chosen creep fracture limit	σ_{fc} [MPa]	σ_u [MPa]	ε_{sh} [%]	E [MPa]	ν [ ]	L_s [mm]
ShortTerm	-	2.23	2.79	4.8	9200	0.35	6
CreepEnv1	50 %	1.35	1.35	4.8	920	0.35	6
CreepEnv2	60 %	1.62	1.62	4.8	920	0.35	6
CreepEnv3	70 %	1.89	1.89	4.8	920	0.35	6
CreepEnv4	80 %	2.16	2.16	4.8	920	0.35	6

The results of the analyses are shown in Figure 7.5 together with the results of an analysis using the short term material model parameters. The influence of the tensile creep fracture limit is shown to be important if the creep limit is to be determined correctly. The influence it has on the flexural strength reduction is expressed in Table 7.3. The tensile creep fracture limit expressed as a percentage of the ultimate short term strength is compared to the percentage of the flexural creep fracture limit over the ultimate short term flexural resistance. It is shown that a larger reduction of the strength is found in the flexural behaviour than the assumed reduction of the tensile stress capacity.

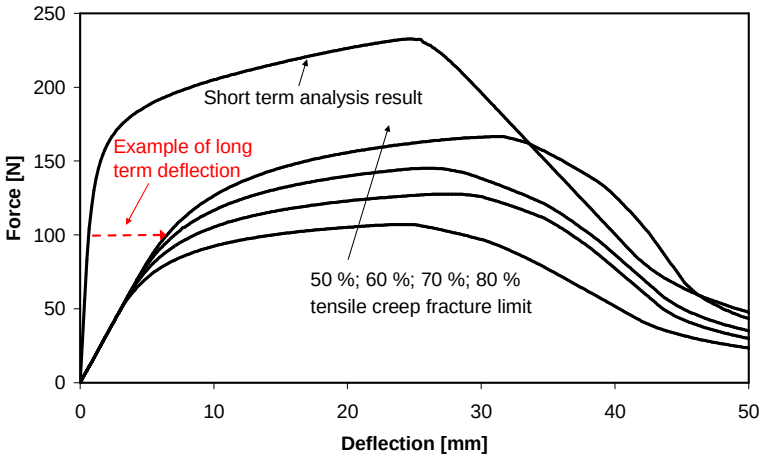

Figure 7.5 Results of the flexural creep limit analyses including a sensitivity study of the tensile creep fracture limit compared to the short term analysis result.

Table 7.3 Comparison of the tensile creep fracture limit and the corresponding flexural creep fracture limit.

Creep fracture limit	
Tensile	Flexural
50 %	46.0 %
60 %	54.9 %
70 %	62.4 %
80 %	71.6 %

To investigate the effect of the increased strain capacity found during the tensile creep tests, the effect of ε_{sh} was investigated. A tensile creep fracture limit of 70 % was chosen for these analyses and the strain capacity was varied from 4.8 % to 6.8 %. The parameters for these analyses are shown in Table 7.4.

Table 7.4 The parameters for the parameters study on the strain capacity.

Analysis	Chosen creep fracture limit	σ_{fc} [MPa]	σ_u [MPa]	ε_{sh} [%]	E [MPa]	ν [ ]	L_s [mm]
CreepEnv3	70 %	1.89	1.89	4.8	920	0.35	6
CreepEnv5	70 %	1.89	1.89	5.8	920	0.35	6
CreepEnv6	70 %	1.89	1.89	6.8	920	0.35	6

The results of these analyses are shown in Figure 7.6. The increase of the strain capacity from 4.8 % to 5.8 % increased the ductility of the long term response, but a further increase of strain capacity had no significant increase.

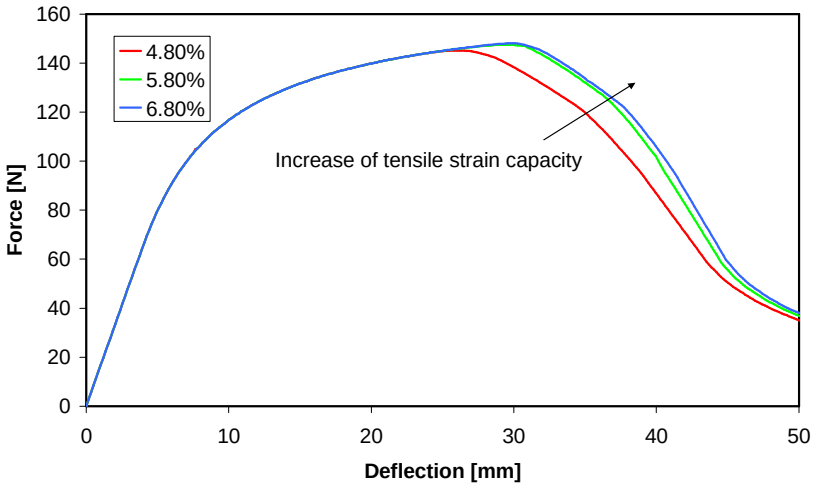

Figure 7.6 The results of the parameter study on the strain capacity.

7.2.3 Conclusions

This method of the creep deflection prediction gives an indication of the long term behaviour of ECC used in a structural sense. There are currently however no long term flexural results available to confirm the prediction. It therefore remains to be verified that a reduction of the tensile stress capacity causes an even bigger reduction in the flexural strength, e.g. a reduction to 70 % of the tensile capacity results in a reduction of the flexural force capacity to 62.4 %.

The large long term deflection that can be expected is alarming and is probably underestimated as the results of Chapter 6 indicate. An example is shown in Figure 7.6 for the calculation of the long term deflection. For a load of 43 % of the short term ultimate strength as shown in Figure 7.6, the short term deflection is estimated at 0.68 mm. However, due to creep the long term deflection is calculated at 6.48 mm if a tensile creep fracture limit of 70 % is chosen. This clearly shows that the long term deflection of any structural element consisting of ECC is an important aspect that requires further study and must be incorporated in the design process.

The method of calculation of the creep fracture limit and creep limit investigated in this section is a pragmatic approach as the constitutive model used is a static model and does not incorporate any time-dependant strains or a rate effect. In the next section an addition is proposed for the static constitutive model that would incorporate the time-dependant behaviour.

7.3 Proposed Constitutive Model for the Time-Dependant Behaviour

In this section, a method is proposed for the incorporation of the time-dependant behaviour in the ECC constitutive model. Firstly, a mathematical model is derived to simulate the creep strain at any time taking into account the stress history. A proposed implementation will be presented to incorporate the mathematical description using associative elasto-plasticity.

7.3.1 Mathematical description of non-linear creep

A mathematical model is required to compute the total creep strain of a material point at any time. The concept of superposition is commonly accepted for creep and for this the load history is taken into account when calculating the creep strain. A formulation is derived that represents the complete stress history over time without having to add a variable for each history point.

The assumption of superposition implies that the total creep strain can be calculated by taking the sum of the creep strains caused by each stress and time increment separately. This is shown schematically for two increments in Figure 7.7.

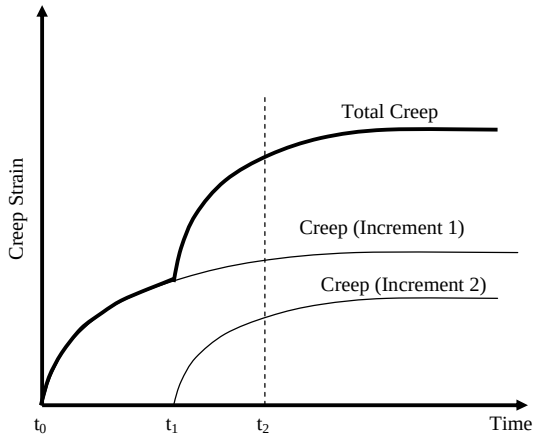

Figure 7.7 Principal of superposition.

The basic shape of creep strain is assumed to be represented by an exponential expression:

$$\varepsilon = \sigma C_1 \left(1 - e^{-C_2 t}\right) \qquad (7.1)$$

C_1 defines the total creep that occurs for 1 stress unit, also know as the creep compliance, C_c, used in Chapter 4, while C_2 defines the rate of creep. This expression, however, cannot represent the typical shape of creep strain over time. A sum of N terms of Equation 7.1 can however give a good estimation of the creep response, each with different values for C_1 and C_2 as follows:

$$\varepsilon = \sigma \sum_{i=1}^{n} \left(C_{i1} \left(1 - e^{-C_{i2} t} \right) \right) \qquad (7.2)$$

For calculating the creep strains for a specific time increment, t_0 to t_1, and stress increment, σ_0 to σ_1, the equation becomes:

$$\varepsilon_1 = (\sigma_1 - \sigma_0) \sum_{i=1}^{n} \left(C_{i1} \varphi \left(1 - e^{-C_{i2} (t_1 - t_0)} \right) \right) \qquad (7.3)$$

This holds true for primary and secondary creep as defined in Chapter 2, which are proportional to the stress. Both will be incorporated together and the characteristic that primary creep is recoverable will be neglected. If tertiary creep is to be incorporated in this formulation, C_1 has to be increased to include the non-linear tertiary creep. For this C_1 is multiplied by a factor, φ, which is introduced to incorporate the non-linearity in this formulation. φ is defined as:

$$\varphi = 1 \quad for \quad \frac{\sigma_1}{\sigma_u} < \eta \qquad (7.4)$$

$$\varphi = 1 - A + A e^{B\left(\frac{\sigma_1}{\sigma_u} - \eta \right)} \quad for \quad \frac{\sigma_1}{\sigma_u} \geq \eta \qquad (7.5)$$

where σ_1 is the current stress, σ_u is the ultimate static stress, η the non-linear creep load ratio, the load ratio at which tertiary creep starts and A and B two constants defining the shape of the non-linearity. In this implementation A and B are the same for each term in the summation. For simplification of the development of the formulation only one term of the summation is used as follows:

$$\varepsilon_1 = (\sigma_1 - \sigma_0) C_1 \varphi \left(1 - e^{-C_2 (t_1 - t_0)} \right) \qquad (7.6)$$

For a next increment, t_1 to t_2, the stress is increased from σ_1 to σ_2. The total creep strain, ε_2, is:

$$\varepsilon_2 = (\sigma_1 - \sigma_0)C_1\varphi_1\left(1 - e^{-C_2(t_2 - t_0)}\right) + (\sigma_2 - \sigma_1)C_1\varphi_2\left(1 - e^{-C_2(t_2 - t_1)}\right) \qquad (7.7)$$

This simplifies to:

$$\varepsilon_2 = e^{-C_2 t_2}\left[(\sigma_0 - \sigma_1)C_1\varphi_1 e^{C_2 t_0} + (\sigma_1 - \sigma_2)C_1\varphi_2 e^{C_2 t_1}\right] + \left[(\sigma_1 - \sigma_0)C_1\varphi_1 + (\sigma_2 - \sigma_1)C_1\varphi_2\right] \qquad (7.8)$$

At a given increment the stress and time at the start and end of the increment is known. The variables of the first term between each set of square brackets of Equation 7.8 are known at the end of the first increment, i.e. t_0 to t_1, while the parameters of second term, i.e. t_1 to t_2, in each set of square brackets are known at the end of the second increment, without needing any information about the previous increments. If another increment is added, a third term would arise with the same property, that is all the parameters of that term are known at the end of that term without needing any information about the previous increments. The equation is simplified to:

$$\varepsilon_2 = e^{-C_2 t_2}\left[H_1 + (\sigma_1 - \sigma_2)C_1\varphi_2 e^{C_2 t_1}\right] + \left[H_2 + (\sigma_2 - \sigma_1)C_1\varphi_2\right] \qquad (7.9)$$

Two new variables are found in Equation 7.9, namely H_1 and H_2. These are two history variables, which encapsulate the stress history. The update of the history variables after the second increment is as follows:

$$H_{1New} = H_1 + (\sigma_1 - \sigma_2)C_1\varphi_2 e^{C_2 t_1} \qquad (7.10)$$

$$H_{2New} = H_2 + (\sigma_2 - \sigma_1)C_1\varphi_2 \qquad (7.11)$$

Thus, a formulation is derived where secondary and tertiary creep can be modelled in a continuum where the applied stress can change with time. This formulation uses only two variables per summation term to represent the stress history. The complete formulation is shown in Equation 7.12.

$$\varepsilon_2 = \sum_{i=1}^{n}\left[e^{-C_2 t_2}\left[H_1 + (\sigma_1 - \sigma_2)C_1\varphi_2 e^{C_2 t_1}\right] + \left[H_2 + (\sigma_2 - \sigma_1)C_1\varphi_2\right]\right] \qquad (7.12)$$

7.3.2 Proposed implementation using elasto-plasticity

Some concepts of elasto-plasticity constitutive models were briefly discussed in Chapter 5. As shown in Figure 5.1, any non-linear strain is permanent. Concrete creep is commonly modelled using visco-elasticity (which implies that all creep strains are recoverable). Elasto-plasticity is a more physical correct model, as the largest percentage of creep is permanent, and will thus be used for this implementation. The basic constitutive relation of elasto-plasticity is:

$$\bar{\sigma} = \bar{\bar{D}}^{e}\left(\bar{\varepsilon}_t - \bar{\varepsilon}_p\right) \qquad (7.13)$$

with the vector ε_t which represents the total strain and ε_p which is the plastic strain vector. The relation combined with the damage formulation is:

$$\bar{\sigma} = (1-\omega)\bar{\bar{D}}^{e}\left(\bar{\varepsilon}_t - \bar{\varepsilon}_p\right) \qquad (7.14)$$

The creep strain after an increment in a numerical analysis is a function of the stress, time and the stress history:

$$\varepsilon_{Creep} = f(\sigma, t, H) \qquad (7.15)$$

as derived in the previous section. For plastic flow to occur, the plastic loading function must become non-negative, i.e. the plastic yielding stress, normally depicted as σ_y, must become less than the current stress. It has been shown that creep occurs even at relative small stresses (Neville 1970) therefore it can be deduced that creep does not have an activation stress level. The activation stress level is thus chosen as zero at the start of loading, but changes due to changes in the load, the time and the stress history, H.

This mathematical formulation derived in the previous section can be used for calculating the yielding criteria for a plastic constitutive implementation. The yield stress for plastic flow is found by solving Equation 7.12 for σ_2, the stress at the end of the increment, which becomes the yield stress, σ_{yt} and σ_{yc} for tension and compression respectively. $\varepsilon_{2,}$ the total creep strain at the end of the increment becomes κ, the plastic strain for 1D. The result is:

$$\sigma_2 = \frac{\kappa - \sum_{i=1}^{n}\left(e^{-C_2 t_1} H_1 + \sigma_1 C_1 \varphi e^{C_2 t_1 - C_2 t_2} + H_2 - \sigma_1 C_1 \varphi\right)}{\sum_{i=1}^{n}\left(C_1 \varphi - C_1 \varphi e^{C_2 t_1 - C_2 t_2}\right)} \qquad (7.16)$$

And the derivative with regard to κ:

$$\frac{\partial \sigma_2}{\partial \kappa} = \frac{1}{\sum_{i=1}^{n}\left(C_1 \varphi - C_1 \varphi e^{C_2 t_1 - C_2 t_2}\right)} \qquad (7.17)$$

To generalize to 2D plane stress, a Rankine yield surface, also known as the maximum principal stress yield criterion is used for the compression and tension zones. The yield surface is shown in Figure 7.8 with σ_1, σ_2 and τ the components of the stress vector in plane stress. The yield function, f, and the potential flow function, g, which are the same in associative plasticity are:

$$f = g = \sqrt{0.5 \bar{\sigma}^T \bar{\bar{P}}_t \bar{\sigma}} - 0.5 \bar{\pi}^T \bar{\sigma} - \sigma_{yt} \qquad (7.18)$$

for tension and:

$$f = g = \sqrt{0.5 \bar{\sigma}^T \bar{\bar{P}}_t \bar{\sigma}} + 0.5 \bar{\pi}^T \bar{\sigma} - \sigma_{yc} \qquad (7.19)$$

for compression with:

$$\kappa = \sqrt{0.5 \bar{\varepsilon}^T \bar{\bar{P}}_t \bar{\varepsilon}} + 0.5 \bar{\pi}^T \bar{\varepsilon} \qquad (7.20)$$

$$\overline{\overline{P}}_T = 0.5\begin{bmatrix} 1 & -1 & 0 \\ -1 & 1 & 0 \\ 0 & 0 & 4 \end{bmatrix} \qquad (7.21)$$

$$\overline{\pi} = \begin{bmatrix} 1 \\ 1 \\ 0 \end{bmatrix} \qquad (7.22)$$

The derivatives with regard to κ are:

$$\frac{\partial g}{\partial \kappa} = -\frac{\partial \sigma_{yt}}{\partial \kappa} \qquad (7.23)$$

$$\frac{\partial g}{\partial \kappa} = -\frac{\partial \sigma_{yc}}{\partial \kappa} \qquad (7.24)$$

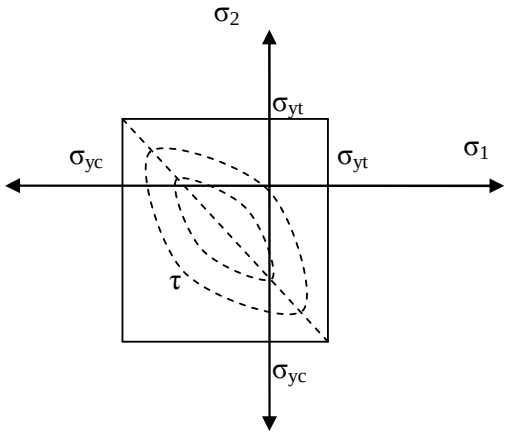

Figure 7.8 Rankine yield surface used for constitutive plasticity.

To simplify the implementation, the assumption of isotropic creep is made. It is, however, possible to distinguish between compressive and tensile creep. Creep can thus occur in compression and tension independently.

7.3.3 Preliminary implementation of the time-dependant constitutive model

A preliminary implementation of this elasto-plasticity model in combination with the damage mechanics approach of Chapter 5 was done using the "User Supplied Subroutine" option of Diana version 8. The implementation of the tertiary creep, i.e. the non-proportional part of creep, was not included. The static parameters used for these analyses are shown in Table 7.5.

Table 7.5 The static parameters for the time-dependant analyses.

σ_{fc} [MPa]	σ_u [MPa]	ε_{sh} [%]	E [MPa]	ν [ ]	L_s [mm]
2.13	2.79	4.8	9200	0.35	6

To find the required parameters for the creep behaviour as described in Equation 7.2, a fit was done to the "sealed" creep response of Figure 4.7. The chosen creep parameters are shown in Table 7.6.

Table 7.6 The chosen creep parameters.

Term no.	C1 [μm/m/MPa]	C2 [/day]
1	430	0.0245
2	11.2	0.1715

Using these parameters, four analyses were done. The rate of loading is specified for each analysis as summarised in Table 7.7.

Table 7.7 The simulated deflection rates for the time-dependant analyses.

Simulated test duration	Deflection rate [mm/day]
Static	Static
1 week	7.14
5 months	0.333
5 years	0.0274

The results of these analyses are shown in Figure 7.9. For these analyses, only the matrix creep is included in the formulation as opposed to the time-dependant fibre pull-out and the time-dependant crack initiation. The matrix creep would influence the first cracking strength of the material considerably, but not the ultimate strength. This is because the creep strain is too small compared to the total strain when the material reaches the ultimate force and no significant reduction is thus seen.

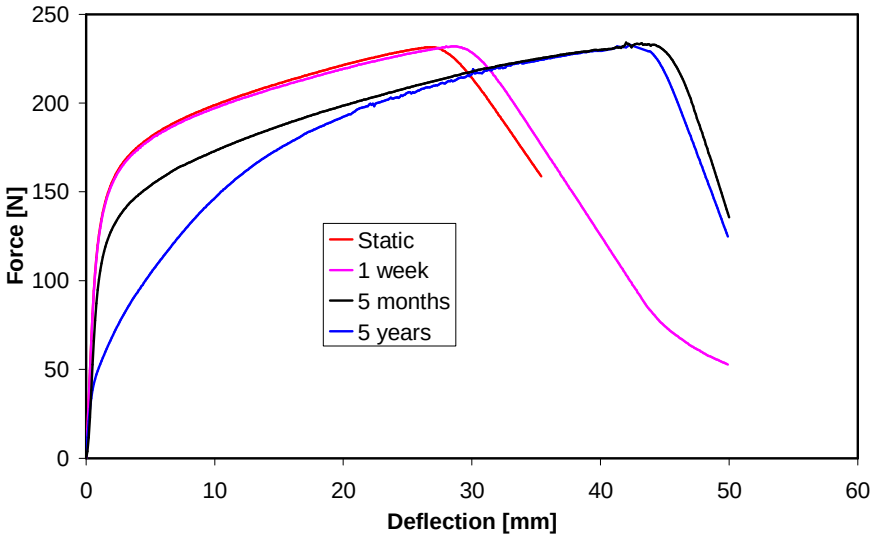

Figure 7.9 The response of the time-dependant analyses.

7.3.4 Concluding remarks

The proposed mathematical description of the creep has the ability to simulate the creep behaviour to include the stress history. The non-linear effect of creep shown in Chapter 2 occurring at high loads can also be included in this formulation.

The implementation using isotropic, associative elasto-plasticity is appropriate for the creep as the creep strains are non-recoverable and creep is shown to be dependant on the stress of the material and plasticity has a stress based failure criterion. With the proposed implementation it is possible for creep to occur in tension and compression independently and different creep parameters can also be specified for tensile and compression.

Even though this method is believed to be more reliable than the previous two methods shown in this chapter, a few aspects would need to be further explored:

- The creep response as defined in the mathematical description and as commonly accepted is dependant on the stress and the stress history. It was

however shown that tensile creep of ECC is also dependant on the strain condition, i.e. if the material is in a condition of higher strain, i.e. more cracks, the creep increases. This has to be further quantified and added to the mathematical description of the creep.

- The damage formulation, which is used to describe the non-linear behaviour of ECC, is based on the strain condition while the plasticity implementation, for the creep, is based on the stress condition. This would result in a lower strength tensile response if the creep strain is added to any analysis. This is shown graphically in Figure 7.10 a). This effect has to be further investigated to establish whether this phenomenon has a physical interpretation.
- A method has to be included to ensure that the first cracking strength is predicted correctly as it is strongly dependant on the strain rate. A method that could ensure the correct cracking strength is to fix the first cracking strain and then, due to the creep strains, the cracking strength would reduce with a lower rate. The effect of this method is shown schematically in Figure 7.10 b). Another method would be to include a crack mouth opening rate as was done by Van Zijl et al (2001) to control the first cracking stress.

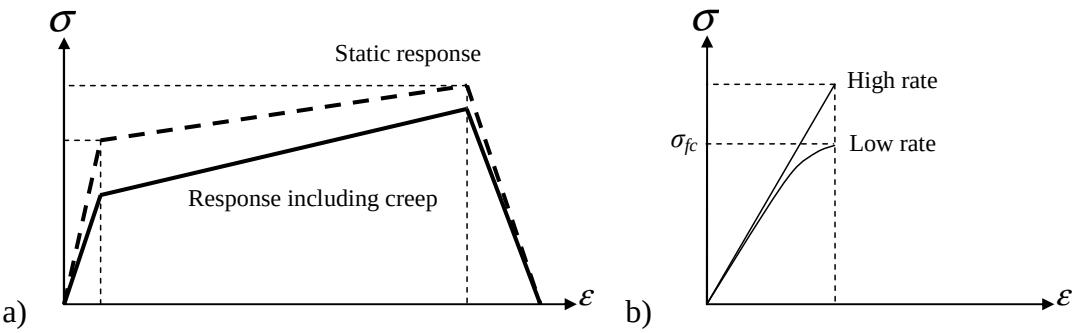

Figure 7.10 a) The response if the plastic creep strains are added to the damage formulation to describe the non-linear behaviour of ECC. b) The method of a fixed tensile strain for the first crack to reduce the first cracking stress at low rates.

7.4 Concluding Summary

In this chapter, three methods of modelling the time-dependant behaviour were investigated. The three methods are the prediction of the rate effect using the rate-dependant material properties, using a creep limit as the material properties and finally, implementing a time-dependant constitutive model.

The first method predicted the rate-dependant behaviour of a beam in flexure by using the rate-dependant tensile properties for the static constitutive model. The parameters were taking from the tensile rate tests of Chapter 3 and the results compared to the rate-dependant flexural tests also reported in Chapter 3. The results compared reasonably well, except for the ductility.

For the second method, a tensile creep limit was used as the material parameters to simulate the long term behaviour of a beam in flexure. The tensile creep limit was chosen after studying the tensile creep test results of Chapter 4. These analyses, which were not verified experimentally, showed that a reduction of up to 40 % of the ultimate resistance can be expected on the long term.

A time-dependant constitutive model was proposed as a final method for the time-dependant modelling of ECC. A mathematical formulation was derived for the description of the creep behaviour, which includes an option for the non-linear behaviour of creep found at high loads. This model was implemented using elasto-plasticity and analyses were done with success. Certain aspects of the time-dependant behaviour were identified which are not included in this formulation. Two examples of these aspects are the ability to correctly predict the first cracking strength as well as the dependency of the magnitude and rate of creep on the strain condition due to the multiple cracking.

CHAPTER 8

Conclusions and Future Prospects

8.1 Conclusions

The main objective of this research project was to investigate and shed light on the fundamental mechanisms causing the time-dependant behaviour of ECC. Together with this, a numerical model had to be created to simulate the static behaviour of ECC and form a basis for the simulation of the time-dependant behaviour.

The sources of the time-dependant behaviour have been successfully identified and investigated on a micro-, macro- and structural-level. The most significant source was found to be the time-dependant fibre pull-out over a crack plane. A numerical model to simulate the static behaviour of ECC was created with success and discussed. Possible sources of inaccuracy were discussed and solutions proposed. The inclusion of the time-dependant behaviour in the constitutive model was demonstrated.

The following significant conclusions can be drawn from the work presented in this dissertation:

8.1.1 Experimental rate tests

- The typical ECC mix investigated shows a strong rate dependence on the first cracking strength in direct tension, i.e. the first cracking strength increases significantly with an increase in strain rate. The rate dependence of the ultimate strength is not as strong while no rate effect is observed for

the ductility. The strain rate varied over four orders of magnitude for these tests.

- The ductility on the structural level, which is represented by flexural tests using thin beams, shows a decrease when the deflection rate is increased. This is in contrast with the results of the tensile rate tests which show no change in ductility with a change in the loading rate. This rate effect is due the rate dependence of the first cracking strength which is shown in Chapter 6 to have a strong effect on the structural ductility.
- On the meso-level, the fibre pull-out resistance shows a strong increase with an increase of the pull-out rate when single fibres are pulled out of the matrix. This increase is believed to be a result of the viscous nature of the matrix which causes an increase of the confining pressure on the fibre during a high pull-out rate thus resulting in a higher frictional shear resistance. This strong increase is however not reflected on the macro-level in tension. The increased pull-out force surpasses the fibre strength at high pull-out rates which cause fibres to rupture and in turn result in a lower than expected ultimate strength on the macro-level.

8.1.2 Experimental creep and shrinkage tests

- The shrinkage behaviour of ECC found is typical of a cement based material. A drying shrinkage value of 0.23 % was found for ECC specimens tested in a controlled environment as described in Chapter 4.
- The mechanisms causing the tensile creep of ECC on the macro-level were identified. They are the matrix creep, the time-dependant crack initiation and the time-dependant pull-out of fibres.
- During the single fibre pull-out creep tests, the embedded fibres tested all crept significantly over time and all the tests resulted in a complete fibre pull-out. The creep rate increased when the fibres were debonded before the onset of the creep load. This shows clearly that fibre pull-out contributes to the tensile creep occurring in a cracked ECC section.
- Uncracked ECC tensile creep tests resulted in a long term creep compliance, C_c, of 0.98 mm/m/MPa at a load of 50 % of the ultimate load.

This value increases to 2.27 mm/m/MPa if the specimen is pre-cracked to 1 % tensile strain. This increase of creep strain is ascribed to the time-dependant pull-out of fibres.

- The tensile creep of ECC shows a substantial increase with regard to the applied stress. At a tensile load of 30 % of the ultimate the creep is 0.49 mm/m/MPa and at a tensile load of 80 % the creep increases to 13.3 mm/m/MPa. This increase is ascribed to the time-dependant fibre pull-out and the time-dependant crack initiation that is believed to occur at high load levels.
- Creep fracture did not occur in direct tension at a load of 80 % of the ultimate static load over a period of 8 months, but the strain did increase from 1.3 % to more than 5 % during this time.

8.1.3 Static modelling of ECC

- The static constitutive model created, which is based on a damage mechanics approach, was implemented with success. Analyses of thin beams tested in flexure were performed and compared to experimental results to verify the model. The model simulates this Mode I dominated failure. The ductility of the response was however under estimated. An analysis of an Iosipescu shear test, which has a dominant Mode II failure mode, underestimated the failure load by 30 %.
- A possible reason for the under prediction of the ductility of the beam in flexure is the orientation of fibres at the edges of the test specimens. The orientation of the fibres on the bottom edge of the beam allows a higher ductility in the area of the highest strain which causes a higher ductility of the experimental test compared to the analysis. This remains to be thoroughly investigated experimentally and numerically.

8.1.4 Time-dependant modelling of ECC

- The static constitutive model was used to simulate the rate-dependent flexural beam tests using the results of the rate-dependant tensile tests as

material model parameters. The analyses simulated the rate-dependant results with reasonable accuracy.

- The creep envelope determined for the flexural tests using the static constitutive model shows that large long term deflection can be expected and that a creep fracture limit may be present assuming there is a creep fracture limit present in tension. The predicted creep fracture limit was however not verified with experimental results as no creep results of beams tested in flexure are available.
- A time-dependant constitutive model was proposed that incorporates the matrix creep as well as the non-linearity associated with creep at high load levels. A preliminary implementation of this model shows that the expected creep behaviour is simulated, but the results could not be verified as no experimental flexural creep results are available.

8.2 Future Work

From the insight gained in this research project, the following are identified as important issues to be investigated further:

- It was shown in Chapter 3 that the interfacial shear resistance is not uniformly distributed along the fibre after full debonding. This is an important issue that requires further investigation as the micro-mechanical models shown in Chapter 2 are all based on the assumption of a uniformly distributed shear resistance along the embedded length of the fibre.
- Creep and creep fracture on a structural level need to be investigated experimentally to validate the creep envelopes found using the constitutive model.
- The effect of the orientation of fibres along the edges of specimens needs to be investigated experimentally and numerically as it has been found to have a significant effect, especially on the ductility of beams tested in flexure.
- The bi-axial behaviour of ECC requires experimental investigation to modify the definition of equivalent strain for the constitutive model to ensure a true numerical response in all stress conditions.

- A mathematical model needs to be formulated that includes the creep caused by time-dependant crack initiation as well as the time-dependant fibre pull-out. The time-dependant constitutive model proposed in Chapter 7 only includes the creep of the matrix.

CHAPTER 9

References

Acker, P., 1993, “Creep tests of concrete: why and how?” Creep and Shrinkage of concrete, Z Bažant and I Carol, RILEM proceedings no 22, E & FN Spoon publishers, London, England. pp 3-14.

Aveston, J., Cooper, G.A., Kelly, A., 1971, “Single and multiple fracture”, Proceedings of the NPL Conference on the Properties of Fiber Composites, National Physical Laboratory, London, England, p.p. 15-26.

Bažant, Z.P., Oh, B.H., 1983, “Crack band theory for fracture of concrete,” Materials and Structures, Vol. 17, No. 93, pp 155-177.

Bažant, Z.P., and Chern, J.C., 1985a, “Concrete creep at variable humidity: Constitutive law and mechanism,” Materials and Structures, Vol. 18 No. 103, pp 1-20.

Bažant, Z.P., Chern, J.C., 1985b, “Strain-softening with creep and exponential algorithm,” Journal of Engineering Mechanics, ASCE, 111(3) pp 391-415.

Bažant, Z.P., 1988, “Mathematical Modelling of Creep and Shrinkage of Concrete, John Wiley and Sons, New York, United States of America.

Bažant, Z.P., Gettu, R., 1989, “Determination of nonlinear fracture characteristic and its time dependency from size effect,” Fracture Mechanics of Concrete and Rock, Recent Developments, Elsevier Science Publishers, London/New York, pp. 549-565.

Bažant, Z.P., Xi, Y. 1994, “Drying creep of concrete: Constitutive model and new experiments separating its mechanisms,” Materials and Structures, Vol 27, pp 3-14.

Boltzmann, Z., 1876, “Zur Theorie er Elastischen Nachwirkung, Sitzber Akad”, Wiss., Wiener Bericht 70, Wiss. Abh., 1, 279-306.

Brühwiler, E., Wittmann, F.H., 1990, “Failure of dam concrete subjected to seismix loading conditions,” Engineering Gracture Mechanics, Vol. 35, pp 565-571.

Cornelissen, H.A.W., Siemes, A.J.M., 1984, “Plain concrete under sustained tensile or tensile and compressive fatigue loadings,” Research on structural concrete 1982-1986, Report 25-87-66 Stevin Laboratory, Delft University of Technology, pp 68-79.

Davids, R.E., Davis, H.E., Brown, E.H., 1937, “Plastic flow and volume changes of concrete,” ASTM Proc. 37, Part 2, pp 317-330.

De Borst, R., 2002, “Fracture in quasi-brittle materials: a review of continuum damage-based approaches,” Engineering Fracture Mechanics, Vol. 69, pp 95-112.

Douglas, K.S., Billington, S.L., 2005, “Rate dependencies in high-performance fibre-reinforced cement-based composites for seismic application,” Proceedings of HPFRCC Conference, Hawaii.

Feenstra, P.H., 1993, “Computational aspects of biaxial stress in plain and reinforced concrete,” Dissertation, Delft University of Technology, Delft, The Netherlands.

Freyssinet, E., 1951, ”Deformation of Concrete,” Magazine of Concrete Research, Vol. 3, No. 8. pp 49-56.

Fu, H.C., Erki, M.A., Seckin, M., 1991, “Review of Effects of Loading Rate on Reinforced Concrete,” Journal of Structural Engineering, Vol. 177, No. 12, pp 3660-3679.

Glucklich, J. 1968, “The effect of micro-cracking on the time-dependant deformations and the long-term strength of concrete,” Proceedings of the International Conference on the Structure of Concrete. Cement and Concrete Association, London, England, pp 176-189.

Han, T.-S., Feenstra, P.H., Billington, S.L., 2003, “Simulation of Highly Ductile Fiber-Reinforced Cement-based Composite Components Under Cyclic Loading,” ACI Structural Journal, November-December 2003, pp. 749-757.

Hannant, D.J., 1978, “Fibre Cements and Fibre Concretes,” John Wiley & Sons, Ltd., New York, United States of America.

Hillerborg, A., Modeer, M., Petersson, P., 1976, “Analyses of crack formation and crack growth in concrete by means of fracture mechanics and finite elements,” Cement and Concrete Research, Vol. 9, Issue 1, pp 147-150.

Illston, J.M., 1965a, “Components of strain in concrete under sustained compressive stress,” Magazine of Concrete Research, Vol. 17, No. 50, pp 21-28.

Illston, J.M., 1965b, “The creep of concrete under uniaxial tension,” Magazine of Concrete Research, Vol. 17, No. 51, pp 77-84.

Iosipescu, N., 1967, “New accurate method for single shear testing of metals,” Journal of Materials, No. 3, pp 537.

Kabele, P., 2000, “Assessment of Structural Performance of Engineered Cemetitious Composites by Computer Simulation,” A habilitation thesis, Czech Technical University, Prague.

Kabele, P., 2003, “Linking scales in modelling of fracture in high performance fiber reinforced cemetitious composites,” Fracture Mechanics of Concrete Structures, Li et al, Proceedings for Ia-FraMCoS 2004, Vail, Colorado, USA.

Kanda, T., and V.C. Li, 1998, “Interface Property and Apparent Strength of a High Strength Hydrophilic Fiber in Cement Matrix,” ASCE J. Materials in Civil Engineering, Vol. 10, No. 1, pp 5-13.

Kesner, K.E., Billington, S.L., Douglas, K.S., 2003, “Cyclic response of highly ductile fibre-reinforced cement-based composites,” ACI Materials Journal, Vol. 100 No. 5, pp 381-390.

Kong, F.K., Evans, R.H., 1987, “Reinforced and Prestressed Concrete,” Spon Press, London, Great Brittain.

Katz, A., and Li, V.C., 1996, “A Special Technique for Determining the Bond Strength of Carbon Fibers in Cement Matrix by Pullout Test,” in J. Materials Science Letters, Vol. 15, pp 1821-1823.

Körmeling, H.A., 1986, “Strain rate and temperature behaviour of steel fibre in concrete in tension,” Dissertation, Delft University of Technology, Delft, The Netherlands.

Kovler, K., 1995, “Interdependence of Creep and Shrinkage for Concrete under Tension,” Journal of Materials in Civil Engineering, May 1995, pp 96–101.

Kovler, K., 1996, “Why Sealed Concrete Swells,” ACI Materials Journal, July-August 1996, pp 334-340.

Leung, C.K.Y., Li, V.C., 1991, “A new strength-based model for the debonding of discontinuous fibres in an elastic matrix,” Journal of Materials Science, Vol 26, No. 11, pp 5996-6010.

Li, V.C., and Wang, Y., and Backer, S., 1990, “Effect of Inclining Angle, Bundling, and Surface Treatment on Synthetic Fiber Pull-Out from a Cement Matrix,” J. Composites, Vol. 21, No. 2, pp 132-140.

Li, V.C., 1992, “Post-Crack Scaling Relations for Fiber-Reinforced Cementitious Composties,” ASCE J. of Materials in Civil Engineering, Vol. 4, No. 1, pp 41-57.

Li, V. C., 1993, “From Micromechanics to Structural Engineering: The Design of Cementitious Composites for Civil Engineering Applications,” J. Struct. Mech. Earthquake Eng., JSCE, Vol. 10, No. 2, 37-48.

Li, V.C., Wu, H.C., and Chan, Y.W., 1995, “Interface Property Tailoring for Pseudo Strain-hardening Cementitious Composites,” in Advanced Technology on Design and Fabrication of Composite Materials and Structures, Ed. Carpinteri and Sih, Kluwer Acad. Publ., Netherlands, pp. 261-268.

Li, V.C., Wu, H.C., and Chan, Y.W., 1996, “Effect of Plasma Treatment of Polyethylene Fibers on Interface and Cementitious Composite Properties,” J. of American Ceramics Society, Vol. 79, No. 3, pp 700-704.

Li, V.C., 1998, “Engineered Cementitious Composites - Tailored Composites Through Micromechanical Modeling,” in Fiber Reinforced Concrete: Present and the Future edited by N. Banthia, A. Bentur, A. and A. Mufti, Canadian Society for Civil Engineering, Montreal, pp. 64-97.

Li, V. C., Wang, S., Wu, C., 2001, “Tensile Strain-hardening Behavior of PVA-ECC,” ACI Materials Journal, Vol. 98, No. 6, pp 483-492.

Li, V. C., Wu, C., Wang, S., Ogawa,. A., Saito, T., 2002, “Interface Tailoring for Strain-hardening PVA-ECC,” ACI Materials Journal, Vol. 99, No. 5, pp 463-472.

Lin, Z., Li, V.C., 1997, “Crack bridging in fiber reinforced cementitious composites with slip-hardening interfaces,” J. Mech. Phys. Solids, Vol. 45, No. 5, pp 763-787.

Lin, Z., Kanda, T., Li, V.C., 1999, “On Interface Property Characterization and Performance of Fiber Reinforced Cementitious Composites,” J. Concrete Science and Engineering, RILEM, Vol. 1, pp. 173-184.

Maalej, M., Quek, S.T., Zhang, J., 2005, “Behaviour of Hybrid-Fibre Engineered Cemetitious Composites Subjected to Dynamic Tensile Loading a Projectile Impact,” Journal of Materials in Civil Engineering, ASCE, pp 143-152.

Mechtcherine, V., Schulze, J., 2005, “Testing the behaviour of strain hardeing cementitious composites in tension,” Proceedings of HPFRCC Conference, Hawaii 2005.

Neville, A.M, 1970, “Creep of Concrete: Plain, reinforced and prestressed,” North Holland publishing company, Amsterdam.

Ngo, D., Scordelis, A.C., 1967, “Finite element analysis of reinforced concrete beams,” Journal of the American Concrete Institute, Vol. 64, pp 152-163.

Østergaard, L., Walter, R., Oleson, J.F., 2005, “Method for determination of tensile properties of ECC II: Inverse analysis and experimental results,” Proceedings of HPFRCC Conference, Hawaii 2005.

Pickett, G., 1942, “The effect of change in moisture content on the creep of concrete under a sustained load,” Journal of the ACI, Vol. 38, pp 333-355.

Rashid., Y.R., 1968, “Analysis of prestressed concrete pressure vessels,” Nuclear Engineering, Vol. 7, pp. 334-344.

Redon, C., Li, V.C., Wu, C., Hoshiro, H., Saito, T., Ogawa, A., 2001, “Measuring and Modifying Interface Properties of PVA Fibers in ECC Matrix,” ASCE J. Materials in Civil Engineering, Vol. 13, No. 6, pp 399-406.

Rots, J.G., 1998, “Computational modelling of concrete fracture,” Dissertation, Delft University of Technology, Delft, The Netherlands.

Shang, Q., 2006, “Shear behaviour of Engineered Cement-based Composites,” M.Sc. Thesis, University of Stellenbosch, South Africa.

Simone, A., Sluys, L.J., Kabele, P., 2003, “Combined continuous/discontinuous failure of cementitious composites,” Computational Modelling of

Concrete Structures, Bicanic et al (editors), Proceedings for EURO-C 2003, pp 133-137.

Tazawa, E., Miyazawa, S., Kasai, T., 1995a, "Chemical shrinkage and autogenous shrinkage of hydrating cement paste," Cement and Concrete Research, Vol. 25, No. 2, pp 288-292.

Tazawa, E. and Miyazawa, S, 1995b., "Experimental study on mechanism of autogenious shrinkage of concrete," Cement and Concrete Research, Vol 25, No. 8. pp 1633-1638.

Thomas, F.G., 1937, "Creep of concrete under load," International Association of Testing Materials, London Congress, pp. 292-294.

Van Zijl, G.P.A.G., 2000, "Computational modelling of masonry creep and shrinkage," Dissertation, Delft University of Technology, Delft, The Netherlands.

Van Zijl, G.P.A.G., De Borst, R., Rots, J.G., 2001, "The role of crack rate dependence in the long-term behaviour of cemetitious materials," International Journal of Solids and Structures, Vol. 38, pp 5063-5079.

Wang, Y., Backer, S., and Li, V.C., 1988, "A Special Technique for Determination of the Critical Length of Fiber Pull-Out from a Cement Matrix," J. Materials Science Letters, Vol. 7, pp 842-849.

Wittmann, F.G. and Roelfstra, P.E., 1980, "Total deformation of loaded drying concrete," Cement and Concrete Research, Vol. 10, pp 601-610.

Wittmann, F.H., Roelfstra, P.E., Mihasi, H., Yiun-yuang Huang, Xinhua Zhang, Nomura, N., 1987, "Influence of age of loading, water-cement ratio and rate of loading on fracture energy of concrete," RILEM, Materials and Structures, 1987, Vol. 20, pp 103-110.

Wittmann, F.H., 1993, "On the influence of stress on shrinkage of concrete," Creep & Shrinkage of concrete, E & FN Spoon Publ., London, England, pp 151-157.

Yang, E., Li, V.C., "Rate dependence in Engineered Cementitious Composites," Proceedings of HPFRCC Conference, Hawaii 2005.

Zhou, F.P., 1992, "Time-dependent Crack Growth and Fracture in Concrete," PhD thesis, University of Lund, Sweden.